Tailored four-wave-mixing processes for optical quantum information science

Christensen, Jesper Bjerge

Publication date:
2018

Document Version
Publisher's PDF, also known as Version of record

DTU Fotonik
Department of Photonics Engineering

Technical University of Denmark

PhD Thesis

Tailored four-wave-mixing processes for optical quantum information science

Author:
Jesper Bjerge Christensen

Supervisors:
Karsten Rottwitt
Leif Katsuo Oxenløwe

Abstract

This thesis deals with applications of nonlinear four-wave mixing in the context of optical quantum information science. By enabling diverse functionalities such as single-photon generation, temporal shaping, and frequency conversion, four-wave mixing is a highly versatile tool for processing optical quantum information.

The first part addresses the use of spontaneous four-wave mixing for generating entangled photon pairs with the particular property that the photons are uncorrelated in time and frequency. Two schemes are proposed to achieve this. The first proposal relies on a gradually varying interaction between two orthogonally polarized pump pulses in a birefringent waveguide. It is shown that, if the two pump pulses undergo a complete walk-through, the two generated photons emerge in orthogonal polarizations with uncorrelated- and tailorable time-frequency distributions. The second proposal deals with photon-pair generation in a microring resonator. In this setting, it is shown that a dual-pulse configuration can be used to excite- and subsequently de-excite the resonator on a sub-lifetime timescale. This turns out to strongly diminish time-frequency correlations.

The second part considers the four-wave-mixing process Bragg scattering, which is known to enable noise-free frequency conversion. The Bragg-scattering process treated here, which occurs in a birefringent waveguide, is shown to allow for shape-preserving and strongly uni-directional conversion with a large acceptance bandwidth.

Resumé

Denne PhD-afhandling omhandler brugen af ikke-lineær firebølgeblanding i relation til optisk kvanteinformationsvidenskab. Ved at muliggøre forskellige funktionaliteter såsom enkeltfotongenerering, tidslig formning og frekvenskonvertering, udgør firebølgeblanding et alsidigt værktøj til processering af optisk kvanteinformation.

Første del adresserer brugen af spontan firebølgeblanding til generationen af sammenfiltrede fotonpar med den særlige egenskab, at de to fotoner er ukorrelerede i tid og frekvens. To fremgangsmetoder foreslås for at opnå dette. Det første forslag bygger på en gradvist varierende interaktion mellem to ortogonalt polariserede pulser i en dobbeltbrydende bølgeleder. Det vises at, såfremt de to pulser undergår en komplet kollision, dannes de to fotoner i ortogonale polarizationer med ukorrelerede- og kontrolerbare fordelinger i tid og frekvens. Forslag nummer to omhandler dannelsen af fotonpar i en mikroringresonator. I dette scenarie vises der, at en konfiguration bestående af en dobbeltpuls kan bruges til at excitere og dernæst af-excitere resonatoren på en tidsskala der er kortere en resonatorens naturlige levetid.

I anden del betragtes processen Bragg spredning, som muliggør støjfri optisk frekvenskonvertering. For Bragg spredning i en dobbeltbrydende bølgeleder vises det, at processen tillader både en stærkt ensrettet- og tidsbevarende konvertering for en stor signal båndbredde.

Preface

This thesis is written in partial fulfilment of the requirements for the PhD degree from the Technical University of Denmark. The thesis is based on work performed at the department DTU Fotonik in the Fiber Optics, Devices & Nonlinear Effects Group, from October 2015 through October 2018, under supervision of Prof. Karsten Rottwitt and Prof. Leif Katsuo Oxenløve. Part of the work included in this thesis was carried out at University of Bristol, United Kingdom, in the group of Prof. Mark Thompson, which I was fortunate enough to visit in the period from March 2017 through June 2017.

At the University of Bristol I would especially like to thank Gary Sinclair, Sebastian Knauer, and Will McCutcheon for the many discussions and the fun we had.

A special thanks goes to Prof. Colin McKinstrie with whom I have enjoyed a very productive collaboration. Especially during the first year of my PhD, Prof. Colin McKinstrie played an important role and helped me accelerate my studies through his always detailed feedback and many ideas. I would also like to send thoughts of appreciation overseas to Prof. Michael Raymer who I visited prior to my PhD studies and continued collaboration with afterwards. Further, I thank Kai Guo, who was a visiting PhD student in our group for two years, for his always energetic behavior and remarkable work spirit.

At the Technical University of Denmark there are many co-workers and friends who I have enjoyed collaborating with and who deserve mentioning. Among them are Mario A. U. Castaneda, Davide Bacco, Søren M. M. Friis, Mikkel Heuck, Yunhong Ding, and Prof. Søren Forchhammer. I would especially like to thank Lars H. Frandsen for discussions on and fabrication of our waveguide samples, Peter D. Girouard for his lead and our collaboration on the dispersion-measurement setup, and Michael Galili and Prof. Leif. K. Oxenløwe for the synergy and interaction made possible through the 'SPOC' Center of Excellence. Further, I am very grateful to my fellow PhD students Erik N. Christensen and Jacob G. Koefoed for the close collaboration and the many discussions we have had throughout the years.

Moreover, I greatly acknowledge the funding organizations: Otto Mønsted Fond, Oticon Fonden, P. A. Fiskers Fond, and Haynmans Fond, who aided my project financially and thereby enabled me to attend conferences all over the world and to pursue my research abroad.

Lastly, a final thanks goes to my main supervisor Prof. Karsten Rottwitt, who I have worked with for more than three years. I have truly enjoyed the work environment in his group, our supervisor meetings, and his unheard-of terrible jokes. Thank you for having provided me with this opportunity!

Jesper Bjerge Christensen

Department of Photonics Engineering
Technical University of Denmark
2800 Kgs. Lyngby, October 2018

List of Publications

The following list contains the publications resulting from the 3-year PhD project.

Scientific journal articles

1. **Jesper B. Christensen**, Jacob G. Koefoed, Bryn A. Bell, Colin J. McKinstrie, and Karsten Rottwitt, *Shape-preserving and unidirectional frequency conversion by four-wave mixing*, Optics Express **26**, 17145 (2018).

2. **Jesper B. Christensen**, Jacob G. Koefoed, Karsten Rottwitt, and Colin J. McKinstrie, *Engineering spectrally unentangled photon pairs from nonlinear microring resonators by pump manipulation*, Optics Letters **43**, 859 (2018).

3. Kai Guo, **Jesper B. Christensen**, Xiaodong Shi, Erik N. Christensen, Li Lin, Yunhong Ding, Haiyan Ou, Karsten Rottwitt, *Experimentally validated dispersion tailoring in a silicon strip waveguide with alumina thin-film coating*, IEEE Photonics Journal **10**, 6600508 (2018).

4. Jacob G. Koefoed, **Jesper B. Christensen**, Colin J. McKinstrie, and Karsten Rottwitt, *Effects of dispersion on spontaneous four-wave mixing in quantum applications*, submitted (2018).

5. Jacob G. Koefoed, **Jesper B. Christensen**, and Karsten Rottwitt, *Effects of noninstantaneous nonlinear processes on photon-pair generation by spontaneous four-wave mixing*, Physical Review A **95**, 043842 (2017).

6. Kai Guo, Søren M. M. Friis, **Jesper B. Christensen**, Erik N. Christensen, Xiaodong Shi, Yunhong Ding, Haiyan Ou, and Karsten Rottwitt, *Full-vectorial propagation model and modified effective mode area of four-wave mixing in straight waveguides*, Optics Letters **42**, 3670 (2017).

7. Colin J. McKinstrie, **Jesper B. Christensen**, Karsten Rottwitt, and Michael G. Raymer, *Generation of two-temporal-mode photon states by vector four-wave mixing*, Optics Express **25**, 20877 (2017).

8. Jacob G. Koefoed, Søren M. M. Friis, **Jesper B. Christensen**, and Karsten Rottwitt, *Spectrally pure heralded single photons by spontaneous four-wave mixing in a fiber: reducing impact of dispersion fluctuations*, Optics Express **25**, 20835 (2017).

9. Kai Guo, Li Lin, **Jesper B. Christensen**, Erik N. Christensen, Xiaodong Shi, Yunhong Ding, Karsten Rottwit, and Haiyan Ou, *Broadband wavelength conversion in a silicon vertical-dual-slot waveguide*, Optics Express **25**, 32964 (2017).

10. Kai Guo, Erik N. Christensen, **Jesper B. Christensen**, Jacob G. Koefoed, Davide Bacco, Yunhong Ding, Haiyan Ou, and Karsten Rottwitt, *High coincidence-to-accidental ratio continuous-wave photon-pair generation in a grating-coupled silicon strip waveguide*, Applied Physics Express **10**, 062801 (2017).

11. Davide Bacco, **Jesper B. Christensen**, Mario A. U. Castaneda, Yunhong Ding, Søren Forchhammer, Karsten Rottwitt, and Leif K. Oxenløwe, *Two-dimensional distributed-phase-reference protocol for quantum key distribution*, Scientific Reports **6**, 36756 (2016).

12. **Jesper B. Christensen**, Colin J. McKinstrie, and Karsten Rottwitt, *Temporally uncorrelated photon-pair generation by dual-pump four-wave mixing*, Physical Review A **94**, 013819 (2016).

Conference proceedings

1. Mikkel Heuck, Yunhong Ding, Lars H. Frandsen, Jacob G. Koefoed, **Jesper B. Christensen**, and Karsten Rottwitt, *Unidirectional Frequency Conversion in Silicon-based Double-Ring Microresonator*, Proceedings of 2018 Conference on Lasers and Electro-Optics, JTh4C.4 (2018).

2. **Jesper B. Christensen**, Jacob G. Koefoed, Colin J. McKinstrie, and Karsten Rottwittm *Spectrally unentangled photon pairs from microring resonators using pump-pulse tailoring*, Proceedings of 2018 Conference on Lasers and Electro-Optics, FTh1G.1 (2018).

3. Erik N. Christensen, **Jesper B. Christensen**, Søren M. M. Friis, Jacob G. Koefoed, Mario A. U. Castenada, and Karsten Rottwitt, *Heralded single-photon source based on intermodal four-wave mixing in a few-mode fiber*, Proceedings of 2018 Conference on Lasers and Electro-Optics, FM3G.3 (2018).

4. **Jesper B. Christensen**, Jacob G. Koefoed, Erik N. Christensen, Søren M. M. Friis, Colin J. McKinstrie, and Karsten Rottwitt, *Four-wave mixing in quantum information science*, Quantum Nonlinear Optics Conference 2018, SuA4.3 (2018).

5. **Jesper B. Christensen**, Jacob G. Koefoed, Colin J. McKinstrie, and Karsten Rottwitt, *Breaking the microring photon-purity limit*, Quantum Nonlinear Optics Conference 2018, SaPS.12 (2018).

6. Jacob G. Koefoed, **Jesper B. Christensen**, and Karsten Rottwitt, *Split-step scheme for photon-pair generation through spontaneous four-wave mixing*, 2017 Conference on Lasers and Electro-Optics Europe & European Quantum Electronics Conference, 8087370 (2017).

7. Søren M. M. Friis, **Jesper B. Christensen**, Jacob G. Koefoed, and Karsten Rottwitt, *Study of Raman-free photon pair generation using inter-modal four-wave mixing in a few-mode silica fiber*, 2017 Conference on Lasers and Electro-Optics Europe & European Quantum Electronics Conference, 8086542 (2017).

8. Colin J. McKinstrie, **Jesper B. Christensen**, Karsten Rottwitt, and Michael G. Raymer, *Single-temporal-mode photon generation beyond the low-power regime*, Proceedings of Quantum Information and Measurement (QIM), 2017, QW3C.6 (2017).

9. Mario A. U. Castaneda, Davide Bacco, **Jesper B. Christensen**, Yunhong Ding, Karsten Rottwit, Leif K. Oxenløwe, *Differential phase-time shifting protocol for QKD (DPTS)*, Proceedings of QCMC 2016, 2354981414 (2016).

10. **Jesper B. Christensen**, Colin J. McKinstrie, and Karsten Rottwitt, *Generation of pure heralded single-photon states by cross-polarized spontaneous four-wave mixing*, Proceedings of CLEO: QELS_Fundamental Science 2016, FTu4C.8 (2016).

Contents

List of Figures

Abbreviations

BS	**B**ragg **s**cattering
CE	**C**onversion **e**fficiency
CME	**C**oupled-**m**ode **e**quation
CW	**C**ontinuous **w**ave
EDFA	**Er**bium-**d**oped **f**iber **a**mplifier
FCA	**F**ree-**c**arrier **absorption**
FSR	**F**ree **s**pectral **r**ange
FWM	**F**our-**w**ave **m**ixing
GVD	**G**roup **v**elocity **d**ispersion
JSA	**J**oint **s**pectral **a**mplitude
JSI	**J**oint **s**pectral **i**ntensity
JTA	**J**oint **t**emporal **a**mplitude
HG	**H**ermite-**G**aussian
HNLF	**H**ighly **n**on**l**inear **f**iber
MRR	**M**icro**r**ing **r**esonator
MZM	**M**ach-**Z**ehnder **m**odulator
NPM	**N**onlinear **p**hase **m**odulation
OSA	**O**ptical **s**pectrum **a**nalyser
PM	**P**olarization **m**aintaining
PECVD	**P**lasma-**e**nhanced **c**hemical-**v**apor **d**eposition
RF	**R**adio **f**requency
SFWM	**S**pontaneous **f**our-**w**ave **m**ixing

SPM	**S**elf-**p**hase **m**odulation
TE	**T**ransverse **e**lectric
TM	**T**ransverse **m**agnetic
TPA	**T**wo-**p**hoton **a**bsorption
XPM	**C**ross-**p**hase **m**odulation
ZDF	**Z**ero-**d**ispersion **f**requency

Nomenclature

Symbol	Unit	Description
A_i	$\mathrm{W}^{1/2}$	Field envelope amplitude of mode i
A_{eff}	m^2	Effective mode area
$\mathcal{A}$		Joint amplitude of the two-photon state
D	$\mathrm{ps\ km^{-1}\ nm^{-1}}$	Dispersion parameter
$\mathbf{E}$	$\mathrm{V\ m^{-1}}$	Electric field
$\bar{E}_j$	J	Energy of pulsed pump j
f_j	m^{-1}	Transverse distribution of mode j
G_{jk}	s^{-1}	Green transfer function
H_{jk}	s^{-1}	Reverse Green transfer function
H		Heaviside step function
l	m	Waveguide length
n		Linear refractive index
n_2	$\mathrm{m^2\ W^{-1}}$	Intensity dependent refractive index
n_{eff}		Effective refractive index
n_{g}		Group refractive index
$\bar{n}$		Mean photon number
$\mathbf{P}$	$\mathrm{C\ m^{-2}}$	Induced polarization density
P_j	W	Power of pump j
$\mathcal{P}$		Single-photon purity
Q		Resonator quality factor
$\mathbf{r}$	m	Position vector
R		Generation rate/probability
V		Interference visibility
t	s	Time variable
t_c	s	Temporal collision coordinate

Continued...

Symbol	Unit	Description
x	m	Transverse coordinate
y	m	Transverse coordinate
z	m	Longitudinal position coordinate
z_c	m	Positional collision coordinate
α		Spectral pulse envelope
β	m^{-1}	Propagation constant
$\beta^{(1)}$	$\mathrm{s\ m}^{-1}$	Inverse group velocity
$\beta^{(1)}$	$\mathrm{s}^2\ \mathrm{m}^{-1}$	Group-velocity-dispersion parameter
β_{jk}	$\mathrm{s\ m}^{-1}$	Inverse group-velocity difference
$\Delta\beta$	m^{-1}	Wavenumber mismatch
$\Delta\beta_1$	$\mathrm{s\ m}^{-1}$	Relative inverse group velocity
$\Delta\tau$	s	Temporal delay between pulses
$\Delta\Phi$		Differential phase between tones
λ	m	Wavelength
λ_k		Schmidt coefficient of order k
ν	s^{-1}	Frequency
ω	$\mathrm{rad\ s}^{-1}$	Angular frequency
$\chi^{(1)}$		Linear susceptibility
$\chi^{(2)}$	$\mathrm{m\ V}^{-1}$	Second-order nonlinear susceptibility
$\chi^{(3)}$	$\mathrm{m}^2\ \mathrm{V}^{-2}$	Third-order nonlinear susceptibility
ε		Relative permittivity
ϵ		Polarization-dependent coupling coefficient
τ_j	s	Width of the pulsed pump j
$\psi_{\mathrm{i},n}$		The nth idler Schmidt mode
$\psi_{\mathrm{s},n}$		The nth signal Schmidt mode
Ψ		General quantum state
Ψ_{II}		Biphoton quantum state
η		Splitting ratio
ζ		Normalized pulse walk-off
γ	$\mathrm{W}^{-1}\ \mathrm{m}^{-1}$	Nonlinear coefficient
γ'		Normalized interaction strength
$\hat{a}_j$		Photon annihilation operator for mode j

Continued...

Symbol	Unit	Description
$\hat{A}_j$		Broadband annihilation operator of mode j
$\hat{H}$	J	Hamiltonian operator
$\hat{n}_j$		Photon number operator, mode j
$\hat{\rho}$		Density operator
$\hat{U}$		Unitary operator

Part I

Introduction

CHAPTER 1

Introduction

1.1 Perspective

One of the most significant and far-reaching discoveries within optics and photonics is that of the laser by Maiman in 1960 [1]. The laser has since then continued to find uses in vastly different scenarios, ranging from optical-fiber communication and interferometry to microscopy and surgery. The high field strengths and long coherence lengths provided by lasers also allowed entrance into the realm of *nonlinear optics* where the electric field itself alters the optical properties of a material [2, 3, 4]. Nonlinear optics, which forms the backbone of most of the work performed in relation to this thesis, has since the first demonstration of coherent wave mixing [5], been a subject of much scientific and industrial interest. A first example of this is that of second-harmonic generation in a second-order nonlinear crystal, which is used in green lasers to frequency double light from 1064 nm to 532 nm. Another promising application of nonlinear optics is in the form of amplifiers for optical communications systems. This can be achieved through either broadband stimulated Raman scattering [6] or third-order nonlinear parametric interaction [7]. Third-order nonlinearities, in for example silica glass, can also be used for supercontinuum generation [8].

The development of nonlinear optics has provided a convenient platform for fundamental tests of quantum mechanics and quantum entanglement. Parametric down conversion in second-order nonlinear crystals, in which a pump photon elastically scatters into two daughter photons of lower frequencies, early on provided an accessible way of generating entangled beams of light. So-called squeezed light plays an important role in *quantum optics* [9], and is key to quantum protocols for quantum cryptography [10], quantum imaging [11], and quantum-enhanced metrology [12]. For low squeezing strengths, i.e. a moderately low pump power

or a short nonlinear medium, the correlated beams of light each only probabilistically contain a single photon. Through this process, it is therefore possible to spontaneously produce pairs of photons with a perfectly correlated number statistics. Such photon pairs have been used to break Bell's inequality [13, 14] and, moreover, form a popular framework for quantum key distribution [15, 16]. Alternatively, by using one of the created photons as a trigger, the photon-pair source is re-build into a source of heralded single photons. In the subset of quantum optics where information is encoded onto single-photon qubits such sources form an instrumental building block towards quantum supremacy[1] with e.g. non-universal Boson Sampling [17, 18], and ultimately the realization of universal optical quantum computing [19, 20, 21]. For this reason, much effort has been devoted to designing and building efficient sources of single photons [22].

In the past decade there has been a tendency of moving from bulky platforms onto photonic chips and integrated photonic circuits. Realization of the lab-on-a-chip idea to replace non-commercializable setups on optical tables is slowly becoming reality, and by now the integration of hundreds or thousands of optical components can be realized on a single photonic chip [23, 24]. This is also the case in the framework of nonlinear quantum optics, wherein recent experiments demonstrating 8- and 10-photon entanglement have approached the limit of scalability for bulk optics [25, 26]. Thus, it is natural to combine quantum optics and integrated optics, as has been done by multiple research groups world wide. The development and success of integrated photonics is largely made possible by the high refractive index of materials such as silicon, which allow ultra tight field confinement in waveguides of sub-square-micron cross-sections. The strong confinement allows waveguide bend-radii of less than 10 μm leading to a high density of components, and it also reinforces nonlinear interactions, which scales inversely with the effective waveguide mode area. However, the materials typically used for photonic integration have a centrosymmetric microscopic structure, and thereby exhibit a vanishing second-order nonlinear response. Resultingly, for these materials nonlinear functionalities must be realized through the weaker third-order nonlinear (Kerr) response, and the effect called four-wave mixing, which is a main focus of this thesis.

1.2 Motivation

In this thesis, we aim to design and engineer third-order nonlinear processes that are useful for quantum information processing and have implementations in integrated settings. The focus of the thesis therefore lies in the intersection of the three fields; nonlinear optics, quantum optics, and integrated optics.

[1] The notion of achieving a quantum speed-up relative to the fastest possible computation performed classically.

1.3 Outline of thesis

Chapter 2: Contains basic theory on the quantum-interference effect and photon-pair generation using spontaneous four-wave mixing, to be used in later chapters.

Chapter 3: We analyse a method for generating spectrally uncorrelated photon pairs based on cross-polarized spontaneous four-wave mixing in a birefringent waveguide.

Chapter 4: We propose and study a novel method for generating spectrally uncorrelated photon pairs from integrated resonator structures, which is based on pump-pulse tailoring.

Chapter 5: We study the properties of optical frequency conversion enabled by four-wave mixing Bragg scattering based on cross-polarized pump fields in a birefringent waveguide.

Chapter 6: We simulate, design, and characterize the properties of in-house fabricated hydrogenated amorphous silicon birefringent waveguides.

Chapter 7: The thesis is concluded by summarizing the most important results and findings, and by providing an outlook for future work.

CHAPTER 2

Theoretical foundations and background

While it is not the purpose here to give a comprehensive overview of the rich field of nonlinear optics, significant understanding can be gained by use of intuitive physical arguments. This approach is taken in Sec. 2.1 where we introduce both the Kerr effect and different flavors of the process called four-wave mixing. This is, in Sec. 2.2, followed by an introduction to two-mode squeezing and the related process spontaneous four-wave mixing, which, in the low-squeezing regime can be used for photon-pair generation. In Sec. 2.3, we study the properties of the biphoton quantum state, and introduce the important quantity known as the joint spectral amplitude. We then, in Sec. 2.4, discuss the phenomena of photon-photon quantum interference, before we revisit, with newly gained insight, the joint spectral amplitude again in Sec. 2.5.

2.1 Nonlinear optics – a crash course

A key capability in both linear and nonlinear optics is that of being able to describe what happens as an electromagnetic wave propagates through an optical medium. In general, this problem involves solving the four Maxwell equations [27], but for our purpose it suffices to consider the derived nonlinear wave equation. The wave equation describes the relationship between an electric field, $\mathbf{E}(\mathbf{r},t)$, characterized by properties of polarization, transverse profile, phase, and frequency, and the induced polarization of the optical material, $\mathbf{P}(\mathbf{r},t)$:

$$\nabla^2\mathbf{E} - \frac{1}{c^2}\partial_t^2\mathbf{E} = \mu_0\partial_t^2\mathbf{P}, \tag{2.1}$$

where $\partial_t = \partial/\partial t$, and ∇ is the nabla-operator $\nabla^2 = \partial_x^2 + \partial_y^2 + \partial_z^2$, c is the speed of light in vacuum, and μ_0 is the vacuum permeability. Physically, the

polarization $\mathbf{P}$ originates from atomic dipoles that align, and oscillate, due to the electric field. Hence, $\mathbf{P}$ describes a materials response to an applied electric field, but through Eq. (2.1) it also causes a back action on the electric field, as we shall see shortly. The nature of the optical response may vary greatly depending on the exact material, and may be either slow (vibronic or rotational atomic motions), or extremely fast (electronic motions). Considering, for simplicity, a medium response that is purely due to the electronic contributions, the optical response may be assumed both local and instantaneous, and the relation $\mathbf{P}(\mathbf{E})$ takes the form of a power series (here truncated to third order):

$$P_i(\mathbf{r},t) = \varepsilon_0 \left[\chi^{(1)}_{ij} E_j(\mathbf{r},t) + \chi^{(2)}_{ijk} E_j(\mathbf{r},t) E_k(\mathbf{r},t) + \chi^{(3)}_{ijkl} E_j(\mathbf{r},t) E_k(\mathbf{r},t) E_l(\mathbf{r},t) \right], \tag{2.2}$$

where ε_0 is the vacuum permittivity, $i,j,k,l \in \{x,y,z\}$ represent polarization direction, and sums are implied over the indices of the electric fields. The optical response of the medium is contained in the susceptibility tensors $\chi^{(m)}$, of rank $m+1$, of which $\chi^{(1)}$ describes the linear optical response and $\chi^{(m\geq 2)}$ account for the mth order nonlinear responses. Equation (2.2) expresses the very basis of nonlinear optics: to exit the linear regime and make the nonlinear optical responses relevant, a certain field strength is required. Moreover, Eq. (2.2) also illustrates the fact that non-diagonal elements of the susceptibility tensors allow an electric field that is, say, x-polarized to induce a polarization that is oriented in the y-direction. This ability is going to play a key role in Chapters 3 and 5.

Now, to begin demystifying Eq. (2.1) we first consider the effect of the linear optical response in Eq. (2.2). For simplicity, we consider an isotropic material, i.e. one for which the optical properties are independent of direction, which means that $\chi^{(1)}_{ij} = \delta_{ij}\chi^{(1)}$, where δ_{ij} is the Kroenecker delta function. Using the relations $c^2 = (\varepsilon_0\mu_0)^{-1}$ and $n^2 = 1 + \chi^{(1)}$, with n being the material refractive index, the wave equation in Eq. (2.1) reduces to the homogeneous form

$$\nabla^2\mathbf{E} - \frac{n^2}{c^2}\partial_t^2\mathbf{E} = 0. \tag{2.3}$$

Thus, as compared to propagation in vacuum, the linear response of the optical material acts to slow down the electromagnetic field by a factor of n. Physically, this delay is caused by electric-field induced oscillating microscopic dipoles. An oscillating (accelerating) dipole itself sets up an electric field, which is, in general, not in phase with the exerted electric field, and therefore acts to slow it down.

The quadratic second-order term in Eq. (2.2) accounts for second-order nonlinear effects such as the electro-optic effect and second-harmonic generation. However, the materials dealt with in this work exhibit a vanishing second-order susceptibility, making the third-order induced polarization the dominant nonlinear perturbation to the linear polarization.

2.1.1 Intensity-dependent refractive index

We now examine the effect of the third-order nonlinear polarization, which is cubed in the electric field, and is known as the Kerr effect [4]. We start by assuming an electric field consisting of a monochromatic wave of angular frequency, ω_0, polarized along a principal axis, here the x-axis, of the optical medium:

$$E_x(\mathbf{r},t) = \frac{1}{2}\left[E_{\omega_0}(\mathbf{r})\mathrm{e}^{-i\omega_0 t} + \text{c.c.}\right], \tag{2.4}$$

Writing, likewise, for the third-order induced polarization

$$P_x^{(3)}(\mathbf{r},t) = \frac{1}{2}\sum_{\omega_\sigma>0}\left[P_{\omega_\sigma}^{(3)}(\mathbf{r})\mathrm{e}^{-i\omega_\sigma t} + \text{c.c.}\right], \tag{2.5}$$

where the sum over ω_σ runs over all positive discrete frequencies induced by the electric field. Now, to find the third-order induced polarization at a specific frequency, one inserts Eqs. (2.4) and (2.5) into Eq. (2.2), and combine terms oscillating at the same frequency. For example, for the original frequency of the monochromatic field, one finds

$$P_{\omega_0}^{(3)}(\mathbf{r}) = \frac{3\varepsilon_0}{4}\chi_{xxxx}^{(3)}|E_{\omega_0}(\mathbf{r})|^2 E_{\omega_0}(\mathbf{r}), \tag{2.6}$$

where the pre-factor of $3/4$ stems from the different permutations of $(\omega_0, -\omega_0, \omega_0)$, and the factors of $1/2$ in Eqs. (2.4) and (2.5). Adding this finding to Eq. (2.3), the wave equation instead reads

$$\nabla^2\mathbf{E} - \frac{\varepsilon_\mathrm{L}+\varepsilon_\mathrm{NL}}{c^2}\partial_t^2\mathbf{E} = 0, \tag{2.7}$$

where we have defined the linear permittivity $\varepsilon_\mathrm{L} = 1 + \chi_{xx}^{(1)}$ and the nonlinear permittivity $\varepsilon_\mathrm{NL} = 3\chi_{xxxx}^{(3)}|\tilde{E}_{\omega_0}|^2/4$. On this form, it is clear that the refractive index experienced by the field at frequency ω_0 has a contribution that scales with the intensity of the light field itself. Indeed, if we treat the nonlinear permittivity as a small perturbation, Taylor-expanding $n = (\varepsilon_\mathrm{L}+\varepsilon_\mathrm{NL})^{1/2}$ results in [28]

$$n \approx n_0 + \frac{3\chi_{xxxx}^{(3)}}{8n_0}|E_{\omega_0}|^2, \tag{2.8}$$

where $n_0 = \varepsilon_\mathrm{L}^{1/2}$. From this it is seen that the field alters its own propagation, a nonlinear phenomena known as the intensity-dependent refractive index, and in the considered example results in an effect, which for obvious reasons is called self-phase modulation (SPM). In an analogous way, one optical field can impart a nonlinear phase shift on another optical field. This process is referred to as cross-phase modulation (XPM).

It is at this point noted that the preceding section omits both linear and nonlinear losses, which, however, may be introduced by including imaginary parts of

the linear and nonlinear susceptibility tensors, respectively.

2.1.2 Categorizing four-wave mixing

In addition to SPM and XPM, the Kerr effect also enables transfer of energy between fields of different frequencies through the effect known as four-wave mixing (FWM) [2]. To demonstrate this, assume now that the electric field initially consists of two monochromatic waves of dissimilar frequencies ω_1 and ω_2:

$$E_x(\mathbf{r},t) = \frac{1}{2}\left[E_{\omega_1}(\mathbf{r})\mathrm{e}^{-i\omega_1 t} + E_{\omega_2}(\mathbf{r})\mathrm{e}^{-i\omega_2 t} + \text{c.c.}\right]. \tag{2.9}$$

This electric field, like before, sets up an induced polarization at angular frequencies ω_1 and ω_2, resulting in a perturbation of the refractive indices at these frequencies. However, it also induces a polarization at various beating frequencies between the two fields, such as $\omega_3 = 2\omega_1 - \omega_2$, $\omega_4 = 2\omega_2 - \omega_1$, or at the third-harmonics $\omega_5 = 3\omega_1$ and $\omega_6 = 3\omega_2$. Considering the induced polarization at ω_3, we find

$$P^{(3)}_{\omega_3}(\mathbf{r}) = \frac{3\varepsilon_0}{4}\chi^{(3)}_{xxxx}(E_{\omega_1}(\mathbf{r}))^2 E^*_{\omega_2}(\mathbf{r}), \tag{2.10}$$

which indicates that the beating between fields at ω_1 and ω_2 sets up an induced polarization at frequency ω_3. As explained earlier, this induced-polarization component stems from microscopic oscillating dipoles, which as a back-action radiates an electromagnetic field of frequency ω_3. However, for a field at this particular frequency to grow up, the frequency-component at ω_3 of these many dipoles must have a very particular phase relation, so that the light radiated from them interfere constructively. This is expressed by the so-called *phase-matching* criterion, which can be established by considering the spatial evolution of the fields. Assuming propagation along the z-axis in an optical waveguide, the electric field at a given frequency component may be written as $E_{\omega_j}(\mathbf{r}) = \tilde{E}_{\omega_j}(\mathbf{r}_\perp, z)\mathrm{e}^{i\beta(\omega_j)z}$, where the wavenumber $\beta(\omega_j)$ is determined from the waveguide structure and its refractive index profile. Inserting this expression of the electric-field component into Eq. (2.10) along with the corresponding expansion $P^{(3)}_{\omega_j}(\mathbf{r}) = \tilde{P}^{(3)}_{\omega_j}(\mathbf{r}_\perp, z)\mathrm{e}^{i\beta(\omega_j)z}$, one finds

$$\tilde{P}^{(3)}_{\omega_j}(\mathbf{r}_\perp, z) = \frac{3}{4}\varepsilon_0\chi^{(3)}_{xxxx}(\tilde{E}_{\omega_1}(\mathbf{r}_\perp, z))^2\tilde{E}^*_{\omega_2}(\mathbf{r}_\perp, z)\mathrm{e}^{i\theta z}, \tag{2.11}$$

where $\theta = 2\beta(\omega_1) - \beta(\omega_2) - \beta(\omega_3)$, is the wavenumber-matching term that must vanish to achieve efficient coherent energy conversion through FWM. Quantum-mechanically, what happens in this process, is that two photons of energy $\hbar\omega_1$ are annihilated, and, simultaneously, a photon of energy $\hbar\omega_2$ and a photon of energy $\hbar\omega_3$ are created. This process can for example be used to amplify weak signals in a communication system by propagating them inside a nonlinear medium alongside a strong coherent pump beam — such a device is known as an optical parametric amplifier [29].

Typically, the nonlinear polarization necessary to observe FWM is induced by one or two strong coherent beams called the pumps. The pumps are used to

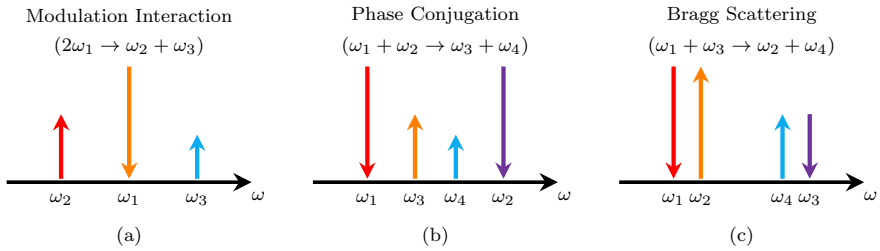

Figure 2.1: Different types of FWM-processes; (a) modulation interaction, (b) phase conjugation, and (c) Bragg scattering. The arrows indicate direction of energy flow (which may be reversed).

control the energy flow into (or out of) one or multiple signal fields. Figure 2.1 illustrates three different flavors of FWM including in Fig. 2.1(a) the degenerate FWM process, here referred to as modulation interaction, which was used in the example above. As the name suggests, FWM also exists in versions involving four fields (non-degenerate), as demonstrated in Figs. 2.1(b) and (c). Figure 2.1(b) illustrates the process often referred to as phase conjugation [30], which, like modulation interaction, is an amplification process of the input. The input field is called the *signal* field while the biproduct of the process is the *idler* field. In another form, known as FWM Bragg scattering [31], shown in Fig. 2.1(c), the signal is not amplified, but instead gradually converted to another frequency while at the same time energy flows from one pump to the other[1]. We here, and in the next two chapters, focus on the amplification processes, but return to a study of FWM Bragg scattering in Chapter 5.

2.2 Two-mode squeezing by four-wave mixing

In the previous section, we saw how the FWM-process exchanges energy between various frequencies, and in particular, how the process, in a classical picture, is stimulated by the presence of multiple distinct frequencies in the optical field. However, the FWM-process can also occur *spontaneously* being stimulated by vacuum fluctuations at the signal- and idler frequencies. To describe this effect one must resort to a quantum-mechanical description of the underlying Hamiltonian.

[1]We note that there is only a subtle difference between phase conjugation and FWM Bragg scattering in the designation of pumps and signals. This is, however, an important one from an application point-of-view!

2.2.1 Simplistic treatment

We start by considering a simplistic description, in which the Hamiltonian describing the interaction depicted in Fig. (2.1)(a) or (b) takes the form

$$\hat{H}_{\mathrm{TMSq}} = -i\hbar\Gamma\hat{a}_{\mathrm{i}}^{\dagger}\hat{a}_{\mathrm{s}}^{\dagger} + \mathrm{h.c.}. \tag{2.12}$$

Here, h.c. stands for Hermitian conjugate, $\hbar$ is the reduced Planck constant, and $\Gamma = \xi \mathrm{e}^{i\theta}$ where ξ (θ) is the squeezing strength (angle) related to the pump power(s) and the medium nonlinearity. Finally, $\hat{a}_{\mathrm{i,s}}^{\dagger}$ are quantum-mechanical photon creation operators of the signal (s) and idler (i) modes that obey the Bosonic commutator relations:

$$[\hat{a}_j, \hat{a}_k] = 0, \qquad \left[\hat{a}_j, \hat{a}_k^{\dagger}\right] = \delta_{jk}, \qquad j,k \in \{\mathrm{i},\mathrm{s}\}. \tag{2.13}$$

The Hamiltonian in Eq. (2.12) is bilinear in the signal- and idler mode operators $\hat{a}_{\mathrm{s}}$ and $\hat{a}_{\mathrm{i}}$, indicating that signal- and idler photons are generated and annihilated in pairs. This becomes even more evident if we consider the operation of the corresponding unitary operator $\hat{U} = \mathrm{e}^{-i\hat{H}_{\mathrm{TMSq}}t/\hbar}$ on the signal-idler vacuum state $|0,0\rangle_{\mathrm{i,s}}$. Doing so generates a so-called two-mode squeezed vacuum state[2], which, in the photon-number basis, has the following solution [9]:

$$\begin{aligned} |\Psi_{\mathrm{TMSV}}\rangle &= \mathrm{e}^{-\Gamma t\hat{a}_{\mathrm{i}}^{\dagger}\hat{a}_{\mathrm{s}}^{\dagger} + \mathrm{h.c.}}\,|0,0\rangle_{\mathrm{i,s}} \\ &= \frac{1}{\cosh(\xi t)}\sum_{n=0}^{\infty}(-1)^n \mathrm{e}^{in\theta}\tanh^n(\xi t)\,|n,n\rangle_{\mathrm{i,s}}\,. \end{aligned} \tag{2.14}$$

The two-mode squeezed vacuum state in Eq. (2.14) is a coherent superposition of terms containing an equal number of signal- and idler photons, and hence exhibits perfect photon-number correlations. Such entangled beams of light are often referred to as "twin beams", and can be generated using both second- and third-order nonlinearities [32, 33]. If generated using the third-order nonlinearity, then the process is often referred to as spontaneous four-wave mixing (SFWM).

In terms of the probability distribution of having exactly N signal photons and N idler photons, one finds [9]

$$P_{N,N} = \langle N,N|\Psi_{\mathrm{TMSV}}\rangle\,\langle\Psi_{\mathrm{TMSV}}|N,N\rangle = \frac{\sinh^{2N}(\xi t)}{\left[1+\sinh^2(\xi t)\right]^{N+1}}. \tag{2.15}$$

Due to the perfect photon-number correlation, each of the signal- and idler subsystems has the exact same photon-number probability distribution, so that $P_N^{(\mathrm{i})} = P_N^{(\mathrm{s})} = P_{N,N}$, which can moreover be shown to be a thermal distribution of mean value $\bar{n} = \langle\hat{n}_{\mathrm{i}}\rangle = \langle\hat{n}_{\mathrm{s}}\rangle = \sinh^2(\xi t)$. This entails that, while there exists strong

[2]The origin of this name comes from the continuous-variable framework: The superposition quadratures of the two modes can be squeezed below the usual quantum-noise limit.

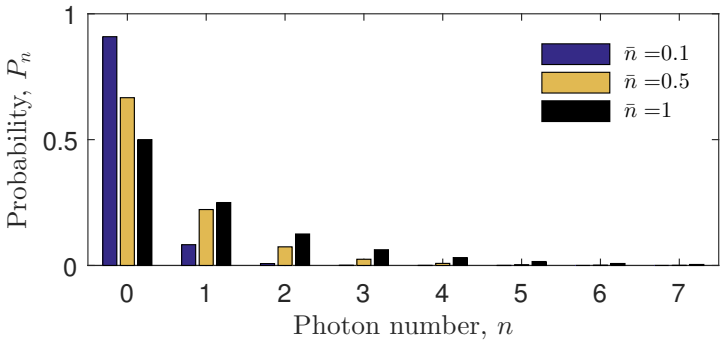

Figure 2.2: Thermal probability distribution of P_n versus photon number n.

inter-mode entanglement between the signal- and idler modes, each mode by itself "just" behaves like thermal light.

Figure 2.2 illustrates the thermal probability distribution for three distinct mean values, $\bar{n}$. For large $\bar{n}$ there is a significant probability of having more than a single photon in the field, whereas for small $\bar{n}$ (< 0.1), this probability quickly dies out ($P_{n\geq 2} \propto \bar{n}^2$). This realization enables the construction of probabilistic sources of single pairs of signal and idler photons. Moreover, by utilizing the degree-of-freedom which distinguishes the signal- and idler photons (be it frequency, space, or polarization), it is possible to use one of the photons, say the idler, to trigger the presence of the signal photon. Such a source of quasi single-photon states is referred to as a *heralded* single-photon source.

2.2.2 Detailed treatment

In practice, two-mode squeezing is experimentally accomplished by pumping a nonlinear material with laser light. However, the generated squeezed field(s) are most often not single-mode in the sense that they occupy a span of wavevectors (in a 3D scenario) or frequencies (in a 1D waveguide scenario). Typically, the laser used is pulsed, and is thus characterized by a broad bandwidth participating in the nonlinear interaction. In this case, the notion used in Eqs. (2.12) is no longer adequate. In the following, we give a detailed theoretical description of pulsed two-mode squeezing attained by exploiting the third-order optical Kerr nonlinearity in for example optical fibers or integrated waveguides.

Hamiltonian and quantization

The third-order nonlinear interaction energy is contained in the, now time-dependent, interaction Hamiltonian [34]

$$\hat{H}_{\mathrm{Int}}(t) = -\frac{\epsilon_0}{4}\int \mathrm{d}\mathbf{r}\ \chi^{(3)}_{jklm}(\mathbf{r})\hat{E}_j(\mathbf{r},t)\hat{E}_k(\mathbf{r},t)\hat{E}_l(\mathbf{r},t)\hat{E}_m(\mathbf{r},t), \tag{2.16}$$

where summation over all four indices, which represent polarization, is implied, and we have assumed a non-dispersive (no time dependence) third-order susceptibility tensor. We take the electric field to be composed of three distinct components denoted p (pump), i (idler), and s (signal), allowing us to write

$$\hat{\mathbf{E}}(\mathbf{r},t) = \hat{\mathbf{E}}_{\mathrm{p}}(\mathbf{r},t) + \hat{\mathbf{E}}_{\mathrm{i}}(\mathbf{r},t) + \hat{\mathbf{E}}_{\mathrm{s}}(\mathbf{r},t) \tag{2.17}$$

The combined electric field is confined to a waveguide geometry in the (x, y)-plane and propagate in the z direction from the input $z = 0$ to the output $z = l$. Moreover, for simplicity, we consider the situation where the three field components are co-polarized along the x-axis, so that from this point onwards subindices to an electric field refer to the three different frequency bands denoted p, i, and s.

The electric fields in Eqs. (2.16) and (2.17) are now operators, as opposed to the classical treatment in Sec. 2.1. Writing $\hat{E}_j(\mathbf{r},t) = \hat{E}^{(+)}_j(\mathbf{r},t) + \hat{E}^{(-)}_j(\mathbf{r},t)$, where $\hat{E}^{(-)}_j(\mathbf{r},t) = [\hat{E}^{(+)}_j(\mathbf{r},t)]^\dagger$, for $j \in \{\mathrm{p},\mathrm{i},\mathrm{s}\}$, we quantize them according to [35, 36]

$$\hat{E}^{(+)}_j(\mathbf{r},t) = i f_j(x,y)\int \mathrm{d}\omega\ \mathcal{B}(\omega)\hat{a}_j(\omega)\mathrm{e}^{i[\beta_j(\omega)z-\omega t]}, \tag{2.18}$$

where $f_j(x,y)$ is the x-polarized transversal mode distribution of the waveguided geometry normalized such that $\iint \mathrm{d}x\mathrm{d}y|f(x,y)|^2 = 1$, β_j is the wavenumber, and

$$\mathcal{B}(\omega) = \left[\frac{\hbar\omega}{4\pi\varepsilon_0 n(\omega)c}\right]^{1/2}, \tag{2.19}$$

is a slowly varying constant that is typically dragged outside the integral. Doing so is justified by the fact that each field is relatively narrowband such that $\Delta\omega_j \ll \omega_{j_0}$, where ω_{j_0} is a center frequency. In contrary to the earlier approach where we were dealing with discrete mode operators, our quantized electric field is now composed of a continuum of mode operators $\hat{a}_j(\omega)$, which obey the commutation relations

$$[\hat{a}_j(\omega), \hat{a}_k(\omega')] = 0, \qquad \left[\hat{a}_j(\omega), \hat{a}^\dagger_k(\omega')\right] = \delta_{jk}\delta(\omega-\omega'), \tag{2.20}$$

where $\delta(\omega-\omega')$ is the Dirac δ-function. The treatment so far deals with a quantum-mechanical pump field. However, the pump field is typically a strong coherent beam, and we may therefore neglect its quantum fluctuations and replace $\hat{E}^{(+)}_{\mathrm{p}}$

with

$$E_{\mathrm{p}}(\mathbf{r},t) = if_{\mathrm{p}}(x,y)\left[4\pi\varepsilon_0 n(\omega_{\mathrm{p}_0})c\right]^{-1/2}\int \mathrm{d}\omega_{\mathrm{p}}\ \alpha_{\mathrm{p}}(\omega_{\mathrm{p}})\mathrm{e}^{i[\beta_{\mathrm{p}}(\omega_{\mathrm{p}})z-\omega_{\mathrm{p}}t]}, \tag{2.21}$$

where α_{p} is spectral envelope of the pump.

The interaction Hamiltonian in Eq. (2.16) contains all the possible third-order nonlinear processes that involve the three fields. However, we here limit our attention to the process that is responsible for photon-par generation, described by the effective Hamiltonian

$$\hat{H}_{\mathrm{eff}}(t) = -\frac{12\varepsilon_0}{4}\chi^{(3)}_{\mathrm{eff}}\int \mathrm{d}\mathbf{r}\ E^{(+)}_{\mathrm{p}}(\mathbf{r},t)E^{(+)}_{\mathrm{p}}(\mathbf{r},t)\hat{E}^{(-)}_{\mathrm{i}}(\mathbf{r},t)\hat{E}^{(-)}_{\mathrm{s}}(\mathbf{r},t) + \mathrm{h.c.}, \tag{2.22}$$

where the factor of 12 stems from the possible permutations of $(E^{(+)}_{\mathrm{p}}, E^{(+)}_{\mathrm{p}}, \hat{E}^{(-)}_{\mathrm{i}}, \hat{E}^{(-)}_{\mathrm{s}})$, and we have assumed a longitudinal invariant effective third-order susceptibility $\chi^{(3)}_{\mathrm{eff}}$, which is averaged over the mode cross-section. Insertion of the electric fields from Eq. (2.17) and Eq. (2.21), yields the effective Hamiltonian

$$\begin{aligned}\hat{H}_{\mathrm{eff}}(t) = -\frac{3\hbar\left(\omega_{\mathrm{i}}\omega_{\mathrm{s}}\right)^{1/2}\chi^{(3)}_{\mathrm{eff}}}{16\varepsilon_0 c^2 A_{\mathrm{eff}} n(\omega_{\mathrm{p}_0})\left[n(\omega_{\mathrm{i}_0})n(\omega_{\mathrm{s}_0})\right]^{1/2}}\int_0^l \mathrm{d}z \iiiint \mathrm{d}\omega_{\mathrm{p}_1}\mathrm{d}\omega_{\mathrm{p}_2}\mathrm{d}\omega_{\mathrm{i}}\mathrm{d}\omega_{\mathrm{s}}\\ \times\alpha_{\mathrm{p}}(\omega_{\mathrm{p}_1})\alpha_{\mathrm{p}}(\omega_{\mathrm{p}_2})\hat{a}^{\dagger}_{\mathrm{i}}(\omega_{\mathrm{i}})\hat{a}^{\dagger}_{\mathrm{s}}(\omega_{\mathrm{s}})\mathrm{e}^{i\Theta} + \mathrm{h.c.},\end{aligned} \tag{2.23}$$

where the effective nonlinear mode-area overlap

$$A^{-1}_{\mathrm{eff}} = \iint \mathrm{d}x\mathrm{d}y\ f_{\mathrm{p}}(x,y)f_{\mathrm{p}}(x,y)f^{*}_{\mathrm{i}}(x,y)f^{*}_{\mathrm{s}}(x,y) \tag{2.24}$$

and the phase

$$\begin{aligned}\Theta &= \Delta\beta z - \Delta\omega t\\ &= [\beta_{\mathrm{p}}(\omega_{\mathrm{p}_1}) + \beta_{\mathrm{p}}(\omega_{\mathrm{p}_2}) - \beta_{\mathrm{i}}(\omega_{\mathrm{i}}) - \beta_{\mathrm{s}}(\omega_{\mathrm{s}})]z - (\omega_{\mathrm{p}_1} + \omega_{\mathrm{p}_2} - \omega_{\mathrm{i}} - \omega_{\mathrm{s}})t.\end{aligned} \tag{2.25}$$

From Eq. (2.23), we see that the nonlinearity scales proportionally to $\chi^{(3)}_{\mathrm{eff}}/A_{\mathrm{eff}}$, and by defining the nonlinear parameter [2, 37]:

$$\gamma_e = \frac{3\left(\omega_{\mathrm{i}}\omega_{\mathrm{s}}\right)^{1/2}\chi^{(3)}_{\mathrm{eff}}}{4\varepsilon_0 c^2 A_{\mathrm{eff}} n(\omega_{\mathrm{p}_0})\left[n(\omega_{\mathrm{i}_0})n(\omega_{\mathrm{s}_0})\right]^{1/2}}, \tag{2.26}$$

the effective Hamiltonian takes on the shorter form

$$\hat{H}_{\mathrm{eff}}(t) = -\frac{\hbar\gamma_e}{4\pi^2}\int_0^l \mathrm{d}z \iiiint \mathrm{d}\omega_{\mathrm{p}_1}\mathrm{d}\omega_{\mathrm{p}_2}\mathrm{d}\omega_{\mathrm{i}}\mathrm{d}\omega_{\mathrm{s}}\alpha_{\mathrm{p}}(\omega_{\mathrm{p}_1})\alpha_{\mathrm{p}}(\omega_{\mathrm{p}_2})\hat{a}^{\dagger}_{\mathrm{i}}(\omega_{\mathrm{i}})\hat{a}^{\dagger}_{\mathrm{s}}(\omega_{\mathrm{s}})\mathrm{e}^{i\theta} + \mathrm{h.c.}. \tag{2.27}$$

State evolution — a perturbative approach

We are now ready to consider how a quantum state evolves due to the effect of the above effective Hamiltonian. Considering an initial state being in the vacuum state, the state evolution is given by[3]

$$|\Psi\rangle = \hat{U}\,|0,0\rangle_{\mathrm{i,s}} = \exp\left[-\frac{i}{\hbar}\int_{t_1}^{t_2}\mathrm{d}t\;\hat{H}_{\mathrm{eff}}(t)\right]|0,0\rangle_{\mathrm{i,s}}\,, \tag{2.28}$$

where the time integral extends from a time before the pump pulse enters the nonlinear waveguide, t_1 to a time after it has exited the nonlinear waveguide t_2. As there is no nonlinear interaction outside this interval, we may extend the limits of integration from $-\infty$ to $+\infty$. Performing the time integral yields a Dirac delta function through the relation $2\pi\delta(\omega-\omega') = \int_{-\infty}^{\infty}\mathrm{d}t\;\mathrm{e}^{i(\omega-\omega')t}$. Thus, using Eq. (2.25), we find

$$-\frac{i}{\hbar}\int_{-\infty}^{\infty}\mathrm{d}t\hat{H}_{\mathrm{eff}}(t) = \frac{i\gamma_e}{2\pi}\int_0^l\mathrm{d}z\iiiint\mathrm{d}\omega_{\mathrm{p}_1}\mathrm{d}\omega_{\mathrm{p}_2}\mathrm{d}\omega_{\mathrm{i}}\mathrm{d}\omega_{\mathrm{s}}\;\alpha_{\mathrm{p}}(\omega_{\mathrm{p}_1})\alpha_{\mathrm{p}}(\omega_{\mathrm{p}_2}) \times\hat{a}_{\mathrm{i}}^{\dagger}(\omega_{\mathrm{i}})\hat{a}_{\mathrm{s}}^{\dagger}(\omega_{\mathrm{s}})\mathrm{e}^{i\Delta\beta z}\delta(\omega_{\mathrm{p}_1}+\omega_{\mathrm{p}_2}-\omega_{\mathrm{i}}-\omega_{\mathrm{s}})+\mathrm{h.c.}, \tag{2.29}$$

which enables elimination of the integral over ω_{p_2}. Finally, we may carry out the z-integral, and find

$$-\frac{i}{\hbar}\int_{-\infty}^{\infty}\mathrm{d}t\hat{H}_{\mathrm{eff}}(t) = \frac{i\gamma_e l}{2\pi}\iiint\mathrm{d}\omega_{\mathrm{p}_1}\mathrm{d}\omega_{\mathrm{i}}\mathrm{d}\omega_{\mathrm{s}}\;\alpha_{\mathrm{p}}(\omega_{\mathrm{p}_1})\alpha_{\mathrm{p}}(\omega_{\mathrm{i}}+\omega_{\mathrm{s}}-\omega_{\mathrm{p}_1}) \times\Phi(\omega_{\mathrm{p}_1},\omega_{\mathrm{i}},\omega_{\mathrm{s}})\hat{a}_{\mathrm{i}}^{\dagger}(\omega_{\mathrm{i}})\hat{a}_{\mathrm{s}}^{\dagger}(\omega_{\mathrm{s}})+\mathrm{h.c.}, \tag{2.30}$$

which includes the so-called phase-matching function:

$$\Phi(\omega_{\mathrm{p}_1},\omega_{\mathrm{i}},\omega_{\mathrm{s}}) = \mathrm{sinc}\left(\frac{\Delta\beta l}{2}\right)\mathrm{e}^{i\Delta\beta l/2}. \tag{2.31}$$

As we are mainly interested in the regime of a weak interaction, we may now expand the unitary evolution operator from Eq. (2.28) in a first-order Taylor series, yielding

$$\hat{U}\approx\hat{\mathcal{I}}+\frac{i\gamma_e l}{2\pi}\iiint\mathrm{d}\omega_{\mathrm{p}_1}\mathrm{d}\omega_{\mathrm{i}}\mathrm{d}\omega_{\mathrm{s}}\;\alpha_{\mathrm{p}}(\omega_{\mathrm{p}_1})\alpha_{\mathrm{p}}(\omega_{\mathrm{i}}+\omega_{\mathrm{s}}-\omega_{\mathrm{p}_1})\Phi(\omega_{\mathrm{p}_1},\omega_{\mathrm{i}},\omega_{\mathrm{s}})\hat{a}_{\mathrm{i}}^{\dagger}(\omega_{\mathrm{i}})\hat{a}_{\mathrm{s}}^{\dagger}(\omega_{\mathrm{s}})+\mathrm{h.c.}. \tag{2.32}$$

While the first term in this expansion, the identity operator, leaves the vacuum unchanged, the second term presents paired generation of a signal- and an idler photon. Equation (2.28) may now be expressed as $|\Psi\rangle = |0,0\rangle_{\mathrm{i,s}} + |\Psi_{\mathrm{II}}\rangle$, where

[3] We have here neglected a time-ordering operator that takes into account the fact that the Hamiltonian does not in general commute with itself at different points in time. This approximation has been shown valid in the low-generation regime considered here. For more information, refer e.g. [38, 39, 40].

the perturbative term is the biphoton (photon-pair) quantum state considered in the following section.

2.3 Biphoton quantum state

The biphoton wavefunction $|\Psi_{\mathrm{II}}\rangle$ may generally be formulated in terms of a two-dimensional complex function, $\mathcal{A}(\omega_i, \omega_s)$, called the joint spectral amplitude (JSA) [41]:

$$|\Psi_{\mathrm{II}}\rangle = \iint \mathrm{d}\omega_{\mathrm{i}}\mathrm{d}\omega_s \mathcal{A}(\omega_{\mathrm{i}}, \omega_{\mathrm{s}})\hat{a}_{\mathrm{i}}^{\dagger}(\omega_{\mathrm{i}})\hat{a}_{\mathrm{s}}^{\dagger}(\omega_{\mathrm{s}})\,|0,0\rangle_{\mathrm{i,s}}\,. \tag{2.33}$$

The JSA fully characterizes the joint spectrum of a photon pair, encompassing both possible spectral correlation between the signal- and idler photons as well as the two-photon spectral probability density through its square modulus; the joint spectral intensity (JSI). Moreover, the JSA is connected to the corresponding joint temporal amplitude (JTA) through a 2-dimensional Fourier-transform relation (see App. A), offering an alternative, yet equivalent, description of the biphoton state vector [42]:

$$|\Psi_{\mathrm{II}}\rangle = \iint \mathrm{d}t_{\mathrm{i}}\mathrm{d}t_s \mathcal{A}(t_{\mathrm{i}}, t_{\mathrm{s}})\hat{a}_{\mathrm{i}}^{\dagger}(t_{\mathrm{i}})\hat{a}_{\mathrm{s}}^{\dagger}(t_{\mathrm{s}})\,|0,0\rangle_{\mathrm{i,s}}\,, \tag{2.34}$$

where $\hat{a}_j^{\dagger}(t_j) = (2\pi)^{-1/2}\int \mathrm{d}\omega_j \hat{a}_j^{\dagger}(\omega_j)\mathrm{e}^{-i\omega_j t_j}$ is an operator that generates a photon in mode j at time t_j. It is important to note that the times t_{i} and t_{s} do not represent times of creation (in which case the JTA would always be δ-correlated in its two variables), but rather represent the times where the photons exit the nonlinear waveguide.

The joint amplitudes are two-dimensional complex functions, which entails that they have a Schmidt decomposition [43]. In the case of the JSA, this reads

$$\mathcal{A}(\omega_{\mathrm{i}}, \omega_{\mathrm{s}}) = \sum_{k=1}^{\infty} \lambda_k \psi_{\mathrm{i},k}(\omega_{\mathrm{i}})\psi_{\mathrm{s},k}(\omega_{\mathrm{s}}), \tag{2.35}$$

where λ_k are descendingly ordered real-valued Schmidt coefficients and $\psi_{\mathrm{i},k}$, $\psi_{\mathrm{s},k}$, are kth order idler- and signal Schmidt functions, respectively. The Schmidt functions form two orthonormal sets such that the inner products

$$\int \mathrm{d}\omega\ \psi_{\mathrm{i},j}(\omega)\psi_{\mathrm{i},k}^{*}(\omega) = \int \mathrm{d}\omega\ \psi_{\mathrm{s},j}(\omega)\psi_{\mathrm{s},k}^{*}(\omega) = \delta_{jk}. \tag{2.36}$$

The formulation of the JSA in terms of its Schmidt decomposition furthermore invites the definition of broadband mode operators: [44]

$$\hat{A}_{\mathrm{i},k} = \int \mathrm{d}\omega\ \psi_{\mathrm{i},k}^{*}(\omega)\hat{a}_{\mathrm{i}}(\omega), \qquad \hat{A}_{\mathrm{s},k} = \int \mathrm{d}\omega\ \psi_{\mathrm{s},k}^{*}(\omega)\hat{a}_{\mathrm{s}}(\omega), \tag{2.37}$$

which, compared to Eq. (2.13), obey the expanded commutation relations

$$\left[\hat{A}_{j,k}, \hat{A}_{j',k'}\right] = 0, \qquad \left[\hat{A}_{j,k}, \hat{A}^{\dagger}_{j',k'}\right] = \delta_{jj'}\delta_{kk'}, \tag{2.38}$$

where $j, j' \in \{\mathrm{i}, \mathrm{s}\}$ and $k, k' \in \mathbb{N}$. Moreover, in terms of the broadband mode operators defined in Eq. (2.37), the biphoton wavefunction reads simply

$$|\Psi_{\mathrm{II}}\rangle = \sum_{k=1}^{\infty} \lambda_k A^{\dagger}_{\mathrm{i},k} A^{\dagger}_{\mathrm{s},k} |0,0\rangle_{\mathrm{i,s}} . \tag{2.39}$$

As earlier mentioned, a source of spontaneously generated pairs of photons can be converted into a heralded single-photon source. Assuming that we are using the idler as the trigger photon, then upon a triggering event, the signal photon is described by the reduced density operator (assuming a normalized biphoton wavefunction)

$$\begin{aligned}\hat{\rho}_{\mathrm{s}} = \mathrm{Tr}_{\mathrm{i}}\left\{|\Psi_{\mathrm{II}}\rangle\langle\Psi_{\mathrm{II}}|\right\} &= \iiint \mathrm{d}\omega_{\mathrm{s}}\mathrm{d}\omega'_{\mathrm{s}}\mathrm{d}\omega_{\mathrm{i}} \mathcal{A}(\omega_{\mathrm{i}}, \omega_{\mathrm{s}})\mathcal{A}^*(\omega_{\mathrm{i}}, \omega'_{\mathrm{s}}) \hat{a}^{\dagger}_{\mathrm{s}}(\omega_{\mathrm{s}}) |0\rangle\langle 0| \hat{a}_{\mathrm{s}}(\omega'_{\mathrm{s}}) \\ &= \sum_{k=1}^{\infty} \lambda_k^2 \hat{A}^{\dagger}_{s,k} |0\rangle\langle 0| \hat{A}_{\mathrm{s},k}. \end{aligned} \tag{2.40}$$

From the reduced density operator, we may furthermore calculate the quantum-mechanical spectral-temporal purity of the signal photon according to

$$\begin{aligned}\mathcal{P}_{\mathrm{s}} = \mathrm{Tr}_{\mathrm{s}}\left\{\hat{\rho}_{\mathrm{s}}{}^2\right\} &= \iiiint \mathrm{d}\omega_{\mathrm{i}}\mathrm{d}\omega'_{\mathrm{i}}\mathrm{d}\omega_{\mathrm{s}}\mathrm{d}\omega'_{\mathrm{s}} \mathcal{A}(\omega_{\mathrm{i}}, \omega_{\mathrm{s}})\mathcal{A}^*(\omega_{\mathrm{i}}, \omega'_{\mathrm{s}})\mathcal{A}^*(\omega'_{\mathrm{i}}, \omega_{\mathrm{s}})\mathcal{A}(\omega'_{\mathrm{i}}, \omega'_{\mathrm{s}}) \\ &= \sum_{k=1}^{\infty} \lambda_k^4, \end{aligned} \tag{2.41}$$

which is symmetric in the sense that $\mathcal{P}_{\mathrm{i}} = \mathcal{P}_{\mathrm{s}} = \mathcal{P}$. Equation (2.41) shows that calculating the purity of the heralded photon boils down to performing a Schmidt decomposition of the joint amplitude. A quantum-mechanical pure state, $\mathcal{P} = 1$, is obtained iff $\lambda_1 = 1$ and $\lambda_{k\geq 2} = 0$. This case corresponds to a separable joint amplitude, $\mathcal{A}(\omega_i, \omega_{\mathrm{s}}) = \mathcal{A}_{\mathrm{i}}(\omega_{\mathrm{i}})\mathcal{A}_{\mathrm{s}}(\omega_{\mathrm{s}})$, which is also seen to factor Eq. (2.33). Thus, a pure heralded signal state can only be obtained if there is no spectral (temporal) correlation in the original signal-idler biphoton state. In the following we consider the implications of such correlation in the context of the effect known as quantum interference.

2.4 Quantum interference

Quantum interference, or Hong-Ou-Mandel interference named after its discoverers [45], is arguably one of the most remarkable quantum phenomena. Moreover, quantum interference lies at the heart of many quantum protocols, such as Boson

Sampling [17], or linear optical quantum computing [19, 20], and it has, though only partly for this reason, been a subject of intense study.

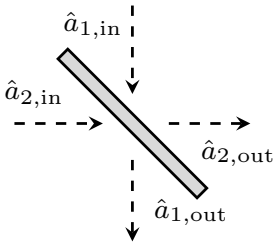

Figure 2.3: Illustration of a beam splitter with quantum-mechanical input- and output operators.

Hong-Ou-Mandel interference occurs at a beam splitter, and we therefore first consider the basic quantum properties of a passive dielectric beam splitter [9]. As sketched in Fig. 2.3, the beam splitter is characterized by having two input ports, with associated photon annihilation operators $\hat{a}_{1,\mathrm{in}}$ and $\hat{a}_{2,\mathrm{in}}$, and two output ports, with associated photon annihilation operators $\hat{a}_{1,\mathrm{out}}$ and $\hat{a}_{2,\mathrm{out}}$. The input and output operators are connected through the transmission and reflection coefficients, and may be formulated on matrix form using the following input-output relation

$$\begin{bmatrix} \hat{a}_{1,\mathrm{out}} \\ \hat{a}_{2,\mathrm{out}} \end{bmatrix} = \begin{bmatrix} \sin(\theta) & i\cos(\theta) \\ i\cos(\theta) & \sin(\theta) \end{bmatrix} \begin{bmatrix} \hat{a}_{1,\mathrm{in}} \\ \hat{a}_{2,\mathrm{in}} \end{bmatrix}, \tag{2.42}$$

such that the splitting parameter θ is related to the transmission and reflection coefficients as $t = \sin(\theta)$, and $r = i\cos(\theta)$. For a balanced 50-50 beam splitter, $\theta = \pi/4$ and $|t|^2 = |r|^2 = 1/2$.

Consider now the particular situation where the two inputs consist of two indistinguishable single photons, i.e. $|\psi_{\mathrm{in}}\rangle = |1\rangle_1 \otimes |1\rangle_2 = \hat{a}^\dagger_{1,\mathrm{in}}\hat{a}^\dagger_{2,\mathrm{in}}\,|0\rangle_1\,|0\rangle_2$. Using the reverse (output-input) relation of Eq. (2.42) with $\theta = \pi/4$, the beam splitter performs the following transformation

$$\begin{aligned} \hat{a}^\dagger_{1,\mathrm{in}}\hat{a}^\dagger_{2,\mathrm{in}}\,|0\rangle_1\,|0\rangle_2 &\to \frac{1}{2}\left(\hat{a}^\dagger_{1,\mathrm{out}} + i\hat{a}^\dagger_{2,\mathrm{out}}\right)\left(\hat{a}^\dagger_{2,\mathrm{out}} + i\hat{a}^\dagger_{1,\mathrm{out}}\right)|0\rangle_1\,|0\rangle_2 \\ &= \frac{1}{2}\Bigg(i(\hat{a}^\dagger_{1,\mathrm{out}})^2 + i(\hat{a}^\dagger_{2,\mathrm{out}})^2 + \underbrace{\hat{a}^\dagger_{1,\mathrm{out}}\hat{a}^\dagger_{2,\mathrm{out}}}_{\text{transmitted}} + \underbrace{i^2\hat{a}^\dagger_{1,\mathrm{out}}\hat{a}^\dagger_{2,\mathrm{out}}}_{\text{reflected}}\Bigg)|0\rangle_1\,|0\rangle_2 \\ &= \frac{i}{\sqrt{2}}\big(\,|2\rangle_1\,|0\rangle_2 + |0\rangle_1\,|2\rangle_2\,\big), \end{aligned} \tag{2.43}$$

where, to obtain the last line, we have used the relation $|n\rangle = (\hat{a}^\dagger)^n/\sqrt{n}\,|0\rangle$. Equation (2.43) exactly encapsulates the effect of quantum interference of *indistinguishable* photons. Notably, the probability amplitudes of both photons being transmitted and that of both photons being reflected appear with opposite signs

and therefore cancel each other. As a result, the output state is an equal superposition of both photons being in output mode 1 and both photons being in output mode 2.

2.4.1 Quantum interference — general case

While the above analysis does well to illustrate the principle of quantum interference, a more general framework is necessary if one wishes to incorporate distinguishability and individual mixedness of the two interfering photons. To do so, consider the more general situation where the two photons in spatial input modes 1 and 2 are instead described by the density operators [see Eq. (2.40)]

$$\hat{\rho}_1 = \sum_{k_1} \lambda_{k_1}^2 \hat{A}_{1,k_1}^\dagger \left|0\right\rangle \left\langle 0\right| \hat{A}_{1,k_1}, \tag{2.44}$$

$$\hat{\rho}_2 = \sum_{k_2} \mu_{k_2}^2 \hat{B}_{2,k_2}^\dagger \left|0\right\rangle \left\langle 0\right| \hat{B}_{2,k_2}, \tag{2.45}$$

where $\hat{A}_{1,k}^\dagger = \int \mathrm{d}\omega\ \psi_{a,k}(\omega)\hat{a}_1^\dagger(\omega)$ and $\hat{B}_{2,k}^\dagger = \int \mathrm{d}\omega\ \psi_{b,k}(\omega)\hat{a}_2^\dagger(\omega)$ are (potentially different) broadband mode operators as defined in Eq. (2.37). Hence, this description, for example, describes the case where the two photons originate from two *different* heralded single-photon sources. In this framework, the probability of receiving a coincidence event, P_{12}, the derivation of which is carried out in Appendix B, is given by [46]

$$P_{12} = \frac{1}{2} - \frac{1}{2} \sum_{k_1,k_2} \lambda_{k_1}^2 \mu_{k_2}^2 \int \mathrm{d}\omega_1 \psi_{a,k_1}^*(\omega_1)\psi_{b,k_2}(\omega_1) \int \mathrm{d}\omega_2 \psi_{b,k_2}^*(\omega_2)\psi_{a,k_1}(\omega_2), \tag{2.46}$$

This expression may further be used analyse what happens as a time delay $\Delta\tau_{12}$ is introduced between the two photons. To implement this, we make the replacement $\psi_{b,k}(\omega) \to \psi_{b,k}(\omega)\mathrm{e}^{i\Delta\tau_{12}\omega}$, which modifies Eq. (2.46) according to

$$P_{12}(\Delta\tau_{12}) = \frac{1}{2} - \frac{1}{2} \sum_{k_1,k_2} \lambda_{k_1}^2 \mu_{k_2}^2 \int \mathrm{d}\omega_1 \psi_{a,k_1}^*(\omega_1)\psi_{b,k_2}(\omega_1) \times \int \mathrm{d}\omega_2 \psi_{b,k_2}^*(\omega_2)\psi_{a,k_1}(\omega_2)\mathrm{e}^{i\Delta\tau_{12}(\omega_1-\omega_2)}. \tag{2.47}$$

From Eq. (2.47) we may calculate the coincidence probability for any two input photons. This is demonstrated in Fig. 2.4, which shows P_{12} versus relative temporal delay for three different cases all obeying $\psi_{a,k} = \psi_{b,k}$, i. e. apart from the adjustable time delay the two input photons are described by the same density operator. The first case (solid blue) illustrates the situation of two Gaussian photon spectra (Hermite-Gaussian of 0th order, HG0), for which we see the usual shape of the so-called Hong-Ou-Mandel dip. Because the photons are spectrally pure and identical, the dip reaches $P_{12} = 0$ at zero delay. The second case (dashed red)

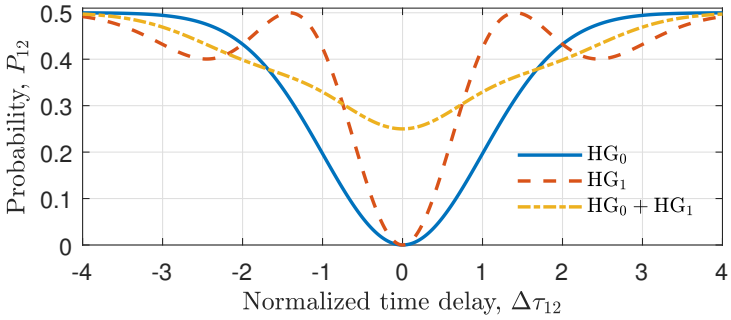

Figure 2.4: Hong-Ou-Mandel interference for three different pairs of identical input photons of varying mixedness and spectral shapes. For details, see text.

shows a modified Hong-Ou-Mandel dip obtained for two photons that are spectrally shaped as Hermite-Gaussians of 1st order (HG1). The final case (dashed-dotted yellow) represents two photons that are each in a spectrally mixed state with equal weights between HG0 and HG1. Here, the coincidence probability only reaches $1/4$ at $\Delta\tau_{12} = 0$ due distinguishability introduced by the mixedness of the input states.

Based on Eq. (2.47) it is common to define a quantum-interference visibility

$$\begin{aligned} V =& \frac{P_{12}(\infty) - P_{12}(0)}{P_{12}(\infty)} \\ =& \sum_{k_1,k_2} \lambda_{k_1}^2 \mu_{k_2}^2 \int \mathrm{d}\omega_1 \psi_{a,k_1}^*(\omega_1)\psi_{b,k_2}(\omega_1) \int \mathrm{d}\omega_2 \psi_{b,k_2}^*(\omega_2)\psi_{a,k_1}(\omega_2), \end{aligned} \tag{2.48}$$

which is a measure of the depth of the Hong-Ou-Mandel dip. This visibility also presents a lower bound on the purity of the individual photons — a bound which is saturated for two photons with identical density operators, $\hat{\rho}_1 = \hat{\rho}_2$, in which case $V = \mathcal{P}_1 = \mathcal{P}_2$. Thus, one way to estimate the quantum purity, is by performing a Hong-Ou-Mandel inteference experiment [32].

2.5 Towards separable biphoton states

We have just seen, in Sec. 2.4, that high-visibility quantum interference between independent single photons requires that the two photons are indistinguishable. The notion of indistinguishability includes that each photon must be in a quantum-mechanical pure state meaning that it is insufficient that the two photons are described by the same mixed state. Furthermore, in Sec. 2.3 we saw that spectral (temporal) correlation in the biphoton state leads to spectral (temporal) mixedness of a single photon heralded from the pair. For exactly this reason, it is important

to be able to design photon-pair sources that exhibit the least possible degree of correlation.

2.5.1 Joint spectral amplitude — degenerate SFWM

By combining Eqs. (2.32) and (2.33), we find that the JSA describing photon pairs generated through degenerate (single-pump) SFWM can be formulated as (neglecting the pre-factor which is irrelevant for now)

$$\mathcal{A}(\omega_\mathrm{i}, \omega_\mathrm{s}) = \int \mathrm{d}\omega \; \alpha_\mathrm{p}(\omega)\alpha_\mathrm{p}(\omega_\mathrm{i} + \omega_\mathrm{s} - \omega)\Phi(\omega, \omega_\mathrm{i}, \omega_\mathrm{s}). \tag{2.49}$$

The JSA constitutes a convolution-like integral that expresses the following: for each set of signal- and idler frequencies, a continuum of paired pump frequencies contribute with a weight determined by both the pump spectrum and the phase-matching function.

To proceed from Eq. (2.49), we perform a first-order expansion of the propagation constants around the phase-matched frequencies, i. e. those that obey $2\beta_\mathrm{p}(\omega_{\mathrm{p}_0}) = \beta_\mathrm{i}(\omega_{\mathrm{i}_0}) + \beta_\mathrm{s}(\omega_{\mathrm{s}_0})$ where ω_{p_0} is the pump center frequency. Doing so, with the understanding that $\bar{\omega}_j = \omega_j - \omega_{j_0}$, the wavenumber mismatch $\Delta\beta$ reads:

$$\begin{aligned}
\Delta\beta(\omega_\mathrm{p}, \omega_\mathrm{i}, \omega_\mathrm{s}) \approx \; & \beta_\mathrm{p}(\omega_{\mathrm{p}_0}) + \beta_\mathrm{p}^{(1)}\bar{\omega}_\mathrm{p} + \beta_\mathrm{p}(\omega_{\mathrm{p}_0}) + \beta_\mathrm{p}^{(1)}(\omega_\mathrm{i} + \omega_\mathrm{s} - \omega_\mathrm{p} - \omega_{\mathrm{p}_0}) \\
& - \beta_\mathrm{i}(\omega_{\mathrm{i}_0}) - \beta_\mathrm{i}^{(1)}\bar{\omega}_\mathrm{i} - \beta_\mathrm{s}(\omega_{\mathrm{s}_0}) - \beta_\mathrm{s}^{(1)}\bar{\omega}_\mathrm{s} \\
= \; & \beta_\mathrm{p}^{(1)}\bar{\omega}_\mathrm{p} + \beta_\mathrm{p}^{(1)}(\bar{\omega}_\mathrm{i} + \bar{\omega}_\mathrm{s} - \bar{\omega}_\mathrm{p}) - \beta_\mathrm{i}^{(1)}\bar{\omega}_\mathrm{i} - \beta_\mathrm{s}^{(1)}\bar{\omega}_\mathrm{s} \\
= \; & \left(\beta_\mathrm{p}^{(1)} - \beta_\mathrm{i}^{(1)}\right)\bar{\omega}_\mathrm{i} + \left(\beta_\mathrm{p}^{(1)} - \beta_\mathrm{s}^{(1)}\right)\bar{\omega}_\mathrm{s} \equiv \Delta\beta(\bar{\omega}_\mathrm{i}, \bar{\omega}_\mathrm{s}).
\end{aligned} \tag{2.50}$$

Notably, the wavenumber mismatch has now become independent of the integration variable in Eq. (2.49), which makes dealing with the integral much more straightforward as the phase-matching function Φ can be moved outside the integral.

If we consider a pump with a Gaussian spectrum $\alpha_\mathrm{p}(\bar{\omega}) \propto \exp[-\bar{\omega}^2/\Omega^2]$, where Ω is related to the pump bandwidth, then [47]

$$\mathcal{A}(\bar{\omega}_\mathrm{i}, \bar{\omega}_\mathrm{s}) \propto \exp\left[-\frac{(\bar{\omega}_\mathrm{i} + \bar{\omega}_\mathrm{s})^2}{2\Omega^2}\right] \mathrm{sinc}\left(\frac{\beta_\mathrm{pi}\bar{\omega}_\mathrm{i} + \beta_\mathrm{ps}\bar{\omega}_\mathrm{s}}{2} l\right) \exp\left[i\Delta\beta(\bar{\omega}_\mathrm{i}, \bar{\omega}_\mathrm{s})l/2\right], \tag{2.51}$$

where we have introduced the notation $\beta_{jk} \equiv \beta_j^{(1)} - \beta_k^{(1)}$. From Eq. (2.51), we see that the JSA has become a simple product between an energy-matching function (the Gaussian function), and a first-order phase-matching function (the sinc function). The complex exponential contains only linear terms in $\bar{\omega}_\mathrm{i}$ and $\bar{\omega}_\mathrm{s}$ (shifts in time), and does therefore not contribute with any correlation. Our analysis may be simplified further by introducing the normalized frequencies $\bar{\Omega}_j = \bar{\omega}_j/\Omega$. This allows us to write the JSA in terms of dimensionless variables:

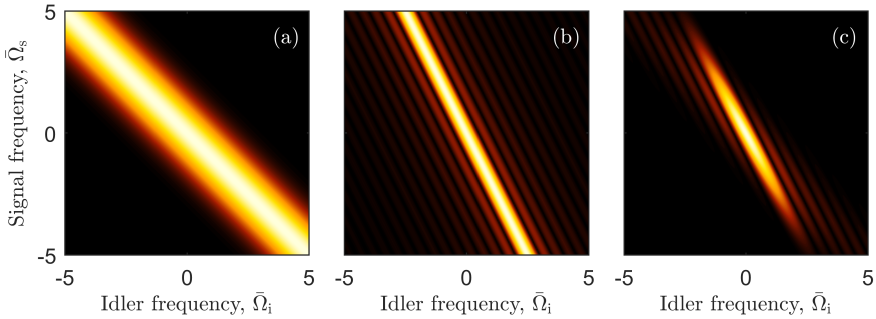

Figure 2.5: Absolute value of (a) energy-matching function, (b) phase-matching function, and (c) the resulting joint spectral amplitude. Parameters used are $\zeta_{\mathrm{pi}} = 4$, $\zeta_{\mathrm{ps}} = 2$.

$$\mathcal{A}(\bar{\Omega}_{\mathrm{i}}, \bar{\Omega}_{\mathrm{s}}) \propto \exp\left[-\frac{\left(\bar{\Omega}_{\mathrm{i}} + \bar{\Omega}_{\mathrm{s}}\right)^2}{2}\right] \mathrm{sinc}\left(\frac{\zeta_{\mathrm{pi}}\bar{\Omega}_{\mathrm{i}} + \zeta_{\mathrm{ps}}\bar{\Omega}_{\mathrm{s}}}{2}\right), \tag{2.52}$$

where we have left out the complex exponential and introduced the parameters $\zeta_{\mathrm{p}j} = \beta_{\mathrm{p}j}\Omega l$, which are dimensionless measures of the walk off between the pump and the signal-idler photons. These two parameters fully determine the shape of the JSA and thereby the spectral correlation between the two photons. In particular, their ratio $\zeta_{\mathrm{pi}}/\zeta_{\mathrm{ps}} = \beta_{\mathrm{pi}}/\beta_{\mathrm{ps}}$, which in an experimental scenario may be varied through careful waveguide- and group-velocity engineering, determines the orientation of the phase-matching function [47, 48], while their magnitudes $|\zeta_{\mathrm{p}j}|$ decide the width of the phase-matching function. As an example, Fig. 2.5 shows (a) an energy-matching function, (b) the absolute value of a phase-matching function for $\zeta_{\mathrm{pi}} = 2\zeta_{\mathrm{ps}} = 4$, and (c) the resulting JSA. In this example, the JSA exhibits a large degree of spectral correlation. In particular the joint spectrum is seen to be anti-correlated, so that large idler frequencies are connected to low signal frequencies, and *vice versa*.

The anti-correlation seen in Fig. 2.5 is frequently encountered due to the fact that the energy-matching function is, as a result of energy conservation, by itself inherently anti-correlated. However, the orientation of the phase-matching function depends on the fraction $\zeta_{\mathrm{pi}}/\zeta_{\mathrm{ps}}$, and therefore it is expected that by changing the values of ζ_{pi} and ζ_{ps} we may tune the degree of spectral correlation between the signal and idler photon. To illustrate this, Fig. 2.6 shows the purity calculated through Eq. (2.41) in a two-dimensional contour plot versus ζ_{pi} and ζ_{ps} (yellow areas correspond to high purity and therefore a low degree of spectral correlation). The purity, which is seen to be symmetric with respect to the lines $\zeta_{\mathrm{pi}} = \zeta_{\mathrm{ps}}$ and $\zeta_{\mathrm{pi}} = -\zeta_{\mathrm{ps}}$, has two (identical) branches of high purity values. Building sources of high-purity heralded single photons therefore involves tailoring the phase-matching properties of nonlinear waveguides such that one ends up in one of these branches. Based on experimental efforts, we may define two different schemes, which we in the following consider in turn.

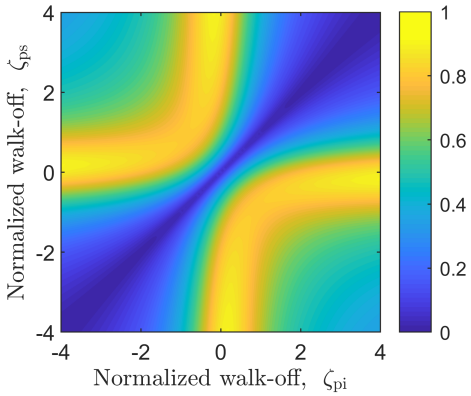

Figure 2.6: Spectral purity versus the two normalized walk-off parameters ζ_{pi} and ζ_{ps}.

2.5.2 The symmetric scheme

We first examine the so-called symmetric case, where the group velocity is approximately an average of that of the signal and idler, i.e. $\beta_{\mathrm{pi}} \approx -\beta_{\mathrm{ps}}$. In this case, the orientation of the phase-matching function [see Fig. 2.5(b)], which is determined by the fraction $\beta_{\mathrm{pi}}/\beta_{\mathrm{ps}} \approx -1$, is approximately perpendicular to the energy-matching function [see Fig. 2.5(a)]. By further optimizing the product of the bandwidth-length product Ωl, one ends up with a JSA that takes the form shown in Fig. 2.7(a), obtained for $\beta_{\mathrm{i}}^{(1)} > \beta_{\mathrm{p}}^{(1)} > \beta_{\mathrm{s}}^{(1)}$. Evidently, in this case the JSA is composed of an uncorrelated center peak accompanied by sidelobes that are due to the sinc-function. These sidelobes introduce spectral correlation resulting in a spectral purity of $\mathcal{P} \approx 0.8$.

Figure 2.7(b) shows the JTA obtained by performing a 2D inverse Fourier transformation of the JSA in Fig. 2.7(a). The JTA exhibits very abrupt edges perpendicular to the 45°-direction which are due to the sinc lobes in the spectral domain[4]. From a temporal point-of-view these two edges are consequences of the sudden change of nonlinear interaction as the pump pulse enters (4th quadrant) and exits (2nd quadrant) the nonlinear waveguide. To realize this, one can use the following arguments: Firstly, a photon pair which is generated at the very end of the waveguide will exit the waveguide simultaneously corresponding to the line parametrized as $t_{\mathrm{i}} = t_{\mathrm{s}}$, i.e. the upper left edge. Secondly, for a pair generated at the waveguide beginning, the idler photon will, at the waveguide output, trail the signal by $\beta_{\mathrm{is}} l$, parametrized by the line $t_{\mathrm{s}} = t_{\mathrm{i}} - \beta_{\mathrm{is}}$, i.e. the bottom right edge. Thus, while the shape and orientation of the JTA comes from the relative group velocities, the waveguide length, and the pulse width, the abrupt edges are a direct consequence of both causality and the instantaneous nature of the Kerr effect.

[4]The Fourier transform of a square function is a sinc function.

2.5.3 The asymmetric scheme

In the asymmetric case, the signal- and idler fields are phase-matched at a set of frequencies such that one is group-velocity matched to the pump and the other is strongly group-velocity *mis*matched to the pump. With these relative group velocities the phase-matching function becomes either horizontally oriented ($\beta_{\mathrm{pi}} = 0$) or vertically elongated ($\beta_{\mathrm{ps}} = 0$). By simultaneously ensuring a large relative walk-off to the group-velocity mismatched field, obtained through a large value of $\beta_{\mathrm{p}j}\Omega l$, we acquire a phase-matching function that is spectrally very narrow compared to the energy-matching function. An example of a resulting JSA, for which it is the idler that is group-velocity mismatched, is seen in Fig. 2.8(a). Notably, the JSA, which as expected still contains the characteristic sidelobes, becomes strongly asymmetric in the signal- and idler frequencies. In particular it is spectrally narrow in the idler frequency, which is the group-velocity matched sideband. To understand this feature, we inspect the corresponding JTA depicted in Fig. 2.8(b). Like in the symmetric case, the JTA exhibits the distinctive edges that are due to the waveguide endpoints. However, due to the fact that the signal is group-velocity matched to the pump, the contours of the JTA are now horizontally aligned. This expresses the fact that, regardless of where the photon pair is generated, the output time, and the temporal profile, of the signal remains the same (apart from the edge contributions). On the other hand, the temporal distribution of the idler is strongly temporally stretched with a temporal duration of approximately $\beta_{\mathrm{is}}l$. This elongation, which also explains why the JSA is spectrally squeezed in the direction of the idler, is again due to the temporal walk-off between idler components generated throughout the waveguide.

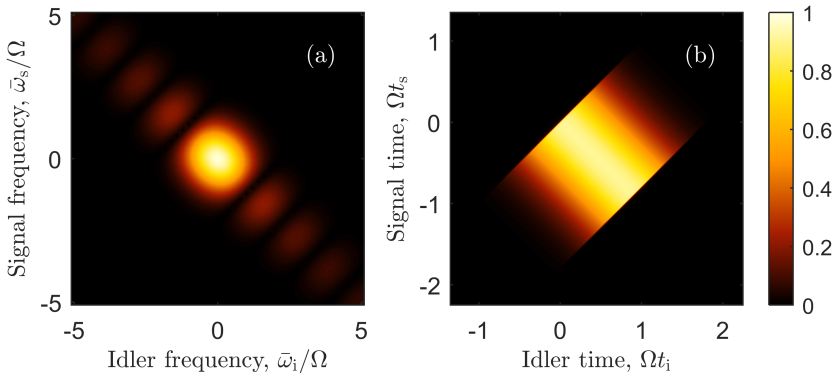

Figure 2.7: (a) Joint spectral amplitude and (b) joint temporal amplitude for $\zeta_{\mathrm{ps}} = 9/10 = -\zeta_{\mathrm{pi}}$. Frequency- and time variables are normalized to the pump spectral width Ω as this facilitates universal plots of the JSA and JTA for a given set of ζ_{pi} and ζ_{ps}. The calculated purity is $\mathcal{P} \approx 0.80$.

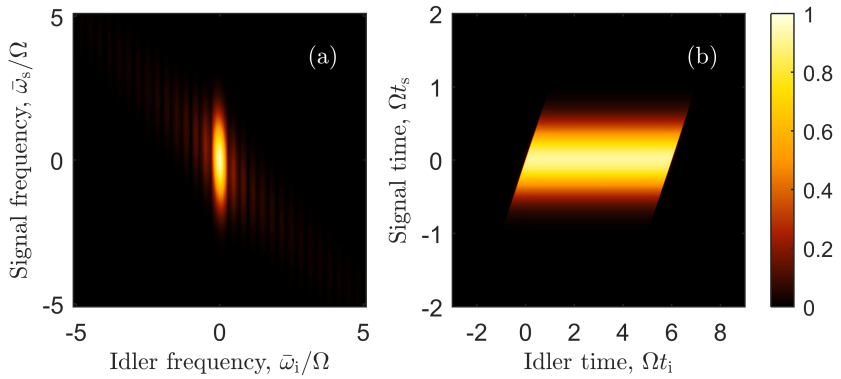

Figure 2.8: (a) Joint spectral amplitude and (b) joint temporal amplitude for $\zeta_{pi} = -6$ and $\zeta_{ps} = 0$. The calculated purity is $\mathcal{P} \approx 0.92$.

2.6 Summary

In this chapter, we have provided the theoretical framework necessary for understanding the main theoretical work in this thesis contained in Chapters 3, 4, and 5. We began by a quick introduction to third-order nonlinear optics, followed by a quantum-mechanical treatment of two-mode squeezing and spontaneous four-wave mixing, with particular focus on photon-pair generation. In the latter part of the chapter we considered, in detail, the properties of biphoton quantum states with emphasize on heralded single photons for high-visibility quantum interference.

Part II

Spontaneous four-wave mixing

CHAPTER 3

Tailored photon-pair generation in a birefringent waveguide

In this this chapter, which is an extended version of the work in [49, 50], we propose and analyse the use of cross-polarized four-wave mixing for generating completely uncorrelated photon pairs in a birefringent nonlinear waveguide. Our novel Heisenberg-picture approach to describing the spontaneous four-wave mixing process allows us to assess the influence of self- and cross-phase modulation.

3.1 Introduction

As outlined in Chapter 2, there are two common schemes (the *symmetric* and the *asymmetric*) for minimizing temporal-spectral correlation in photon pairs generated from travelling-wave parametric sources. The symmetric scheme, originally proposed by W. Grice *et al.* [42], relies on phase-matching the signal and idler fields such that the group velocity of the pump lies in between that of the signal and idler. Additionally, the waveguide length must be optimized such that the phase-matching function acquires approximately the same spectral width as the pump spectrum, or *vice versa* (see Chapter 2 for details). This scheme has been experimentally demonstrated on various nonlinear platforms such as periodically poled $KTiOPO_4$ (PPKTP) [32], birefringent silica fibers [51, 52], and integrated silica waveguides [53, 54]. The asymmetric scheme [48], instead relies on perfectly group-velocity matching the signal (idler) to the pump and enabling a large walk off to the idler (signal). In effect, the joint spectral amplitude becomes strongly elongated in one direction, as have been shown experimentally using second-order-nonlinear KDP crystals [55] and birefringent micro-structured fibers [56, 57, 58, 59].

In implementations of the two original schemes, the generation of *completely* uncorrelated photon pairs necessitates the use of spectral filters to "cut out" the correlated parts of the signal-idler spectra. However, such filtering comes at the expense of photon losses, and thereby a reduction in the (two-sided) heralding efficiency [60, 61], which ultimately could prevent up-scaling to many-photon experiments using, etc. various multiplexing techniques [62, 63]. Moreover, recent studies on the use of SFWM have indicated that the accompanying effects of nonlinear phase modulation (NPM)[1], as well as group-velocity disperison (GVD), may introduce significant spectral correlation in the two-photon state [64, 65].

The schemes originally proposed for generating uncorrelated photon pairs suffer from a small degree of spectral correlation, which comes from the characteristic sidelobes of the phase-matching function. These sidelobes arise due to the abrupt temporal changes in the nonlinear interaction as the travelling pump pulse enters, and later on, exits the nonlinear medium. A solution to this issue was offered by A. Brańczyk *et al.* who suggested to tailor a second-order nonlinear crystal to have a Gaussian-like nonlinearity profile by introducing a longitudinal variation in the poling period of a second-order nonlinear crystal or waveguide [66, 67]. Such a longitudinal variation in the interaction can be realized in an alternative manner by using two pump pulses that collide with each other in a third-order nonlinear waveguide. As proposed by Fang *et al.* [68], this may be achieved relying on the dispersive property of the nonlinear waveguide and thereby using two pump pulses of different center wavelengths. We here follow a different road than Fang *et al.*, and consider the case where the two pump pulses are orthogonal in polarization, which, in a birefringent waveguide, enables the relative pump-pump walk-off [49, 50]. This approach, which can also be realized using higher-order spatial modes in a multi-mode waveguide [69, 70, 71, 72], is significantly simpler in implementation as the two pump pulses may originate from the same pulsed laser source. Moreover, our approach turns out to directly enable the group-velocity matching required for high-purity heralded single-photon generation, and be highly resilient to both NPM- and GVD effects [49, 65].

This chapter is organized as follows: In Sec. 3.2 we introduce the (type-II) cross polarized FWM process and its phase-matching properties. In Sec. 3.3 we analyse the dynamics of dual-pump FWM, and solve the coupled-mode equations governing the propagation of the classical pumps and the quantum-mechanical sidebands. We further establish a perturbative connection between the Heisenberg-picture transfer functions and the Scrödinger-picture two-photon amplitude. The resulting two-photon amplitude for photon pairs generated by type-II SFWM is analysed in Sec. 3.4. Finally, in Sec. 3.5 we discuss and summarize the results of the chapter.

[1] We use the phrase "nonlinear phase modulation" to refer to the combined effect of self- and cross phase modulation.

3.2 Type-II four-wave mixing

We consider the type-II FWM interaction shown in Fig. 3.1(a). In this process, two cross-polarized pumps (p and q) at a degenerate frequency[2] interact in a birefringent third-order nonlinear waveguide, and generate cross-polarized signal- (s) and idler (i) fields at non-degenerate frequencies. Conservation of energy requires that

$$\hbar\left(\omega_{\mathrm{p}}+\omega_{\mathrm{q}}-\omega_{\mathrm{s}}-\omega_{\mathrm{i}}\right)=0, \tag{3.1}$$

which is fulfilled for all symmetric displacements $\delta\omega=\omega_{\mathrm{p,q}}-\omega_{\mathrm{s}}=\omega_{\mathrm{i}}-\omega_{\mathrm{p,q}}$. In addition, efficient cumulative interaction requires the relative phases of the four participating fields to be constant. This phase-matching requirement, which physically stems from momentum conservation, is formulated in terms of the wavenumber mismatch

$$\Delta\beta=\beta_x(\omega_{\mathrm{p}})+\beta_y(\omega_{\mathrm{q}})-\beta_x(\omega_{\mathrm{s}})-\beta_y(\omega_{\mathrm{i}}), \tag{3.2}$$

which must vanish for efficient FWM. In Eq. (3.2) we have neglected a nonlinear pump-power dependent term to the wavenumber mismatch as we are operating in the low-generation regime in which signal-idler photon pairs are generated with low probability. Equation (3.2) therefore only depends on the frequency- and polarization dependent wavenumber $\beta_j(\omega)$, where the subindex j refers to the polarization. We assume that the birefringent waveguide may be modelled by writing the wavenumbers as

$$\beta_j(\omega)=\beta_j^{(0)}+\beta_j^{(1)}(\omega-\omega')+\frac{\beta_j^{(2)}}{2}(\omega-\omega')^2+\mathcal{O}(\omega-\omega')^3, \tag{3.3}$$

where we have performed a series expansion around a reference angular frequency ω'. If we now let $\omega'=\omega_{\mathrm{p}}=\omega_{\mathrm{q}}$ and insert Eq. (3.3) into Eq. (3.2), then using $\delta\omega=\omega'-\omega_{\mathrm{s}}$ we find

$$\begin{aligned}\Delta\beta&=\beta_x^{(0)}+\beta_y^{(0)}-\left[\beta_x^{(0)}+\beta_x^{(1)}(-\delta\omega)+\frac{\beta_x^{(2)}}{2}(-\delta\omega^2)+\beta_y^{(0)}+\beta_y^{(1)}\delta\omega+\frac{\beta_y^{(2)}}{2}\delta\omega^2\right]\\&=\left(\beta_x^{(1)}-\beta_y^{(1)}\right)\delta\omega-\left(\frac{\beta_x^{(2)}+\beta_y^{(2)}}{2}\right)\delta\omega^2.\end{aligned} \tag{3.4}$$

By requiring $\Delta\beta=0$ in expression 3.4, we find the following phase-matching criterion for the type-II FWM process:

$$\delta\omega=\frac{\Delta\beta_1}{\beta_{2,\mathrm{av}}}, \tag{3.5}$$

where we have defined $\Delta\beta_1\equiv\beta_x^{(1)}-\beta_y^{(1)}$ and $\beta_{2,\mathrm{av}}\equiv(\beta_x^{(2)}+\beta_y^{(2)})/2$. Thus, the sideband-pump detuning depends only on the inverse group-velocity difference of the two polarization modes and the average experienced GVD [73].

[2]The process is easily generalized to the two pumps being at non-degenerate frequencies.

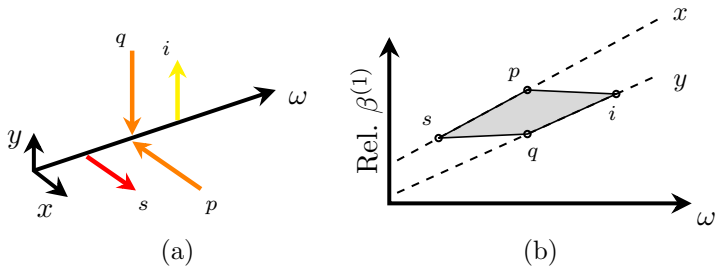

Figure 3.1: Sketch of type-II FWM.

The phase-matching condition described by Eq. (3.5) has a remarkably simple visual interpretation as sketched in Fig. 3.1(b) [74, 69]. By plotting the two curves of $\beta^{(1)}(\omega)$, the phase-matching condition takes the form of a parallelogram, which is increasingly skewed for increasing deviations between $\beta_x^{(2)}$ and $\beta_y^{(2)}$. Focusing on waveguides where the group-velocity dispersion is similar for the two waveguide polarization modes, the signal (idler) becomes nearly group-velocity matched to the orthogonally polarized pump q (pump p). Specifically, we find that

$$\delta\beta_1 = \beta_y^{(1)}(\omega_\mathrm{q}) - \beta_x^{(1)}(\omega_\mathrm{s}) = \beta_x^{(1)}(\omega_\mathrm{p}) - \beta_y^{(1)}(\omega_\mathrm{i}) = |\beta_{2,\mathrm{av}} - \beta_{x,y}^{(2)}| \frac{\Delta\beta_1}{\beta_{2,\mathrm{av}}}. \tag{3.6}$$

Notably, if the group-velocity dispersion is polarization independent, then $\delta\beta_1 = 0$ so that each sideband is group-slowness matched to the pump in the orthogonal polarization. This group-slowness matching shall become important later on in this chapter.

As it appears from Eq. (3.5), this cross-polarized form of FWM may be observed in either the normal dispersion regime ($\beta^{(2)} > 0$), or in the anomalous dispersion regime ($\beta^{(2)} < 0$). The process has been demonstrated in birefringent optical fibers in both of these regimes [75, 73, 76], in situations where it was stimulated by signal- and idler vacuum fluctuations (so-called modulation-instability). Notably, the cross-polarized FWM process has a narrow phase-matching bandwidth, which may be far detuned from the pump frequency. This stands in stark contrast to the scalar FWM process, which can exhibit many THz of bandwidth in waveguides tailored to have flat and near-zero anomalous dispersion [77, 78]. Moreover, as is apparent from Fig. 3.1(b), the cross-polarized FWM process can be highly tunable in frequency, which allows tuning of the signal- and idler frequencies, merely by changing the pump frequency.

3.3 Four-wave mixing: underlying dynamics

To model the SFWM process we here follow an alternative approach compared to the usual Scrödinger-picture framework which was outlined in Chapter 2. Instead,

we consider the Heisenberg picture equations of motion for the four involved fields, which may be derived from first principles or by invoking the correspondence principle[79]. This approach permits us to directly include the effect of NPM in the analysis, an important addition given that this effect is inherently of the same order of magnitude as the FWM interaction. By further including inter-pulse dispersion, the governing coupled-mode equation (CMEs) take the form [2]

$$\left(\partial_z + \beta_{\mathrm{p}}^{(1)}\partial_t\right) A_{\mathrm{p}} = i\gamma\left(|A_{\mathrm{p}}|^2 + \epsilon_{\mathrm{pq}}|A_{\mathrm{q}}|^2\right) A_{\mathrm{p}}, \tag{3.7a}$$

$$\left(\partial_z + \beta_{\mathrm{q}}^{(1)}\partial_t\right) A_{\mathrm{q}} = i\gamma\left(|A_{\mathrm{q}}|^2 + \epsilon_{\mathrm{pq}}|A_{\mathrm{p}}|^2\right) A_{\mathrm{q}}, \tag{3.7b}$$

$$\left(\partial_z + \beta_{\mathrm{i}}^{(1)}\partial_t\right) \hat{a}_{\mathrm{i}} = i\gamma\left(\epsilon_{\mathrm{ip}}|A_{\mathrm{p}}|^2 + \epsilon_{\mathrm{iq}}|A_{\mathrm{q}}|^2\right) \hat{a}_{\mathrm{i}} + i\gamma\epsilon A_{\mathrm{p}} A_{\mathrm{q}} \hat{a}_{\mathrm{s}}^\dagger, \tag{3.7c}$$

$$\left(\partial_z + \beta_{\mathrm{s}}^{(1)}\partial_t\right) \hat{a}_{\mathrm{s}} = i\gamma\left(\epsilon_{\mathrm{sp}}|A_{\mathrm{p}}|^2 + \epsilon_{\mathrm{sq}}|A_{\mathrm{q}}|^2\right) \hat{a}_{\mathrm{s}} + i\gamma\epsilon A_{\mathrm{p}} A_{\mathrm{q}} \hat{a}_{\mathrm{i}}^\dagger, \tag{3.7d}$$

where ∂_z and ∂_t denote partial differentiation w.r.t. position and time, $\hat{a}_{\mathrm{i,s}}$ are the idler and signal slowly varying quantum fields, $A_{\mathrm{p,q}}$ are the complex slowly varying envelope of the pumps, $\beta_j^{(1)} = \partial_\omega \beta(\omega)|_{\omega=\omega_j}$ is the group slowness at the frequency of the jth field, and γ is the (assumed common) nonlinear coupling coefficient proportional to the intensity-dependent refractive index n_2. Moreover, as we wish to describe a FWM process among two different polarization component, Eqs. (3.7) contain the polarization-dependent nonlinear coupling coefficients ϵ_{jk} and ϵ. In an amorphous material, such as a silica, the third-order susceptibility $\chi^{(3)}$ has the tensorial property that $\chi^{(3)}_{xxyy} = \chi^{(3)}_{xyyx} = \chi^{(3)}_{xyxy} = \chi^{(3)}_{xxxx}/3 = \chi^{(3)}_{yyyy}/3$. For this reason, the XPM-coefficients ϵ_{jk} equal 2 for optical fields j and k that are co-polarized, while the corresponding value for cross-polarized fields is $2/3$. Similarly, the FWM-coefficient ϵ is 2 if all four fields are co-polarized and $2/3$ for pairwise co-polarized fields which are orthogonally polarized with respect to the two remaining fields.

3.3.1 The pump dynamics

In Eq. (3.7), we have made the realistic, and common, assumption that the weak sidebands do not influence the classical pumps. This enables us to solve Eqs. (3.7a) and (3.7b) independently from Eqs. (3.7c) and (3.7d). The pump evolutions may be found to satisfy [80]

$$A_{\mathrm{p}}(z,t) = \left[F_{\mathrm{p}}(\xi_{\mathrm{p}})\right]^{1/2} \exp\left[i\phi_{\mathrm{p}}(z,t)\right], \tag{3.8}$$

$$A_{\mathrm{q}}(z,t) = \left[F_{\mathrm{q}}(\xi_{\mathrm{q}})\right]^{1/2} \exp\left[i\phi_{\mathrm{q}}(z,t)\right], \tag{3.9}$$

where the retarded times $\xi_{\mathrm{p,q}} = t - \beta_{\mathrm{p,q}} z$ determine the pump propagation of the envelope $F_{\mathrm{p,q}}(\xi_{\mathrm{p,q}}) = |A_{\mathrm{p,q}}(0,t)|^2$, and we have adopted the convenient notation $\beta_j \equiv \beta_j^{(1)}$. Furthermore, the pump phases $\phi_{\mathrm{p,q}}$, which start out as $\phi_{\mathrm{p,q}}(0,t) =$

$\phi_{\mathrm{p}_0,\mathrm{q}_0}(t)$, are given as

$$\phi_{\mathrm{p}}(z,t) = \phi_{p0}(t) + \gamma F_{\mathrm{p}}(\xi_{\mathrm{p}})z + \frac{\epsilon_{\mathrm{pq}}\gamma}{\beta_{\mathrm{pq}}} \int_{\xi_{\mathrm{p}}}^{\xi_{\mathrm{q}}} \mathrm{d}\tau \; F_{\mathrm{q}}(\tau), \tag{3.10}$$

$$\phi_{\mathrm{q}}(z,t) = \phi_{\mathrm{q}_0}(t) + \gamma F_{\mathrm{q}}(\xi_{\mathrm{q}})z + \frac{\epsilon_{\mathrm{pq}}\gamma}{\beta_{\mathrm{pq}}} \int_{\xi_{\mathrm{p}}}^{\xi_{\mathrm{q}}} \mathrm{d}\tau \; F_{\mathrm{p}}(\tau), \tag{3.11}$$

with $\beta_{\mathrm{pq}} = \beta_{\mathrm{p}} - \beta_{\mathrm{q}}$. Thus, from Eqs. (3.8)–(3.11), it is readily seen that the pumps evolve with unaltered shapes, while their phase profiles change due to the effects of NPM.

3.3.2 The signal-idler dynamics

The signal- and idler-mode operators, which are governed by Eqs. (3.7c) and (3.7d), additionally satisfy the Bosonic commutation relations

$$[\hat{a}_m(z,t), \hat{a}_n(z,t')] = 0, \qquad \left[\hat{a}_m(z,t), \hat{a}_n^\dagger(z,t')\right] = \delta_{mn}\delta(t-t'), \tag{3.12}$$

where $m, n \in \{\mathrm{i}, \mathrm{s}\}$, and δ_{mn} and $\delta(t)$ are the Kronecker and Dirac delta functions, respectively. Due to the linearity of Eqs. (3.7c) and (3.7d) in the mode operators, their solution may be written in a linear quantum input-output form (see also Appendix C). Denoting by $\hat{b}_{\mathrm{i,s}}(t)$ the output mode operators at $z = l$ and output time t, and by $\hat{a}_{\mathrm{i,s}}(t')$ the input mode operators at $z = 0$ and input time t', the input-output linear Bogoulibov transformation is

$$\hat{b}_{\mathrm{i}}(t) = \int_{-\infty}^{\infty} \mathrm{d}t' \left[G_{\mathrm{ii}}(t,t')\hat{a}_{\mathrm{i}}(t') + G_{\mathrm{is}}(t,t')\hat{a}_{\mathrm{s}}^\dagger(t')\right], \tag{3.13}$$

$$\hat{b}_{\mathrm{s}}(t) = \int_{-\infty}^{\infty} \mathrm{d}t' \left[G_{\mathrm{ss}}(t,t')\hat{a}_{\mathrm{s}}(t') + G_{\mathrm{si}}(t,t')\hat{a}_{\mathrm{i}}^\dagger(t')\right], \tag{3.14}$$

where G_{mn} are the Green (transfer) functions associated with the governing coupled-mode equations. These Green functions depend implicitly on the waveguide length l, inverse group velocities β_j, and the input profiles of the pumps. Furthermore, as the output mode operators $\hat{b}_{\mathrm{i,s}}$ are subject to the same commutation relations as those in Eq. (3.12), one can establish that the following constraints apply to

the set of Green functions:

$$\left[\hat{b}_{\rm i}(t_{\rm i}),\hat{b}_{\rm i}^{\dagger}(t_{\rm i}')\right]=\int_{-\infty}^{\infty}{\rm d}t'\left[G_{\rm ii}(t_{\rm i},t')G_{\rm ii}^{*}(t_{\rm i}',t')-G_{\rm is}(t_{\rm i},t')G_{\rm is}^{*}(t_{\rm i}',t')\right]=\delta(t_{\rm i}-t_{\rm i}'),\tag{3.15}$$

$$\left[\hat{b}_{\rm i}(t_i),\hat{b}_{\rm s}(t_{\rm s})\right]=\int_{-\infty}^{\infty}{\rm d}t'\left[G_{\rm ii}(t_{\rm i},t')G_{\rm si}(t_{\rm s},t')-G_{\rm is}(t_{\rm i},t')G_{\rm ss}(t_{\rm s},t')\right]=0.\tag{3.16}$$

Since Eqs. (3.13) and (3.14) are symmetric with respect to the indices i and s, similar constraints apply upon performing the substitution i $\leftrightarrow$ s in Eqs. (3.15) and (3.16).

With the framework of the signal- and idler evolution in place, we next derive the governing (perturbative) Green functions.

3.3.3 The perturbative Green functions

By definition, and as seen from Eqs. (3.13) and (3.14), the Green functions represent the effects caused by impulse signal- and idler inputs. In the following we focus on the Green functions related to a signal input, i.e. $G_{\rm ss}$ and $G_{\rm is}$, and note that the other pair is obtained in a completely analogous way.

First, consider the problem of attaining the self-Green function $G_{\rm ss}$. In the perturbative regime, the nonlinear interaction is considered weak, which means that we may neglect the effect of a generated idler photon further stimulating the nonlinear process. This is in agreement with the perturbative formulation in Chapter 2. This further means that, as we here consider the case of a signal input, we may ignore the FWM term in Eq. (3.7d). With $A_{\rm p}(z,t)$ and $A_{\rm q}(z,t)$ already given, we find that the signal at the output $z=l$ is given as

$$\hat{b}_{\rm s}(t)\equiv\hat{a}_{\rm s}(l,t)=\hat{a}_{\rm s}(0,t-\beta_{\rm s}l)\exp\left[i\phi_{\rm s}(l,t)\right],\tag{3.17}$$

where $\phi_{\rm s}(l,t)$ is due to XPM from the two pump pulses, and, similarly to Eqs. (3.10) and (3.11), explicitly reads

$$\phi_{\rm s}(l,t)=\gamma\sum_{j={\rm p,q}}\frac{\epsilon_{{\rm s}j}}{\beta_{{\rm s}j}}\int_{t-\beta_{\rm s}l}^{t-\beta_j l}{\rm d}\tau\ F_j(\tau),\tag{3.18}$$

taking into account the potential walk-off effect between the signal and the pumps. We may reformulate Eq. (3.17) as

$$\hat{b}_{\rm s}(t)=\int{\rm d}t'\ \delta(t-t'-\beta_{\rm s}l)\exp\left[i\phi_{\rm s}(l,t)\right]\hat{a}_{\rm s}(0,t'),\tag{3.19}$$

which allows identification of the Green function G_{ss} as

$$G_{\mathrm{ss}}(t,t') = \delta(t - t' - \beta_{\mathrm{s}} l) \exp\left[i\phi_{\mathrm{s}}(l,t)\right]. \tag{3.20}$$

Notably, the self-Green function G_{ss} is seen to be divided into a part describing linear propagation and a part describing XPM.

Proceeding with G_{is}, we use the time-domain collision method formulated in [80, 81]. This method relies on the Green functions being the solutions to impulse inputs, justifying an analysis based on a ray picture. Consider therefore an input signal-ray moving along the line from $(0,t')$ to $(l,t'+\beta_{\mathrm{s}} l)$. Then the generated idler-ray exiting the waveguide at (l,t) is bound to having been created at the collision point (z_c,t_c), given by [81]

$$z_c = \frac{t' - (t - \beta_{\mathrm{i}} l)}{\beta_{\mathrm{is}}}, \quad t_c = \frac{\beta_{\mathrm{i}} t' - \beta_{\mathrm{s}}\,(t - \beta_{\mathrm{i}} l)}{\beta_{\mathrm{is}}}, \tag{3.21}$$

and we assumed that $\beta_{\mathrm{is}} > 0$. The effect of FWM is present only in the collision region, which is infinitesimally thin due to the impulse s-input. The interaction is therefore captured by integrating Eq. (3.7c) across the collision 'point' while neglecting the XPM terms. This yields the intermediate (collision) Green function

$$G_{\mathrm{is}}^{(c)}(t,t') = i\epsilon\bar{\gamma}(z_c,t_c) \exp\left[i\Phi(z_c,t_c)\right], \tag{3.22}$$

where $\bar{\gamma}(z,t) = \gamma\left[F_{\mathrm{p}}(t-\beta_{\mathrm{p}} z) F_{\mathrm{q}}(t-\beta_{\mathrm{q}} z)\right]^{1/2}/\beta_{\mathrm{is}}$, and $\Phi(z,t) = \phi_{\mathrm{p}}(z,t) + \phi_{\mathrm{q}}(z,t) - \phi_{\mathrm{s}}(z,t)$ is the relative phase carried over to the idler field. After the collision, while propagating to the waveguide output (l,t), the generated idler solely experiences XPM from the pumps, and acquires the residual phase [compare with Eq. (3.18)]

$$\phi_{\mathrm{i}}^{(r)}(l,t) = \gamma \sum_{j=\mathrm{p,q}} \frac{\epsilon_{\mathrm{i}j}}{\beta_{\mathrm{i}j}} \int_{t_c-\beta_j z_c}^{t-\beta_j l} \mathrm{d}\tau\ F_j(\tau). \tag{3.23}$$

This phase can be coherently added to Eq. (3.22) yielding the final form of G_{is}

$$G_{\mathrm{is}}(t,t') = i\epsilon\bar{\gamma}(z_c,t_c) \exp\left[i\Phi(z_c,t_c) + i\phi_{\mathrm{i}}^{(r)}(l,t)\right] \mathrm{H}(t'-t+\beta_{\mathrm{i}} l)\mathrm{H}(t-t'-\beta_{\mathrm{s}} l), \tag{3.24}$$

where the Heaviside step functions $\mathrm{H}(t)$ enforce the causal requirement that the nonlinear interaction is bounded to within the waveguide, i.e. $0 < z_c < l$.

3.3.4 Joint temporal amplitude

In the Schrödinger picture, the photon-pair state generated by SFWM is of the form (see Chapter 2)

$$|\Psi_{\mathrm{II}}\rangle = \int_{-\infty}^{\infty}\int_{-\infty}^{\infty} \mathrm{d}t_{\mathrm{i}}\mathrm{d}t_{\mathrm{s}}\ \mathcal{A}(t_{\mathrm{i}},t_{\mathrm{s}})\hat{a}_{\mathrm{i}}^{\dagger}(t_{\mathrm{i}})\hat{a}_{\mathrm{s}}^{\dagger}(t_{\mathrm{s}})\,|0,0\rangle\,, \tag{3.25}$$

where the JTA, $\mathcal{A}(t_{\mathrm{i}},t_{\mathrm{s}})$, describes the temporal correlation in the signal-idler photon pair at the *output* of the waveguide. It turns out that it is possible to attain the JTA from the Scrödinger picture by use of the Heisenberg picture Green functions. As shown in Appendix D, the JTA is connected to the Green functions according to

$$\mathcal{A}(t_{\mathrm{i}},t_{\mathrm{s}}) = \int_{-\infty}^{\infty} \mathrm{d}t' G_{\mathrm{is}}(t_{\mathrm{i}},t')G_{\mathrm{ss}}(t_{\mathrm{s}},t') = \int_{-\infty}^{\infty} \mathrm{d}t' G_{\mathrm{ii}}(t_{\mathrm{i}},t')G_{\mathrm{si}}(t_{\mathrm{s}},t'), \tag{3.26}$$

where the two different forms are due to the constraint in Eq. (3.16). Using the first form of Eq. (3.26) together with Eqs. (3.20), and (3.24), allows an explicit expression for the JTA, and a central result of this chapter, to be obtained

$$\begin{aligned}\mathcal{A}(t_{\mathrm{i}},t_{\mathrm{s}}) = {}& i\epsilon\bar{\gamma}(z_c,t_c)\mathrm{H}(t_{\mathrm{s}}-t_{\mathrm{i}}+\beta_{\mathrm{is}}l)\mathrm{H}(t_{\mathrm{i}}-t_{\mathrm{s}})\\ &\times\exp\left\{i\left[\phi_{\mathrm{p}}(z_c,t_c)+\phi_{\mathrm{q}}(z_c,t_c)+\phi_{\mathrm{i}}^{(r)}(l,t_{\mathrm{i}})+\phi_{\mathrm{s}}^{(r)}(l,t_{\mathrm{s}})\right]\right\},\end{aligned} \tag{3.27}$$

in which $\phi_{\mathrm{s}}^{(r)}$ has the same form as Eq. (3.23) with $\mathrm{i}\to\mathrm{s}$.

The form of the JTA in Eq. (3.27) is quite intuitive: First, the pre-factor $\epsilon\bar{\gamma}(z_c,t_c)$ describes the interaction strength which depends on the overlap of the two pump pulses in time and space. Next, the four phase terms describe, respectively, the NPM induced phases on the two pumps up until the creation event ($\phi_{\mathrm{p,q}}$), and the residual XPM-induced phases experienced by the idler and the signal after the creation event ($\phi_{\mathrm{i,s}}^{(r)}$). Finally, the two Heaviside functions have acquired new arguments as the collision coordinates, in terms of the signal and idler output times t_{s} and t_{i}, are now given by

$$z_c = l - \frac{t_{\mathrm{i}}-t_{\mathrm{s}}}{\beta_{\mathrm{is}}}, \quad t_c = \frac{\beta_{\mathrm{i}}t_{\mathrm{s}}-\beta_{\mathrm{s}}t_{\mathrm{i}}}{\beta_{\mathrm{is}}}. \tag{3.28}$$

It is clear upon inspection of these arguments, that the first Heaviside function corresponds to the waveguide input (unlike times), whereas the second corresponds to the waveguide output (like times).

3.3.5 The Schmidt decomposition

Additional insight on the relationship between the Green functions and the JTA can be obtained by considering their Schmidt decompositions. The four Green functions have the (related) Schmidt decompositions [82, 83]

$$G_{\mathrm{ii}}(t,t') = \sum_{j=1}^{\infty} v_{\mathrm{i}j}(t)\mu_j u_{\mathrm{i}j}^*(t'), \tag{3.29a}$$

$$G_{\mathrm{is}}(t,t') = \sum_{j=1}^{\infty} v_{\mathrm{i}j}(t)\nu_j u_{\mathrm{s}j}(t'), \tag{3.29b}$$

$$G_{\mathrm{si}}(t,t') = \sum_{j=1}^{\infty} v_{\mathrm{s}j}(t)\nu_j u_{\mathrm{i}j}(t'), \tag{3.29c}$$

$$G_{\mathrm{ss}}(t,t') = \sum_{j=1}^{\infty} v_{\mathrm{s}j}(t)\mu_j u_{\mathrm{s}j}^*(t'), \tag{3.29d}$$

for which each pair of the (real) Schmidt coefficients μ_j and ν_j obey the auxiliary equation $\mu_j^2 - \nu_j^2 = 1$ [83], and the output (v_{kj}) and input (u_{kj}) Schmidt modes for $k \in \{\mathrm{i},\mathrm{s}\}$ constitute four orthonormal sets. These decomposed forms of the Green functions allow us to gain additional insight regarding the JTA. Inserting the Schmidt decompositions of Eq. (3.29) into Eq. (3.26), the JTA may be formulated by its own Schmidt decomposition (see also Chapter 2)

$$\mathcal{A}(t_{\mathrm{i}},t_{\mathrm{s}}) = \sum_{j=1}^{\infty} \lambda_j v_{\mathrm{i}j}(t_{\mathrm{i}}) v_{\mathrm{s}j}(t_{\mathrm{s}}), \tag{3.30}$$

in which $\lambda_j = \mu_j\nu_j$ are the resulting Schmidt coefficients. In the regime of low pair-generation rate, $\nu_j \ll 1$, $\mu_j \approx 1$, and hence $\lambda_j \approx \nu_j$. The basis functions of the JTA are seen to be the output Schmidt modes $v_{\mathrm{i}j}$ and $v_{\mathrm{s}j}$ of the Green functions. This also explains the reason for the pairing of G_{ii} with G_{si} and G_{ss} with G_{is} in Eq. (3.26). It is noteworthy that the separability of G_{is} and G_{si} is both a necessary and sufficient condition for achieving a separable JTA. This implies, that one, in principle, only needs to determine G_{is} or G_{si} to establish the separability of the JTA. If necessary the Green functions may also be found numerically by employing the method from [84, 85, 86].

The Schmidt decomposition is an invaluable tool for characterizing photon-pair sources, and it simplifies the calculation of some important quantities such as the photon-pair generation probability (or rate per set of pump pulses)

$$\begin{aligned} R &= \iint \mathrm{d}t_{\mathrm{s}}\mathrm{d}t_{\mathrm{i}} |\mathcal{A}(t_{\mathrm{i}},t_{\mathrm{s}})|^2 \\ &= \sum_{j=1}^{\infty} \lambda_j^2. \end{aligned} \tag{3.31}$$

From this follows that λ_j^2 should be interpreted as the generation probability of a signal-idler photon pair with respective temporal wave-packet profiles $v_{\mathrm{s}j}$ and $v_{\mathrm{i}j}$. Similarly, for the quantum-mechanical purity of a heralded single photon[3]

$$\begin{aligned}\mathcal{P} &= \frac{1}{R^2}\iiiint \mathrm{d}t_\mathrm{s}\mathrm{d}t_\mathrm{i}\mathrm{d}t_\mathrm{s}'\mathrm{d}t_\mathrm{i}'\ \mathcal{A}(t_\mathrm{i},t_\mathrm{s})\mathcal{A}^*(t_\mathrm{i}',t_\mathrm{s})\mathcal{A}^*(t_\mathrm{i},t_\mathrm{s}')\mathcal{A}(t_\mathrm{i}',t_\mathrm{s}') \\ &= \frac{1}{R^2}\sum_{j=1}^{\infty}\lambda_j^4 \leq 1,\end{aligned} \tag{3.32}$$

for which the ideal case of unity corresponds to no temporal entanglement between the signal and idler photons. This situation is obtained, only if the JTA can be expressed as a product of a single set of temporal wave-packet modes, i.e. $\mathcal{A}(t_\mathrm{i},t_\mathrm{s}) = \lambda_1 v_{\mathrm{i}1}(t_\mathrm{i})v_{\mathrm{s}1}(t_\mathrm{s})$.

3.4 Type-II four-wave mixing for pure heralded photons

3.4.1 Initial examples

We now specifically consider the type-II FWM process, described in Sec. 3.2. To simplify our analysis, we initially assume that the two pump pulses have common Gaussian temporal profiles given by

$$A_j(0,t) = \left(\frac{\bar{E}_j}{\pi^{1/2}\tau}\right)^{1/2}\exp\left(-\frac{(t+t_{0j})^2}{2\tau^2}\right), \tag{3.33}$$

where $\bar{E}_j$ is the pulse energy, τ is the temporal pulse width, and t_{0j} is an initial pump-dependent time delay. Postponing our investigation of the effect of NPM to Sec. 3.4.5, the JTA from Eq. (3.27) now takes the explicit form

$$\begin{aligned}\mathcal{A}(\tau_\mathrm{i},\tau_\mathrm{s}) =& \frac{i\epsilon\gamma(\bar{E}_\mathrm{p}\bar{E}_\mathrm{q})^{1/2}}{\pi\tau^2\beta_\mathrm{is}}\ \exp\left[-\left(\frac{\beta_\mathrm{ps}\tau_\mathrm{i}-\beta_\mathrm{pi}\tau_\mathrm{s}}{\beta_\mathrm{is}}-\frac{\beta_\mathrm{p}l}{\tau}+\frac{t_{0\mathrm{p}}}{\tau}\right)^2/2\right] \\ &\times\exp\left[-\left(\frac{\beta_\mathrm{qs}\tau_\mathrm{i}-\beta_\mathrm{qi}\tau_\mathrm{s}}{\beta_\mathrm{is}}-\frac{\beta_\mathrm{q}l}{\tau}+\frac{t_{0\mathrm{q}}}{\tau}\right)^2/2\right]\mathrm{H}(\tau_\mathrm{s}-\tau_\mathrm{i}+\zeta)\mathrm{H}(\tau_\mathrm{i}-\tau_\mathrm{s}),\end{aligned} \tag{3.34}$$

where we have defined the normalized times $\tau_{\mathrm{i,s}} = t_{\mathrm{i,s}}/\tau$ and the normalized walk-off parameter $\zeta = \beta_\mathrm{is}l/\tau$. With the phase-matching property of the type-II FWM process, the fields are approximately group-velocity matched in pairs (see Sec. 3.2).

[3]Note the difference between Eq. (3.32) and Eq. (2.41) in that we here do not consider a normalized two-photon state. In calculating the spectral purity, this is made up for with a normalization constant, which turns out to be R^{-2}.

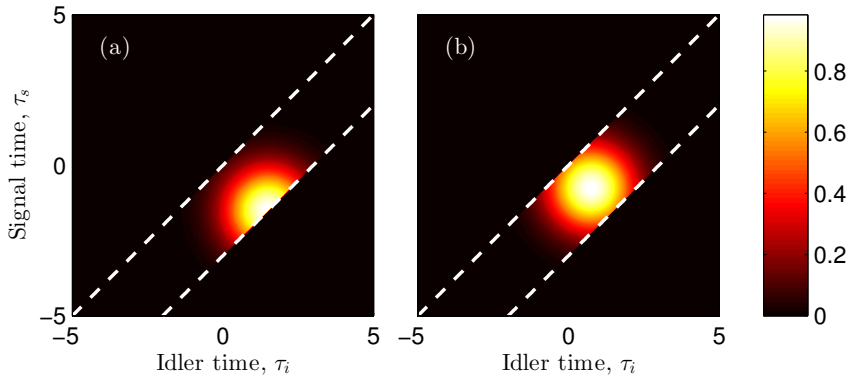

Figure 3.2: Normalized absolute value of the JTA for $\zeta = 3$ in cases of (a) the two pump pulses being perfectly overlapped at the waveguide beginning, and (b) the two pump pulses being perfectly overlapped at the center of the waveguide.

With this in mind, we may, for the time being, choose to set $\beta_{\mathrm{pi}} = \beta_{\mathrm{qs}} = 0$, which also considerably simplifies Eq. (3.34). For this parameter choice, Fig. 3.2 shows the absolute value of the (normalized) JTA for a moderate walk-off level of $\zeta = 3$, in cases where (a) the pumps are overlapped initially ($t_{0\mathrm{p}} = t_{0\mathrm{q}} = 0$), and (b) where the pumps are perfectly overlapped half way through the waveguide ($t_{0\mathrm{p}} = \beta_{\mathrm{p}} l/2$ and $t_{0\mathrm{q}} = \beta_{\mathrm{q}} l/2$). In both cases, the white dashed lines indicate the boundaries of the causality region mathematically described by the Heaviside step functions. In case (a), the interaction is abruptly turned on at the beginning of the waveguide and almost absent at the output, which focuses the JTA to the lower line of causality where the output temporal separation between signal- and idler photons is maximal. That is, for photon pairs generated at the waveguide beginning, an output idler photon is seen to trail the signal photon by $\tau_{\mathrm{i}} - \tau_{\mathrm{s}} = \zeta$. The abrupt interaction turn-on is seen to result in a rather strongly correlated JTA. This correlation turns out to be somewhat mitigated if we instead consider case (b), where the pumps are delayed with respective to each other such that their overlap is largest at the waveguide midpoint. The interaction is gradually increasing, and subsequently decreasing, as the fast pump pulse (in our case pump q) overtakes the slow pump pulse (in our case pump p). Such a gradually varying interaction strongly limits the influence of the waveguide endpoints, which could be made completely insignificant had we used a slightly longer waveguide.

3.4.2 Dependence on waveguide length

Inspired by the results from the previous section, Fig. 3.3 shows the purity $\mathcal{P}$, calculated from Eq. (3.32), as a function of the normalized walk-off parameter ζ in the same two cases considered in Fig. 3.2. In the case where the pulses are initially overlapped, the purity quickly saturates at a value slightly below 0.7.

Increasing the waveguide length (or decreasing the pulse width) beyond $\zeta > 3$ [see Fig. 3.2(a)] does not have any significant effect as $\zeta = 3$ already ensures that the two pump pulses do not overlap at the waveguide endpoint. In contrast, the case where the pumps are overlapped at the waveguide midpoint the purity asymptotically approaches unity as ζ is increased. Now, however, the pumps have to walk completely through each other to ensure no significant pump-pulse overlap at any of the endpoints. This is seen to be achieved for $\zeta \approx 6$ where the purity has reached a value of $\mathcal{P} \approx 0.995$.

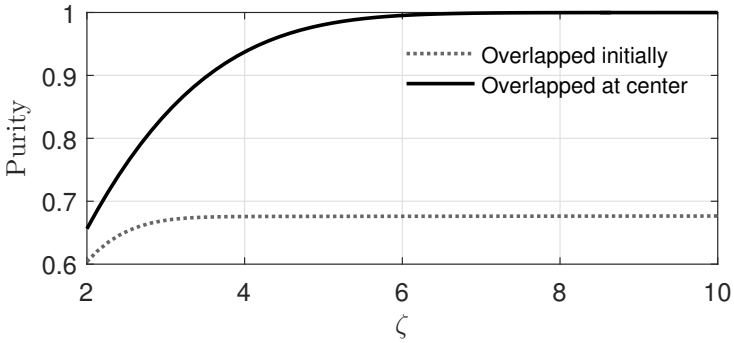

Figure 3.3: The purity as a function of the dimensionless distance parameter ζ in the two cases where the pumps are either overlapped at the begining or the center of the waveguide.

3.4.3 Purity considerations

Lets now consider, in more detail, the situation where the two pumps walk completely through such that we may neglect the Heaviside step functions. In this case, Eq. (3.31) becomes a double integral of a two-dimensional Gaussian function, which may be performed analytically. For pumps of the form given in Eq. (3.33), but generalized to potentially different temporal pulse widths of τ_{p} and τ_{q}, we find

$$R_f = \frac{\epsilon^2 \gamma^2 \bar{E}_{\mathrm{p}} \bar{E}_{\mathrm{q}}}{|\beta_{\mathrm{is}} \beta_{\mathrm{pq}}|}, \tag{3.35}$$

in which the subscript f refers to a full collision. The pair-production rate, R_f, depends on the pulse energies but is independent of the waveguide length l. Instead, the important length scale is the effective interaction distance, which is determined by the inter-pulse walk-off between the two pumps [68].

When neglecting the Heaviside step functions, we may also carry out the quadruple integral in Eq. (3.32). After a few algebraic simplifications it can be

shown to take the form

$$\mathcal{P}_f = \frac{\sigma_{\mathrm{p,q}}|\beta_{\mathrm{ip}}\beta_{\mathrm{sq}} - \beta_{\mathrm{iq}}\beta_{\mathrm{sp}}|}{\sqrt{\left(\beta_{\mathrm{ip}}^2 + \beta_{\mathrm{iq}}^2\sigma_{\mathrm{p,q}}^2\right)\left(\beta_{\mathrm{sp}}^2 + \beta_{\mathrm{sq}}^2\sigma_{\mathrm{p,q}}^2\right)}}, \tag{3.36}$$

where we have defined the fractional pump width $\sigma_{\mathrm{p,q}} = \tau_{\mathrm{p}}/\tau_{\mathrm{q}}$. Equation (3.36), though it excludes NPM effects, directly leads to a key criterion for achieving unit purity. This criterion states that the relative group slownesses and fractional pump width should satisfy

$$\beta_{\mathrm{ip}}\beta_{\mathrm{sp}} = -\sigma_{\mathrm{p,q}}^2\beta_{\mathrm{iq}}\beta_{\mathrm{sq}}, \tag{3.37}$$

This criterion, which was also found in a more complicated form in [68], turns out to be satisfied almost by default when using the type-II cross-polarized form of SFWM considered here. To see this, recall that the fields are phase-matched so that they are approximately pairwise group-slowness matched, $\beta_{\mathrm{s}}^{(1)} \approx \beta_{\mathrm{q}}^{(1)}$ and $\beta_{\mathrm{i}}^{(1)} \approx \beta_{\mathrm{p}}^{(1)}$. This inverse group-velocity matching is readily seen to make both the left- and right-hand sides vanish in Eq. (3.37). Alternatively, if the fields are not exactly group-velocity matched, Eq. (3.37) is seen to have solutions for either $\beta_{\mathrm{p}} > \beta_{\mathrm{i}} > \beta_{\mathrm{q}} > \beta_{\mathrm{s}}$ or $\beta_{\mathrm{i}} > \beta_{\mathrm{p}} > \beta_{\mathrm{s}} > \beta_{\mathrm{q}}$, while using the fractional pump width as a tuning parameter. Remarkably, this relationship between the inverse group velocities is exactly the tendency observed for type-II FWM [see Fig. 3.1(b)], when a polarization-mode dependent GVD is taken into account.

To investigate the effect of non-group velocity matched fields, Fig. 3.4 shows the attainable purity as a function of the ratio $\delta\beta_1/\Delta\beta_1$ where $\delta\beta_1 = \beta_{\mathrm{pi}} = \beta_{\mathrm{qs}}$ and $\Delta\beta_1 = \beta_{\mathrm{pq}}$. Without tuning the fractional pulse width $\sigma_{\mathrm{p,q}}$ (solid line) the purity falls of slightly for $\delta\beta_1/\Delta\beta_1 > 0.2$, which by virtue of Eq. (3.6) corresponds to a relatively large difference in group-velocity dispersion of $\Delta\beta_2/\beta_{2,\mathrm{av}} > 0.4$. However, even in cases where the group-velocity dispersion is strongly polarization-mode dependent, the purity can be restored to unity by appropriately tuning $\sigma_{\mathrm{p,q}}$ (dashed-dotted line).

3.4.4 Shaping the signal-idler wavepackets

The purity criterion in Eq. (3.37) was derived under the assumption of having two Gaussian pumps that undergo a full collision inside the waveguide. However, it turns out that the use of Gaussian pumps are not a necessary requirement for achieving a temporally uncorrelated JTA. To see this, recall the general expression for the JTA in Eq. (3.27), which, in the absence of NPM and the boundary effects, takes the very simply form $\mathcal{A}(t_{\mathrm{i}}, t_{\mathrm{s}}) = i\epsilon\gamma A_{\mathrm{p}}(t_c - \beta_{\mathrm{p}}z_c)A_{\mathrm{q}}(t_c - \beta_{\mathrm{q}}z_c)/\beta_{\mathrm{is}}$. If we now, again, consider the case where the fields are pairwise group-slowness matched, such that $\beta_{\mathrm{ip}} = \beta_{\mathrm{sq}} = 0$, we find, using the expression for the collision coordinates in

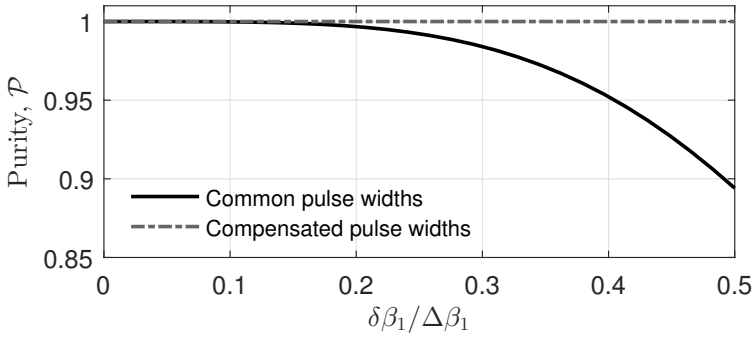

Figure 3.4: The purity obtained as a function of $|\delta\beta_1/\Delta\beta_1| = |\Delta\beta_2/(2\beta_{2,\mathrm{av}})|$, with and without compensation using different relative pump pulse widths τ_p and τ_q. A full collision between the pumps were assumed.

Eq. (3.28), that the pump arguments simplify:

$$t_c - \beta_\mathrm{i} z_c = t_\mathrm{i} - \beta_\mathrm{i} l, \tag{3.38a}$$

$$t_c - \beta_\mathrm{s} z_c = t_\mathrm{s} - \beta_\mathrm{s} l, \tag{3.38b}$$

which entails that $\mathcal{A}(t_\mathrm{i}, t_\mathrm{s}) = i\epsilon\gamma A_\mathrm{p}(t_\mathrm{i} - \beta_\mathrm{i} l) A_\mathrm{q}(t_\mathrm{s} - \beta_\mathrm{s} l)/\beta_\mathrm{is}$. On this form the JTA is strictly separable entirely independent of the chosen pump profiles. Moreover, the simplification shows that the generated idler wavepacket becomes a temporal copy of pump p while the signal wavepacket is an image of pump q. This entails that one may simultaneously (and independently) shape the signal-idler wavepackets 'simply' by tailoring the two pump profiles. To illustrate this capability, Fig. 3.5(a) shows the normalized JTA for unequal pump widths satisfying $\tau_\mathrm{p} = 3\tau_\mathrm{q}$, and $\zeta = \beta_\mathrm{is} l/\tau_\mathrm{p} = 8$. As pump p is three times broader than pump q, the JTA becomes elongated, but retains the property of being separable. Moreover, Fig. 3.5(b) shows the first-order signal- and idler Schmidt modes, clearly demonstrating that the resulting idler (which co-propagates with pump p) is broader than the signal (which co-propagates with the narrow pump q).

To underline that our scheme also works for non-Gaussian pump profiles, Fig. 3.6(a) shows the JTA, and Fig. 3.6(b) the corresponding first-order Schmidt modes, for a first-order Hermite-Gaussian pump p [while pump q is still a normal Gaussian of the form in Eq. (3.33)]. We describe this mathematically as an input envelope of the form

$$A_p^{(\mathrm{HG}_1)}(0,t) = \left(\frac{2\bar{E}_\mathrm{p}}{\pi^{1/2}\tau_\mathrm{p}}\right)^{1/2} \left(\frac{t + t_{0\mathrm{p}}}{\tau_\mathrm{p}}\right) \exp\left(-\frac{(t + t_{0j})^2}{2\tau_\mathrm{p}^2}\right). \tag{3.39}$$

Figure 3.6 was obtained using $\tau_\mathrm{p} = \tau_\mathrm{q}$ and $\zeta = 8$, corresponding to a complete collision between the pump pulses as indicated with the dashed white lines. Notably,

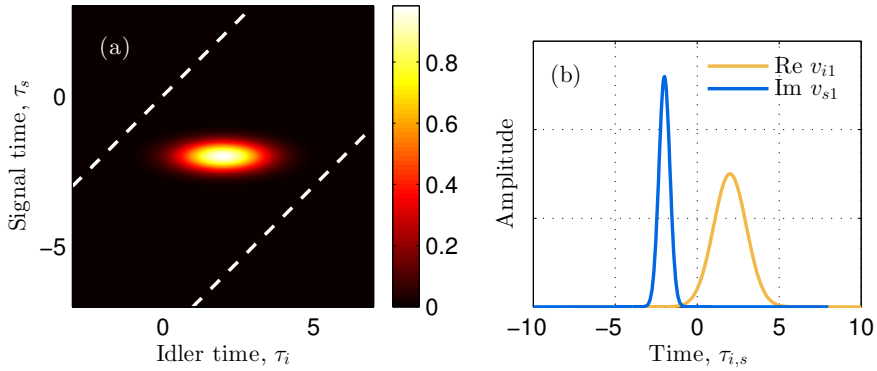

Figure 3.5: (a) Absolute value of the normalized JTA for two Gaussian pumps but with $\tau_\mathrm{q} = \tau_\mathrm{p}/3$ and $\zeta = \beta_\mathrm{is} l/\tau_\mathrm{p} = 8$. (b) The corresponding first-order signal-idler Schmidt modes.

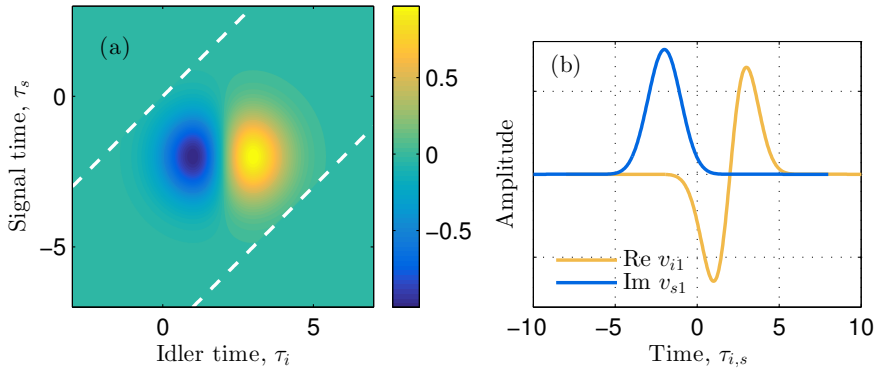

Figure 3.6: (a) Imaginary value of the normalized JTA for $\zeta = \beta_\mathrm{is} l/\tau_\mathrm{p,q} = 8$ in the case where pump q is Gaussian shaped and pump p is a first-order Hermite Gaussian. (b) The corresponding first-order signal-idler Schmidt modes.

while signal Schmidt mode is still Gaussian shaped, the idler Schmidt mode inherits not only the shape of pump p, but also the phase profile. Moreover, despite of the complicated structure of the JTA, it remains entirely separable.

We note that the kind of biphoton shaping considered here is also possible in specifically tailored parametric downconversion sources, albeit in that case only one of the photons (the signal or the idler) becomes a copy of the pump, while the other becomes temporally elongated [87, 88]. Our scheme does not have this limitation.

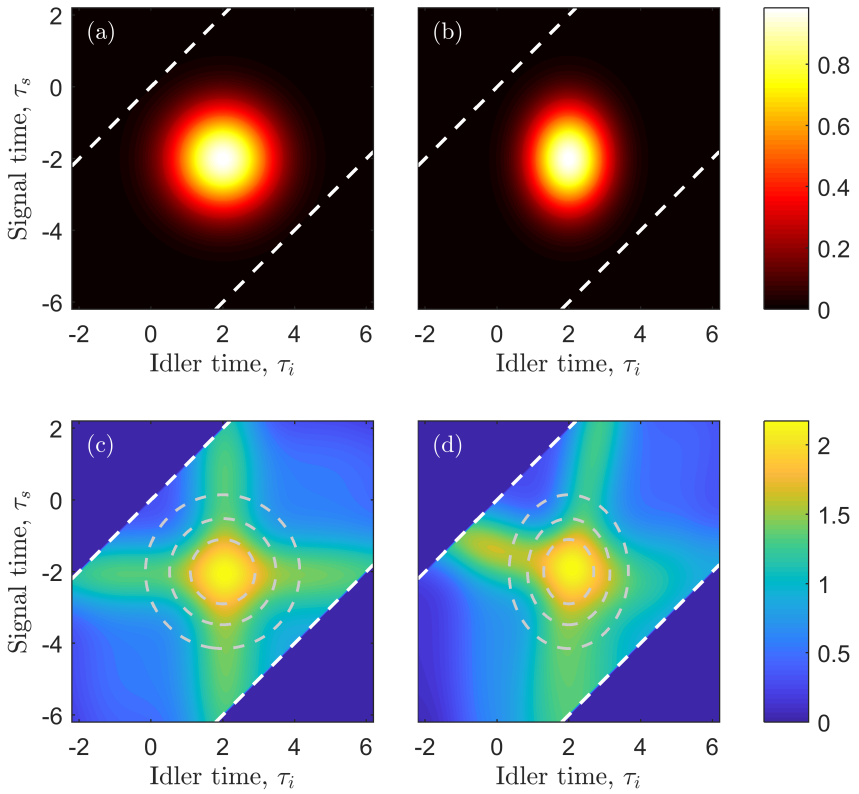

Figure 3.7: Normalized absolute value (a) and (b), and phase (c) and (d) of the JTA obtained for two different relative group-velocity mismatches. In (a), (c) the fields are pairwise group-velocity matched, while in (b), (d) the fields are group-velocity mismatched so that $\delta\beta_1/\Delta\beta_1 = 0.25$ with the pulse widths chosen so as to comply with the purity criterion in Eq. (3.37). The boarding white dashed lines enclose the causal region of the step functions, and the grey dashed lines in (c) and (d) are amplitude contours of the corresponding JTAs in (a) and (b). Simulation parameters: $\zeta = 8$ and $R = 0.02$.

3.4.5 Effect of nonlinear phase modulation

We now consider the effect of NPM on the correlation of the signal-idler biphoton state, and first assume an amorphous material for which $\epsilon = \epsilon_{\rm pq} = \epsilon_{\rm sq} = \epsilon_{\rm ip} = 2/3$ and $\epsilon_{\rm sp} = \epsilon_{\rm iq} = 2$.

Figure 3.7 illustrates amplitude and phase of the JTA in two cases of Gaussian pumps that undergo a complete collision. In the left column, subfigures (a) and (c), the fields are pairwise group-velocity matched ($\beta_{\rm ip} = \beta_{\rm sq} = 0$), while in the right column, subfigures (b) and (d), the fields are strongly group-velocity mismatched with $\delta\beta_1/\Delta\beta_1 = 0.25$. In the group-velocity mismatched case $\tau_{\rm q}$ has been compensated according to Eq. (3.37) to make the absolute value of the JTA

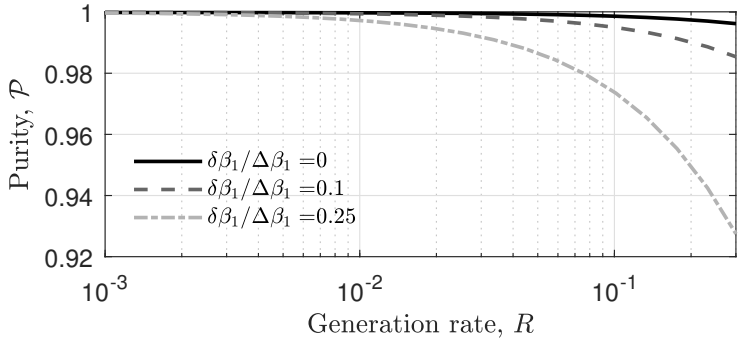

Figure 3.8: The effect of NPM on purity versus generation rate for different normalized group-slowness mismatches and a normalized distance parameter $\zeta = 8$. As indicated in Fig. 3.7, the case where the fields are perfectly group-slowness matched in pairs (solid line) proves to be very resistant to the effect of NPM.

separable. As we have previously discussed the JTA amplitudes in detail (these are unaffected by NPM), we here focus on the JTA phases in Fig. 3.7(c) and (d). Considering first the group-velocity matched case, the JTA exhibits four phase branches, which, in clockwise order, are due to: XPM from pump q to the signal (3 o'clock), XPM from pump p to the idler (6 o'clock), SPM of pump q (9 o'clock), and SPM of pump p (12 o'clock). The fact that the fields are perfectly group-velocity matched in pairs is manifested by these phase branches being horizontally and vertically oriented. The main feature, however, is a Bell-like peak which coincides with the JTA amplitude, and will result in the signal-idler Schmidt modes having a quadratic chirp. In the group-velocity mismatched case, in Fig. 3.7(d), the four phase branches are neither horizontal or vertical and therefore give rise to temporal phase correlations. Such correlations are not (visibly) apparent for the group-velocity matched case in Fig. 3.7(c), which is due to the large degree of symmetry[4].

As NPM is a nonlinear effect, we expect its influence to be dependent on the interaction strength, and therefore on the generation rate R. Figure 3.8 shows the purity, $\mathcal{P}$, as a function of the generation rate R (recall that this is really a probability) in the case where both pumps are Gaussians of width τ, and the normalized distance parameter $\zeta = 8$ ensuring a full pump-pump collision. The purity is displayed for three different values of the normalized group-slowness mismatch $\delta\beta_1/\Delta\beta_1$ [see Fig. 3.4], and in general the effect of NPM is seen to increase for larger values of $\delta\beta_1/\Delta\beta_1$. Notably, the case of perfectly group-slowness matched fields ($\delta\beta_1/\Delta\beta_1 = 0$) shows the largest degree of robustness against the effect NPM and only undergoes a small decrease in purity for large generation rates on the

[4]One should be aware of the fact that the linearity of the exponential function plays an important role here: Notably, $h_1(x, y) = \exp[f(x)+g(y)]$ is separable, while $h_2(x, y) = f(x)+g(y)$ is not.

order of $R \sim 0.1$ — a regime in which the validity of the presented perturbative results should be questioned [40, 86].

Remarkably, Fig. 3.7(c) and Fig. 3.8 both illustrate how the case with $\beta_{\mathrm{ip}} = \beta_{\mathrm{sq}} = 0$ is almost completely unaffected by NPM. To see why this is, we now take a detailed look at the phase terms in Eq. (3.27). Calculating each phase term separately, while again considering $\epsilon = \epsilon_{\mathrm{pq}} = \epsilon_{\mathrm{sq}} = \epsilon_{\mathrm{ip}}$ as a variable, and utilizing that $\beta_{\mathrm{ip}} = \beta_{\mathrm{sq}} = 0$, we find

$$\phi_{\mathrm{p}}(z_c, t_c) = \gamma |A_{\mathrm{p}}(t_{\mathrm{i}} - \beta_{\mathrm{i}} l)|^2 z_c + \frac{\epsilon\gamma}{\beta_{\mathrm{is}}} \int_{t_{\mathrm{i}} - \beta_{\mathrm{i}} l}^{t_{\mathrm{s}} - \beta_{\mathrm{s}} l} \mathrm{d}\tau \; |A_{\mathrm{q}}(\tau)|^2, \tag{3.40}$$

and

$$\phi_{\mathrm{q}}(z_c, t_c) = \gamma |A_{\mathrm{q}}(t_{\mathrm{s}} - \beta_{\mathrm{s}} l)|^2 z_c + \frac{\epsilon\gamma}{\beta_{\mathrm{is}}} \int_{t_i - \beta_{\mathrm{i}} l}^{t_s - \beta_{\mathrm{s}} l} \mathrm{d}\tau \; |A_{\mathrm{p}}(\tau)|^2, \tag{3.41}$$

for the pump terms, and

$$\phi_{\mathrm{i}}^{(r)}(l, t_{\mathrm{i}}) = \epsilon\gamma |A_{\mathrm{p}}(t_{\mathrm{i}} - \beta_{\mathrm{i}} l)|^2 (l - z_c) + \frac{2\gamma}{\beta_{\mathrm{is}}} \int_{t_{\mathrm{s}} - \beta_{\mathrm{s}} l}^{t_{\mathrm{i}} - \beta_{\mathrm{s}} l} \mathrm{d}\tau \; |A_{\mathrm{q}}(\tau)|^2, \tag{3.42}$$

and

$$\phi_{\mathrm{s}}^{(r)}(l, t_{\mathrm{s}}) = \epsilon\gamma |A_{\mathrm{q}}(t_{\mathrm{s}} - \beta_{\mathrm{s}} l)|^2 (l - z_c) + \frac{2\gamma}{\beta_{\mathrm{si}}} \int_{t_{\mathrm{i}} - \beta_{\mathrm{i}} l}^{t_{\mathrm{s}} - \beta_{\mathrm{i}} l} \mathrm{d}\tau \; |A_{\mathrm{p}}(\tau)|^2, \tag{3.43}$$

for the residual XPM-induced phase terms. Apparently, in the pairwise group-velocity matched case, the four integrals are separable phase terms (i.e. frequency shifts and chirps), which do not contribute to temporal phase correlations. After computing the JTA phase: $\Phi_{\mathrm{JTA}}(t_{\mathrm{i}}, t_{\mathrm{s}}) = \phi_{\mathrm{p}}(z_c, t_c) + \phi_{\mathrm{q}}(z_c, t_c) + \phi_{\mathrm{i}}^{(r)}(l, t_{\mathrm{i}}) + \phi_{\mathrm{s}}^{(r)}(l, t_{\mathrm{s}})$, we can identify the contribution to a non-separable phase, Φ_{NS}:

$$\Phi_{\mathrm{NS}}(t_{\mathrm{i}}, t_{\mathrm{s}}) = \frac{(1 - \epsilon)\,\gamma}{\beta_{\mathrm{is}}} \left[|A_{\mathrm{p}}(t_{\mathrm{i}} - \beta_{\mathrm{i}} l)|^2 t_{\mathrm{s}} - |A_{\mathrm{q}}(t_{\mathrm{s}} - \beta_{\mathrm{s}} l)|^2 t_{\mathrm{i}} \right]. \tag{3.44}$$

Interestingly, due to the pre-factor of $(1-\epsilon)$, the different contributions to the non-separable phase appear to partly cancel each other out. Moreover, the cancellation effect is seen to be directly related to the nonlinear anisotropy of the third-order susceptibility tensor. While the correlations due to NPM is small for an isotropic media for which $\epsilon = 2/3$ [see Fig. 3.8], it would be even less significant in silicon waveguides ($\epsilon_{\mathrm{Si}} = 0.85$ [89]), and its impact completely vanish for a potential anisotropic material where $\epsilon = 1$.

3.5 Discussion and Summary

The proposed method for generating spectrally unentangled photon pairs relies on a birefringence-induced walk-off between two cross-polarized pump pulses to realize an interaction strength that varies along the waveguide. This means that the nonlinear interaction of the desired process takes place over an effective length scale that is shorter than the actual waveguide length. This stands in contrast to spurious noise processes such as spontaneous Raman scattering or intra-polarization modulation instability which (typically) occur individually for each polarization mode but over the entire waveguide. Moreover, compared to the same spurious processes, the desired process endures a penalty in interaction strength as it involves fields of orthogonal polarizations where the nonlinear coupling is relatively lower.

To overcome the noise-related issue described above, there are different potential tracks. One possibility is a fiber-based solution, which, necessitates a very large frequency detuning $\delta\omega \gg 2\pi \times 13$ THz, and/or cryogenic cooling to mitigate spontaneous Raman scattering [90]. While this turns out to be difficult to accomplish using polarization modes (an early experiment using a polarization-maintaining (PM) fiber realized $\delta\omega \approx 2\pi \times 3$ THz in the telecommunications band [76]), an alternative solution incorporates higher-order modes for which the inter-modal group-slowness difference may be significantly larger, and recently detunings in excess of 20 THz have been demonstrated [71]. Another route involves the use of integrated waveguides, which, depending on the waveguide material, typically has a Raman spectrum that is relatively narrow. As an example, crystalline silicon has a very strong, but an ultra narrow, Raman gain peak at around 15.6 THz, which could easily be filtered out. Additionally, integrated waveguides offer the potential of tailoring the degree of birefringence simply by appropriately designing the waveguide cross-section. We take a closer look at this opportunity in Chapter 6.

In conclusion, we have presented a configuration for the generation of temporally (and spectrally) uncorrelated photon pairs using SFWM. Our method relies on the type-II FWM interaction, which in a birefringent waveguide naturally generates orthogonally polarized signal- and idler sidebands that are (approximately) pairwise group-velocity matched to the orthogonally polarized pump. This, in combination with a gradually varying interaction strength enabled by birefringence-induced pump-pump walk-off, is the exact recipe for completely eliminating temporal-spectral biphoton correlations. We further show that the process facilitates arbitrary shaping of the generated signal- and idler temporal wavepackets, enabled simply by tailoring the temporal form of the two pump pulses. Finally, our time-domain approach allows us to demonstrate that the inclusion of NPM in the considered configuration hardly introduces any temporal phase correlations (in strong contrast to, especially, the asymmetric configuration [64]). Including the recent findings that the configuration displays strong robustness against the effects of group-velocity dispersion [65], and may be tailored to mitigate longitudinal dispersion fluctuations [69], we believe that the proposed scheme holds great

promise for forming future sources of tailored biphotons and pure-state heralded single photons.

CHAPTER 4

Tailored photon-pair generation in a microring resonator

Microring resonators have become an established workhorse for nonlinear optics. This chapter, which is an extended and modified version of work in [91, 92], contains a new proposal on how a tailored pump pulse can be used to eliminate spectral correlation in photon pairs generated from nonlinear microring resonators.

4.1 Introduction

During the last decade, microring resonators (MRRs) have become an established tool within the field of integrated quantum photonics [93, 94, 95, 96]. In particular, focus has been dedicated to using MRRs, or similar resonantly based structures, for generating quantum-correlated photon pairs through SFWM [97, 98, 99, 100]. This approach provides a number of advantages compared to the use of straight waveguides: (1) The MRR comes with a potentially extremely small integrated footprint; (2) The combination of strongly nonlinear materials and the resonantly enhanced fields strongly reduces the energy budget per source; (3) The semi-discrete MRR resonance spectrum provides a natural basis for the spectral modes of the pump (p), signal (s), and idler (i) fields, and; (4) provides a means for generating so-called biphoton frequency combs for which the signal-idler biphoton state is coherently distributed over multiple spectral resonances (see Fig. 4.1). The final point opens up the possibility for generation of high-dimensional quantum states in the frequency basis [101], and recently multiple groups have demonstrated on-chip generation and off-chip processing of such quantum states [102, 103].

As for photon pairs generated in straight waveguides (see Chapter 2 and Chapter 3), a photon pair generated in an MRR may exhibit either strong or weak

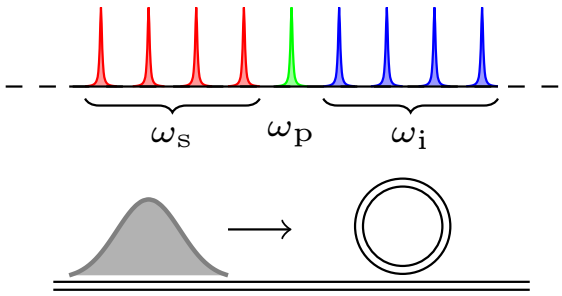

Figure 4.1: Sketch and designation of resonances in an MRR source of quantum-correlated photon pairs.

spectral correlation. The degree of spectral correlation depends on the spectral width of the pump used for excitation relative to the bandwidth of the resonances [104]. In particular, if a Gaussian shaped pump pulse is used to excite a standard MRR, there exists a lower bound on the degree of spectral entanglement, reached when the pump is spectrally much broader than the excited resonance. In other words, the spectral purity of heralded photons generated from standard MRR sources is bounded to values below $\sim 92\%$ [104]. Notably, this limit has now been approached in experiments involving quantum intereference between heralded photons from different MRR sources [105], and reached in genuine measurements of the unheralded second-order correlation function [102][1]. Recently, however, it was suggested by Z. Vernon *et al.* that this limit could be overcome by altering the underlying MRR structure so that the signal and/or the idler resonances become spectrally narrow compared to the pump resonance [107]. This is achievable by interferometrically (multi-point) coupling the connecting bus waveguide to the MRR [108].

In this chapter, we propose an alternative means for completely eliminating the spectral entanglement in photon pairs generated from MRR sources. We start out, in Sec. 4.2, by providing the necessary theoretical framework for SFWM in an MRR. Following this, in Sec. 4.3 we demonstrate and analyse how a specifically tailored "dual-pump pulse" can be used to remove spectral correlation from photon pairs generated in a standard MRR structure. Finally, in Sec. 4.4 we discuss our results and conclude.

4.2 Theory

An MRR is characterized by a free-spectral range (FSR), ν_{FSR}. The FSR is the spacing between resonator modes that each satisfy the resonance criterion

[1]The unheralded second-order correlation function is related to the single-mode purity according to $g^{(2)} = 1 + \mathcal{P}$ [106].

$n_{\text{eff}}(\lambda)L = m\lambda$, where n_{eff} is the effective index of the considered waveguide mode, L is the length of the MRR, and m is an integer. The FSR is therefore given by

$$\nu_{\text{FSR}}(\lambda) = \frac{c}{n_{\text{eff}}(\lambda)L}, \tag{4.1}$$

and is typically well approximated by being constant over the range of tens of resonances. This entails, that by exciting a resonance, say $m = M$, with a pump (p), SFWM is energy- and wavenumber-matched for symmetrically surrounding resonances, i.e. $m = M \pm \{1, 2, 3, \ldots\}$, in which the generation of correlated photon pairs is resonantly enhanced by the redistributed optical density of states. While this process may take place in multiple resonance pairs simultaneously, we limit our treatment to considering only a single signal-idler resonance pair. Moreover, we consider the situation where the exciting pump light overlaps spectrally only with resonance $m = M$, so that the spectral width of the pump $\sigma_{\text{p}} \ll 2\pi\nu_{\text{FSR}}$. It is rather straightforward to show that this assumption is identical to the pump pulse duration τ_{p} being much longer than the resonator round-trip time[2].

4.2.1 Photon-pair generation in microring resonators

We consider the regime where the pump power is so low that only single pairs of signal and idler photons are probabilistically generated in the MRR. The biphoton-part of the output quantum state is, as in Chapter 2, expressed as

$$|\Psi_{\text{II}}\rangle = R^{-1/2} \iint \mathrm{d}\omega_{\text{i}}\mathrm{d}\omega_{\text{s}} \mathcal{A}(\omega_{\text{i}}, \omega_{\text{s}}) \hat{a}_{\text{i}}^{\dagger}(\omega_{\text{i}}) \hat{a}_{\text{s}}^{\dagger}(\omega_{\text{s}}) \, |\text{vac}\rangle \,, \tag{4.2}$$

wherein $\mathcal{A}(\omega_{\text{i}}, \omega_{\text{s}})$ is the bi-photon JSA, and $\hat{a}_j^{\dagger}(\omega_j)$ is a creation operator of a photon in mode $j \in \{\text{i}, \text{s}\}$, assumed to have no spectral overlap with adjacent resonances. To normalize Eq. (4.2), we have included the probability per pump pulse to generate a photon pair, $R = \iint \mathrm{d}\omega_{\text{i}}\mathrm{d}\omega_{\text{s}} |\mathcal{A}(\omega_{\text{i}}, \omega_{\text{s}})|^2$, which is restricted to $R \ll 1$, to avoid the output of multi-photon states.

In the context of resonator-based sources of photon pairs using SFWM, the JSA takes the form (omitting a proportionality factor unimportant for our analysis) [104, 107]

$$\mathcal{A}(\omega_{\text{i}}, \omega_{\text{s}}) \propto F_{\text{p}}(\omega_{\text{i}} + \omega_{\text{s}}) l_{\text{i}}(\omega_{\text{i}}) l_{\text{s}}(\omega_{\text{s}}), \tag{4.3}$$

in which F_{p} is given as the convolution

$$F_{\text{p}}(\omega) = \int \mathrm{d}\omega' \alpha_{\text{p}}(\omega - \omega') l_{\text{p}}(\omega - \omega') \alpha_{\text{p}}(\omega') l_{\text{p}}(\omega'), \tag{4.4}$$

and where the Lorentzian factor $l_j(\omega) = [\omega_{j0}/(2Q_j) + i\omega]^{-1}$ for the resonances $j \in \{\text{p}, \text{s}, \text{i}\}$. Here, ω_{j0} and Q_j are the center frequency and the quality factor of the jth resonance, respectively. Moreover, α_{p} is the spectral envelope of the pump

[2] To show this, one merely has to invert Eq. (4.1).

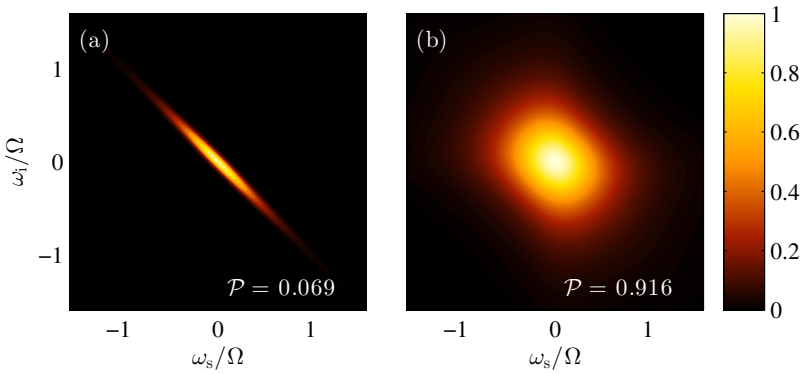

Figure 4.2: The normalized joint spectral intensity of a single signal-idler resonance pair for (a) a pump pulse that is spectrally narrower than the pumped resonance, and (b) a pump pulse that is spectrally broader than the pumped resonance. The resulting heralded-state spectral purities are given within each subfigure.

pulse prior to coupling into the MRR, and, as for the resonance linewidths l_j, the argument ω represents an angular frequency relative to ω_{j0}.

As seen from Eq. (4.3), the spectral correlation in the JSA is solely contained in $F_\mathrm{p}(\omega_\mathrm{i} + \omega_\mathrm{s})$. As a result, if F_p is made constant over the spectral widths of the signal and idler resonances, set by $l_{\mathrm{i,s}}$, then the JSA would be factorable. However, by virtue of Eq. (4.4), F_p is itself spectrally limited by its corresponding resonance shape l_p. For a Gaussian pump pulse, and a standard MRR structure where $Q_\mathrm{p} \approx Q_\mathrm{i} \approx Q_\mathrm{s}$, this turns out to impose an upper limit for the quantum-state purity of heralded photons of $\mathcal{P} \approx 0.92$. This is illustrated in Fig. 4.2, which shows the normalized JSI in cases where the Gaussian spectral width $\sigma_\mathrm{p} \ll \Omega_\mathrm{p} \equiv \omega_{\mathrm{p}0}/Q_\mathrm{p}$ (left) and $\sigma_\mathrm{p} \gg \Omega_\mathrm{p}$ (right), while keeping $\Omega = \Omega_\mathrm{p} = \Omega_\mathrm{s} = \Omega_\mathrm{i}$ to represent the situation for a standard MRR. Figure 4.2 thereby demonstrates that, even when the pump pulse is spectrally saturating the pump resonance, there is still spectral correlation in the signal-idler biphoton quantum state. A solution to this limitation was offered by Z. Vernon *et al.* [107], who suggested to use an MRR structure that is interferometrically coupled to the MRR, gaining individual control of the quality factors of the signal, idler, and pump resonances. In the following section, we pursue an alternative approach, which rather than altering the MRR structure itself, relies on tailoring the temporal-spectral profile of the incoming pump pulse.

4.3 Dual-pulse configuration

Descriptions of SFWM in MRRs have so far been partitioned into two categories when it comes to the pump light used for excitation: (1) continuous wave (CW)

operation, which enables ultra-low energy requirements, but the generated photon pairs are strongly spectrally correlated; and (2) pulsed operation, which has so far been limited to the study of Gaussian shaped or spectrally flat pump pulses. There is, however, no reason as to why a Gaussian shaped pump should be optimal, and it is therefore natural to look towards other pulse shapes that may perform better in terms of eliminating spectral correlations. To this end, consider again Eq. (4.4), which we wish to make frequency-independent over the range of the widths of l_i and l_s [such that $\mathcal{A}(\omega_\mathrm{i},\omega_\mathrm{s}) \propto l_\mathrm{i}(\omega_\mathrm{i}) l_\mathrm{s}(\omega_\mathrm{s})$]. A first approach to accomplish this, is to force the integrand in Eq. (4.4) to be constant by letting $\alpha_\mathrm{p}(\omega) = l_\mathrm{p}^{-1}(\omega)$. However, such a 'pulse' is quickly seen to be unphysical, and clearly makes the integral approach infinity. Instead, we therefore consider an incident pump pulse with a spectrum of the form

$$\alpha_\mathrm{p}^{(\mathrm{tar})}(\omega) = l_\mathrm{p}^{-1}(\omega) \exp\left(-\frac{\omega^2}{2\sigma^2}\right), \tag{4.5}$$

where the Gaussian factor bounds the pulse spectrum to have a finite width of σ. Insertion of Eq. (4.5) into Eq. (4.4), results in $F_\mathrm{p}(\omega) \propto \exp(-\omega^2/4\sigma^2)$, which in the limit $\sigma \gg \Omega_\mathrm{i,s}$, results in a factorable JSA. For this reason, we in the following refer to Eq. (4.5) as the 'target' pulse spectrum.

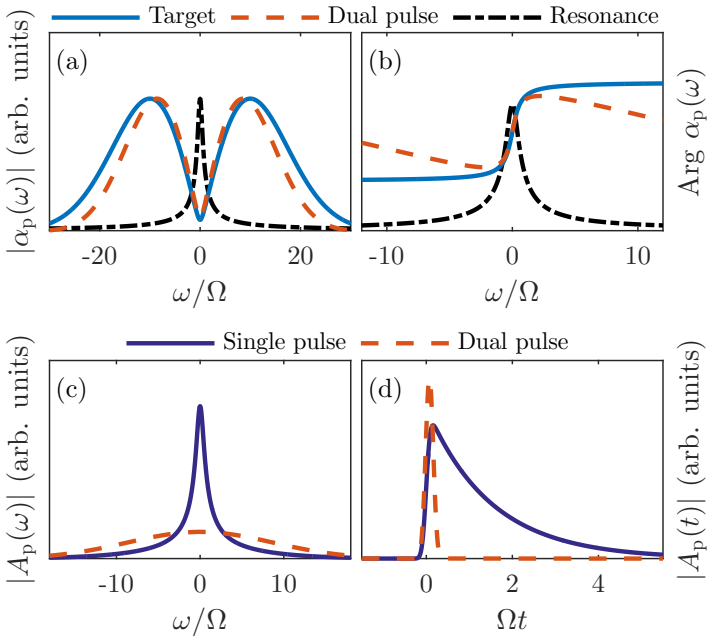

Figure 4.3: (a) Pulse spectrum $|\alpha_\mathrm{p}(\omega)|$, and (b) spectral phase, of the 'target' pulse and the dual-pulse configuration, both shown alongside the corresponding resonance spectrum $|l_\mathrm{p}(\omega)|$. (c) Spectral- and (d) temporal distribution of the in-resonator pump field for both single- and dual-pulse configurations. For parameters, see text.

On the form given in Eq. (4.5), the target pulse is difficult to interpret and visualize. To improve our understanding, we may inverse Fourier transform Eq. (4.5) to obtain the temporal profile

$$\alpha_{\mathrm{p}}^{(\mathrm{tar})}(t) \propto \left(\frac{t}{\tau^3} - \frac{\Omega_{\mathrm{p}}}{2\tau}\right) \exp\left(-\frac{t^2}{2\tau^2}\right), \tag{4.6}$$

where $\tau = 1/\sigma$. Equation (4.6) bears close resemblance to a first-order Hermite Gaussian, which is characterized by a node in the center surrounded by two Gaussian-like lobes which are π out phase. Therefore, to ease understanding, and parametrization, we instead consider a dual-pulse 'approximation' to the target pulse, which has the temporal form

$$\alpha_{\mathrm{p}}(t) = \left(\frac{\eta}{2\pi}\right)^{1/2} \exp\left(-\frac{t^2}{2\tau_{\mathrm{p}}}\right) - \left(\frac{1-\eta}{2\pi}\right)^{1/2} \exp\left[-\frac{(t-\Delta\tau)^2}{2\tau_{\mathrm{p}}}\right], \tag{4.7}$$

where the minus between the two terms gives the π-phase difference. The corresponding spectrum is

$$\alpha_{\mathrm{p}}(\omega) = \left[\eta^{1/2} - \exp(-i\Delta\tau\omega)\,(1-\eta)^{1/2}\right] \exp\left(-\frac{\tau_{\mathrm{p}}^2\omega^2}{2}\right). \tag{4.8}$$

In Eqs. (4.7) and (4.8), τ_{p} is the (common) pulse duration, $\Delta\tau$ is the inter-pulse temporal separation, and η is the relative weight of the two pulses.

To see that such a dual-pulse superposition provides an excellent qualitative approximation (for certain values of η, $\Delta\tau$, and τ_{p}) to the target pulse, Figs. 4.3(a) and (b) illustrate the close resemblance, in both absolute value and phase, obtained for the parameters $\eta = 0.55$, $\tau_{\mathrm{p}}\Omega = 0.1$, $\Delta\tau\Omega = 0.2$, and $\sigma\tau_p = 1$. The spectra are significantly broader than the corresponding resonance linewidth, and they both exhibit a spectral dip coinciding with the resonance. The effect of this is seen in Fig. 4.3(c) which shows the in-resonator pump field $A_{\mathrm{p}}(\omega) = \alpha_{\mathrm{p}}(\omega)l_{\mathrm{p}}(\omega)$ for the single-pulse case [$\eta = 1$ in (4.8)] and for the dual-pulse case parametrized as in Figs. 4.3(a) and (b) (here, both spectra are normalized with respect to their respective in-resonator pulse energies). Notably, the in-resonator field for the dual-pulse case is not, as in the single-pump case, spectrally limited by the spectral linewidth of the resonator. This broadening effect is perhaps intuitively easier to understand from a time-domain argument. As the delayed pulse encounters the coupling region between the bus waveguide and the MRR, it interferes with the part of the early pulse still inside the resonator. Due to the relative phase shift of π between the pulses, this interference is destructive into the resonator and constructive into the bus channel waveguide. Thus, rather than being limited by the resonator lifetime, pump light can be coupled in and subsequently out of the resonator on a time scale comparable to $\Delta\tau$. This is illustrated in Fig. 4.3(d) showing the stark contrast between an exponential decay and an interferometrically-induced outcoupling. The shorter lifetime effectively amounts to a smaller resonator quality factor for the pump resonance, and hence a broader pump spectrum inside the resonator, as was already shown in Fig. 4.3(c).

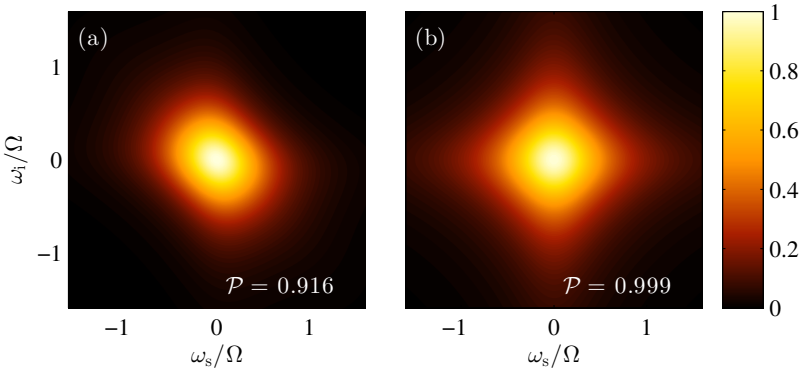

Figure 4.4: The normalized joint spectral intensity of a single signal-idler resonance pair for (a) a single Gaussian pulse that saturates the resonance, and (b) the double Gaussian pulse that interferometrically couples to the ring in time. Same parameters as in Fig. 4.4.

4.3.1 Numerical results

To illustrate the effect of the tailored pump spectrum, Fig. 4.5(a) and (b) shows how the JSI changes by going from the case of a single Gaussian pulse (left) to the dual-pulse Gaussian superposition (right). Using the same parameters as in Fig. 4.4, we find that the spectral correlation characterizing the single-pulse configuration is entirely removed by using the dual-pulse superposition. Remarkably, the resulting spectral purity is practically unity. However, this only demonstrates that our idea works for a specific parameter set of $(\eta, \Delta\tau)$. Therefore, to investigate how the scheme depends on these parameters, Fig. 4.5 shows the purity $\mathcal{P}(\eta, \Delta\tau)$ in the case of $\tau_p\Omega = 1/5$ (the behavior is very similar for other values of $\tau_p\Omega$). The purity is seen to be mirror symmetric in the sense that $\mathcal{P}(\eta, \Delta\tau) = \mathcal{P}(1-\eta, -\Delta\tau)$ as is also evident from Eq. (4.8). Promisingly, a large subset of the $(\eta, \Delta\tau)$-parameter space results in $\mathcal{P} > 0.92$, which is an improvement in comparison to the single-pump case recovered in the extremes $\eta = 0$ or $\eta = 1$. This improvement is observed in the region $(\eta > 1/2, \Delta\tau > 0)$, which corresponds to the early pulse being more energetic than the late pulse.

The increase in purity allowed by our dual-pulse scheme, comes at the cost of having less pump power in the resonator, and hence a lower generation probability R. This dependence is illustrated by the contours in Fig. 4.5, which represent different generation probabilities R relative to the single-pump case, for which we denote the probability R_0. These contours show how the generation probability increases as we move away from the point $(\eta = 1/2, \Delta\tau = 0)$, for which $R = 0$ [Note that with the construction of the dual-pulse spectrum in Eq. (4.8), the combined pulse energy proportional to $\int \mathrm{d}\omega |\alpha(\omega)|^2$ becomes dependent on η and $\Delta\tau$.]. Figure 4.6 shows the maximal purity as a function of τ_p

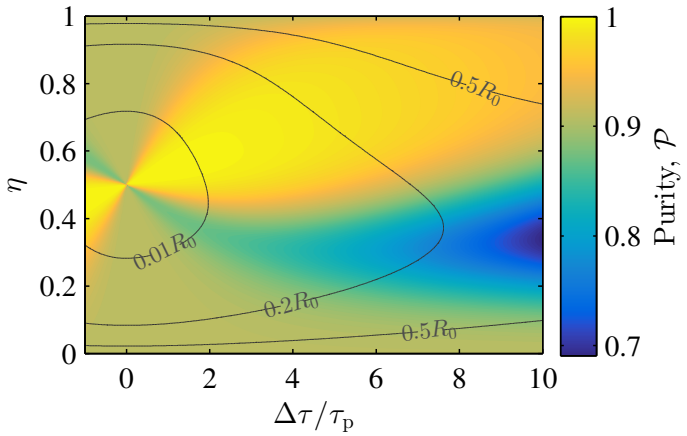

Figure 4.5: 2D-map of the purity $\mathcal{P}$ as a function of the dual-pulse splitting ratio η and temporal separation $\Delta\tau$, in the case of $\tau_p\Omega = 1/5$. Photon-pair-rate contours have been inserted to illustrate the penalty resulting from the interference-induced outcoupling.

under different generation-probability constraints. The bottom (blue) curve shows the single-pulse case, which saturates at 0.92 for pump pulses that are spectrally much broader than the resonance linewidth. For each value of τ_p, we denote the corresponding single-pump generation probability R_0, permitting us to evaluate the penalty in generation probability when using the dual-pulse scheme. The remaining curves were obtained by numerically maximizing $\mathcal{P}(\eta, \Delta\tau)$ (see Fig. 4.5) subject to the constraints $R/R_0 \geq 0.5$ (red), $R/R_0 \geq 0.2$ (yellow), and $R \geq 0$ (purple, unconstrained). Figure 4.6 illustrates that, even in the dual-pulse case, the purity remains low for temporally long pulses ($\tau_p\Omega > 1$). However, given that Eq. (4.8) was derived to minimize spectral entanglement based on the assumption of having a spectrally broad pump, this is not particularly surprising. However, for $\tau_p\Omega = 1/10$, a purity in excess of 0.99 can be achieved with $R > 0.2R_0$; a penalty in generation probability that, due to the quadratic scaling between pair-generation probability and pulse energy, can be compensated for by increasing the pulse energy by a factor 2.2.

4.4 Discussion and Summary

An immediate advantage of the dual-pulse scheme is that it can readily be implemented in already existing MRR-based photon-pair sources. Such an implementation requires a preparation setup comprised of an unbalanced Mach-Zehnder interferometer, in which the splitting ratio of the first beam splitter is η, the path difference is $\Delta\tau$, and the combining beam splitter is 50/50. Such an interferometer, which potentially could be integrated directly on-chip, would directly generate

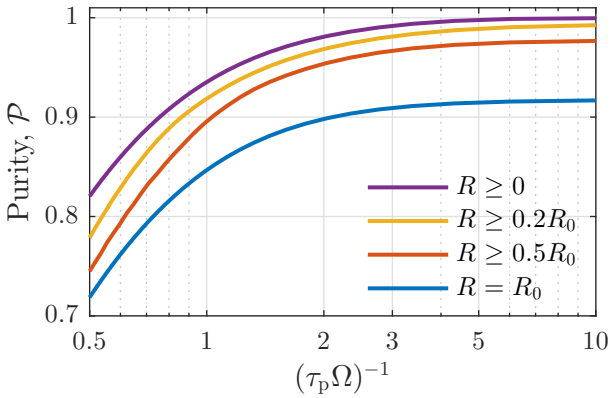

Figure 4.6: Purity $\mathcal{P}$, as a function of the normalized spectral pump width $(\tau_p\Omega)^{-1}$ with and without constraints on the relative pair-generation probability R/R_0, where R_0 is the generation probability in the single-pump case.

the spectrum given by Eq. (4.8) in one of its output ports. The required relative phase of π between the two pulses, see Eq. (4.8), makes a chip-integrated interferometer an especially appealing option. Alternatively, as a first demonstration, the required spectrum could be generated prior to coupling the pump light onto the chip using a commercial waveshaper.

With careful engineering of the MRR group-velocity dispersion it is possible to realize hundreds of 'identical' paired signal and idler resonances [109]. With the dual-pulse scheme functioning for standard MRRs, it appears like a promising route towards generating N-dimensional high-fidelity quantum frequency combs, where the N signal (idler) spectral modes have identical spectra, and contain no spectral correlation with their paired idler (signal) mode. In other words, our scheme would enable the generation of an ideal quantum frequency comb of the form $|\Psi\rangle = N^{-1/2}\sum_{j=1}^{N}|1_j\rangle|1_{-j}\rangle$, where $|1_j\rangle = \int \mathrm{d}\omega_j A(\omega_j)\hat{a}_j^\dagger(\omega_j)|0\rangle$, which have recently been demonstrated as an interesting resource for high-dimensional quantum information processing in the frequency domain [102, 103].

Another potential application of our dual-pulse scheme is in the context of a frequency-multiplexed single-photon source [110, 111]. The alpha-omega of multiplexing in the frequency domain is that the loss related to switching, which is imagined done using noise-free FWM Bragg scattering [31] (see Chap. 5), is constant with respect to the number of multiplexed modes (in stark contrast to that of spatial- or temporal multiplexing where losses scale unfavorably with the number multiplexing modes). As our dual-pulse scheme provides a means for spontaneously generating many pure-state heralded signal photons which are only distinguished by translations in frequency, it offers a promising route towards an on-chip near-deterministic frequency-multiplexed single-photon source.

In conclusion, we have presented a scheme for generating spectrally unentangled photon pairs using SFWM in standard MRRs. The developed method requires an input pump spectrum attainable by using two pulses with a π-relative phase shift, which are slightly separated in time. Such a pump configuration enables a broadened in-resonator pump spectrum, which is necessary for completely eliminating signal–idler spectral correlations. We further show that the proposed scheme is highly robust with respect to realistic experimental parameter uncertainties, making it a promising candidate for future on-chip implementation of high-purity heralded single photons.

Part III

Four-wave mixing Bragg scattering

CHAPTER 5

Four-wave mixing Bragg scattering in a birefringent waveguide

Whereas the preceding two chapters have dealt with the generation of photon pairs from spontaneous four-wave mixing in cubic nonlinear waveguides, we now skip to a different, albeit related, interaction known as four-wave mixing Bragg scattering. This chapter is an extended version of the work in [112], in which we presented a specific form of Bragg scattering that is capable of providing strongly uni-directional frequency conversion without altering the temporal waveform of the converted signal.

5.1 Introduction

One particular method of all-optical nonlinear signal processing is FWM Bragg scattering (BS), in which an input signal (s) is up- or downshifted to an output signal (r) by the frequency difference between two pump lasers (p and q), see Figs. 5.1(a) and (b). In contrast to FWM processes such as parametric amplification, which is inherently noisy, BS enables full conversion of an input signal without the addition of any noise [31]. For this reason, BS has attracted attention in quantum photonics as it allows signal processing of single- or few-photon level signals [113, 114]. This could be useful in quantum communications for shifting quantum signals between telecom wavelengths, where the transmission loss in optical fibers is lowest, and visible wavelengths quantum memories and solid-state nodes could be operating [115, 116, 117]. Shifting single photons between wavelength channels could be used for routing signals across quantum networks, or for quantum information processing with frequency encoding schemes [118, 119, 120].

Similarly, BS has applications in classical communications and all-optical ultra-fast signal processing and switching[121, 122, 123].

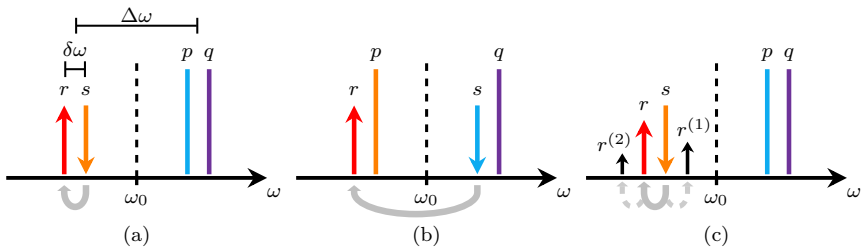

Figure 5.1: (a) Near- and (b) distant frequency conversion by BS for fields placed symetrically around the zero-dispersion frequency ω_0. The direction of the arrows indicate direction of energy flow, which may be reversed to achieve up-conversion. (c) In the near configuration, spurious Bragg scattering processes, generating the additional fields $\mathrm{r}^{(1)}$ and $\mathrm{r}^{(2)}$, may limit the conversion efficiency from s to r.

One practical challenge in BS is that of frequency *unidirectionality*. In general, BS allows for both up- and downconversion, which entails that the original energy at frequency ω_s is converted to energy at both $\omega_\mathrm{s} + \delta\omega$ and $\omega_\mathrm{s} - \delta\omega$ [124, 125, 126, 127]. This bidirectionality (represented by the field $\mathrm{r}^{(1)}$) is illustrated in Fig. 5.1(c), which at the same time illustrates the potential of cascaded conversion in the same direction ($\mathrm{r}^{(2)}$). In order to achieve a high conversion efficiency (CE) to the desired frequency at ω_r, action need to be taken to suppress these undesired process, e.g. by designing them to be strongly phase mismatched.

Another, yet unresolved, challenge in the framework of BS is that of achieving shape-independent and shape-preserving frequency conversion when the process is driven by short pump pulses. Intuitively, the use of pulsed pumps rather than CW pumps is advantageous in the sense that far lower average pump powers are required to achieve efficient conversion. However, in the setting of pulsed pumps, the nonlinear interaction strength varies in time, making the attainable CE strongly dependent on the temporal mode of the input signal, while at the same time strongly distorting the output signal [81, 128].

In this chapter, we provide solutions to the above-mentioned challenges by investigating a BS configuration where the two pump pulses are polarized on orthogonal axes of a nonlinear birefringent waveguide, or as recently demonstrated, propagate in different spatial modes of a higher-order mode fiber [74, 129]. The chapter is organized as follows: In Sec. 5.2 we introduce the concept and basics of BS, followed in Sec. 5.3 by a review of the standard configuration of BS and its limitations. In Sec. 5.4 we then introduce the cross-polarized BS configuration, and show it to exhibit highly unidirectional frequency conversion with the direction of conversion being controlled by the polarization of the input signal. Lastly, in Sec. 5.5, the proposed configuration is shown to preserve, and be independent of, the signal temporal shape even when driven by short pump pulses.

5.2 Basics of Bragg scattering

The BS interaction involves four fields: the input signal (s), the converted signal (r), and the two pumps that drive the energy conversion (p) and (q), see Fig. 5.1. The process requires the frequencies to obey energy conservation

$$\hbar\left(\omega_{\mathrm{p}}-\omega_{\mathrm{q}}+\omega_{\mathrm{s}}-\omega_{\mathrm{r}}\right)=0, \tag{5.1}$$

and hence the size of the frequency shift $\delta\omega=\omega_{\mathrm{s}}-\omega_{\mathrm{r}}$ is entirely determined by the difference between the two pump frequencies, i.e. $\omega_{\mathrm{q}}-\omega_{\mathrm{p}}$.

As in Chapter 3, we write down the CMEs describing the BS interaction. For simplicity we consider co-polarized CW fields,

$$\partial_z A_{\mathrm{p}} = i\beta(\omega_{\mathrm{p}})A_{\mathrm{p}} + i\gamma\left(|A_{\mathrm{p}}|^2 + 2|A_{\mathrm{q}}|^2\right)A_{\mathrm{p}}, \tag{5.2a}$$

$$\partial_z A_{\mathrm{q}} = i\beta(\omega_{\mathrm{q}})A_{\mathrm{q}} + i\gamma\left(|A_{\mathrm{q}}|^2 + 2|A_{\mathrm{p}}|^2\right)A_{\mathrm{q}}, \tag{5.2b}$$

$$\partial_z A_{\mathrm{s}} = i\beta(\omega_{\mathrm{s}})A_{\mathrm{s}} + 2i\gamma\left(|A_{\mathrm{p}}|^2 + |A_{\mathrm{q}}|^2\right)A_{\mathrm{s}} + 2i\gamma A_{\mathrm{p}}^* A_{\mathrm{q}} A_{\mathrm{r}}, \tag{5.2c}$$

$$\partial_z A_{\mathrm{r}} = i\beta(\omega_{\mathrm{r}})A_{\mathrm{r}} + 2i\gamma\left(|A_{\mathrm{p}}|^2 + |A_{\mathrm{q}}|^2\right)A_{\mathrm{r}} + 2i\gamma A_{\mathrm{p}} A_{\mathrm{q}}^* A_{\mathrm{s}}, \tag{5.2d}$$

where $\beta(\omega)$ is the frequency-dependent propagation constant. As in Eq. (3.7), the second term on the right-hand sides correspond to NPM effects while the last terms in Eqs. (5.2c) and (5.2d) are responsible for power conversion between (s) and (r). There is a subtle difference between Eqs. (5.2c) and (5.2d) and Eqs. (3.7c) and (3.7d) in the presence or absence of a complex conjugate on the last amplitude ($A_{\mathrm{i,s}}$). While the presence of the complex conjugation gives rise to parametric amplification (of vacuum fluctuations in Chapter 3), the absence of the complex conjugation gives rise to a beam-splitter like interaction where energy is exchanged between fields s and r[1].

Equations (5.2) may be considerably simplified by utilizing that, in the absence of losses, the pump powers are conserved such that $|A_{\mathrm{p}}(z)|^2 = P_{\mathrm{p}}$, and $|A_{\mathrm{q}}(z)|^2 = P_{\mathrm{q}}$, for pumps p and q, respectively. By defining $\bar{A}_j(z) = A_j(z)\exp\left[i\left(\beta(\omega_j)+2\gamma\left(P_{\mathrm{p}}+P_{\mathrm{q}}\right)\right)z\right]$ for $j\in\{s,r\}$ and similarly for the pumps, one finds

$$\partial_z \bar{A}_{\mathrm{p}} = \partial_z \bar{A}_{\mathrm{q}} = 0, \tag{5.3a}$$

$$\partial_z \bar{A}_{\mathrm{s}} = 2i\gamma \bar{A}_{\mathrm{p}}^* \bar{A}_{\mathrm{q}} \bar{A}_{\mathrm{r}} \exp\left[-i\left(\Delta\beta_{\mathrm{L}}+\Delta\beta_{\mathrm{NL}}\right)z\right], \tag{5.3b}$$

$$\partial_z \bar{A}_{\mathrm{r}} = 2i\gamma \bar{A}_{\mathrm{p}} \bar{A}_{\mathrm{q}}^* \bar{A}_{\mathrm{s}} \exp\left[i\left(\Delta\beta_{\mathrm{L}}+\Delta\beta_{\mathrm{NL}}\right)z\right], \tag{5.3c}$$

where we have defined the wavenumber phase mismatch

$$\Delta\beta_{\mathrm{L}} = \beta(\omega_{\mathrm{p}}) - \beta(\omega_{\mathrm{q}}) + \beta(\omega_{\mathrm{s}}) - \beta(\omega_{\mathrm{r}}), \tag{5.4}$$

and the nonlinear wavenumber mismatch

$$\Delta\beta_{\mathrm{NL}} = \gamma(P_{\mathrm{q}} - P_{\mathrm{p}}), \tag{5.5}$$

[1] In fact the total signal power is conserved, i.e. $\partial_z(|A_s|^2 + |A_r|^2) = 0$, as may easily be checked.

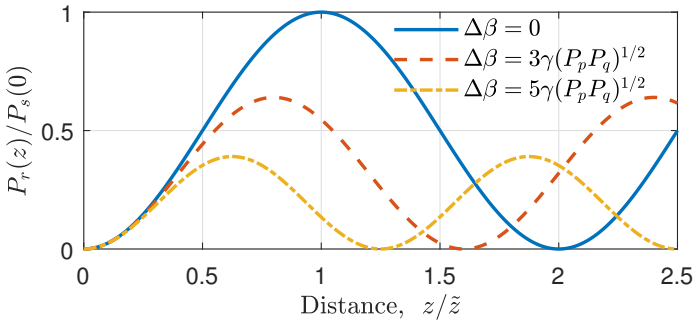

Figure 5.2: BS oscillations for different values of the combined wavenumber mismatch $\Delta\beta$. Full signal conversion is only achieved if the wavenumber mismatch vanishes.

respectively. Interestingly, the simple form of Eq. (5.3), allows an analytic solution to be found. In particular, if we consider the arguably most interesting case where $\bar{A}_{\rm r}(0) = 0$, the power transfer is given by the formula

$$\frac{P_{\rm r}(z)}{P_{\rm s}(z=0)} = \frac{16\gamma^2 P_{\rm p}P_{\rm q}\sin^2\left[\frac{1}{2}\left(\Delta\beta^2 + 16\gamma^2 P_{\rm p}P_{\rm q}\right)^{1/2} z\right]}{\Delta\beta^2 + 16\gamma^2 P_{\rm p}P_{\rm q}}, \tag{5.6}$$

where we have defined the combined phase mismatch $\Delta\beta = \Delta\beta_{\rm L} + \Delta\beta_{\rm NL}$. Equation (5.6) is plotted in Fig. 5.2 with the distance z normalized to $\tilde{z} \equiv \pi/[(16\gamma^2 P_{\rm p}P_{\rm q})^{1/2}]$ for three different values of the phase mismatch $\Delta\beta$. Full conversion is only observed in the perfectly phase-matched case $\Delta\beta = 0$. The conversion is oscillatory with a period that depends both on the nonlinear interaction strength and the size of the phase mismatch according to $z_{\rm per} = 2\pi/(\Delta\beta^2 + 16\gamma^2 P_{\rm p}P_{\rm q})^{1/2}$. With the oscillatory period decreasing for increasing phase mismatch, the oscillatory behavior observed in FWM-BS is very similar to the light-matter interaction known as Rabi flopping, and in fact there is a strong mathematical analogy between the two effects [130].

5.3 The standard configuration

5.3.1 Phase-matching and bandwidth

Following the introduction to BS given in Sec. 5.2, we now discuss the standard BS configuration for co-polarized fields that are centered around a zero-dispersion frequency (ZDF) [131]. We label the input signal s, the output r, and the pumps p and q, as shown in Fig. 5.1. The wavenumber mismatch for the down-shifting case [Figs. 5.1(a) and (b)], is given by (see also above)

$$\Delta\beta = \beta(\omega_{\rm s}) - \beta(\omega_{\rm r}) + \beta(\omega_{\rm p}) - \beta(\omega_{\rm q}) + \gamma(P_{\rm q} - P_{\rm p}), \tag{5.7}$$

where $\beta(\omega)$ is the wavenumber at angular frequency ω, γ is the nonlinear coefficient proportional to the intensity-dependent refractive index n_2, and P_p and P_q are the pump powers. Notably, the nonlinear contribution to the wavenumber-matching condition cancels if the two pump powers are equal. The wavenumber as a function of frequency can be expanded as

$$\beta(\omega) = \beta_0 + \beta_1\omega + \beta_3\omega^3/6 + \mathcal{O}(\omega^4), \tag{5.8}$$

where ω is measured relative to a ZDF, in which case the second-order dispersion term vanishes, i.e. $\beta_2 = 0$. For balanced pump powers, it follows that wavenumber matching, i.e. $\Delta\beta = 0$, is obtained by placing the fields symmetrically around the zero-dispersion wavelength, such that $\omega_\mathrm{s} = -\omega_\mathrm{p}$ and $\omega_\mathrm{r} = -\omega_\mathrm{q}$. With this placement, insertion of Eq. (5.8) into Eq. (5.7) directly leads to cancellation of the terms of odd order in ω, while the static terms trivially vanish. Such placement of the fields furthermore leads to group-velocity matching of s to p, and of r to q, as can be seen from the group slowness

$$\beta^{(1)}(\omega) = \mathrm{d}\beta/\mathrm{d}\omega = \beta_1 + \beta_3\omega^2/2 + \mathcal{O}(\omega^3), \tag{5.9}$$

providing convenient visualization of the phase-matching criterion (see below).

In the standard configuration the third-order dispersion coefficient β_3 plays an important role in setting the allowed signal bandwidth, and in determining the degree to which other nonlinear processes are suppressed, or allowed. To estimate the phase-matching bandwidth, we break the symmetry by allowing ω_s to deviate from $-\omega_\mathrm{p}$ (and hence ω_r from $-\omega_\mathrm{q}$), while fixing $\delta\omega = \omega_s - \omega_r$. Thereby, the wavenumber mismatch is given by

$$\Delta\beta = \frac{\beta_3\delta\omega\Delta\omega}{2}(\omega_\mathrm{p} + \omega_\mathrm{s}), \tag{5.10}$$

with $\Delta\omega$ being the separation between the average frequency of the pumps and that of the input/output signal, as shown in Fig. 5.1(a). Note that the wavenumber mismatch in Eq. (5.10) indeed vanishes for $\omega_\mathrm{s} = -\omega_\mathrm{p}$. In a waveguide of length L, efficient conversion occurs for accumulated phase-mismatches $|\Delta\beta L| \ll 1$, resulting in the following condition for the signal bandwidth Ω_s

$$\Omega_\mathrm{s} \ll \left|\frac{4}{\beta_3\delta\omega\Delta\omega L}\right|, \tag{5.11}$$

where a factor of 2 stems from considering the two-sided bandwidth.

5.3.2 Unidirectionality

Consider now the influence of spurious BS processes, which are sketched in Fig. 5.1(c). These processes must be well suppressed in order to obtain a high CE in the desired direction [132]. To quantify this, we consider the configuration for desired down-shifting from s to r. When the desired process is perfectly wavenumber

matched, the wavenumber mismatch for the spurious up-shifting process, s to $\mathrm{r}^{(1)}$, is given by

$$\Delta\beta_{\mathrm{spur}} = \beta(\omega_{\mathrm{s}}) - \beta(\omega_{\mathrm{s}} + \delta\omega) - \beta(\omega_{\mathrm{p}}) + \beta(\omega_{\mathrm{q}}) = \beta_3\omega_{\mathrm{p}}\delta\omega^2, \tag{5.12}$$

with $\omega_{\mathrm{s}} + \delta\omega$ being the frequency of up-shifted light. From this, we deduce the condition for suppressing the unwanted up-shifting process ($|\Delta\beta_{\mathrm{spur}}L| \gg 1$)

$$|\beta_3\omega_{\mathrm{p}}\delta\omega^2 L| \gg 1, \tag{5.13}$$

which shows that the spurious BS process may be particularly difficult to suppress for small frequency shifts $\delta\omega$. A very similar condition applies for suppressing the process where converted light to ω_{r} is down-shifted a second time, i.e. r to $\mathrm{r}^{(2)}$:

$$\left|\beta_3\omega_{\mathrm{q}}\delta\omega^2 L\right| \gg 1. \tag{5.14}$$

Notably, by combining the conditions for unidirectionality [Eqs. (5.13) and (5.14)] with the attainable BS bandwidth [Eq. (5.11)], one finds that unidirectional operation is only possible for a signal bandwidth that is much smaller than the frequency shift, i.e. $\delta\omega \gg \Omega_{\mathrm{s}}$. This could be detrimental to applications of frequency conversion for dense wavelength division multiplexing systems, where the channel separation is comparable to the bandwidth of each channel.

The impact of undesired bidirectional conversion is quantified by solving the coupled-mode equations for the BS process, including multiple signal modes (for details, see Appendix E). Figure 5.3(a) shows the highest attainable CE as a

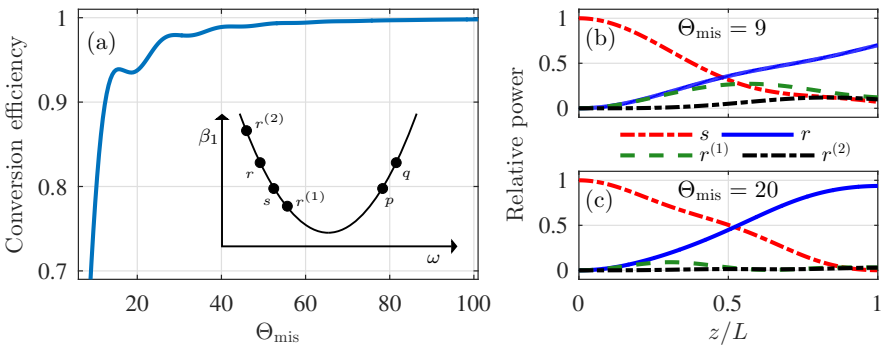

Figure 5.3: (a) Maximal conversion efficiency as a function of the dimensionless mismatch parameter $\Theta_{\mathrm{mis}} = \beta_3\Delta\omega\delta\omega^2 L$. For small mismatches, undesired Bragg scattering modes, $\mathrm{r}^{(n)}$, become significant, and thereby limit the conversion efficiency from s to r. The inset shows the phase-matching diagram interpreted as a parabola in (ω, β_1)-space and the placements of the various fields. (b) and (c) show the relative power transfer versus waveguide distance between the input signal s (dashed-dotted, red) the desired output r (full, blue), the undesired bidirectional output $\mathrm{r}^{(1)}$ (dashed, green), and the cascaded converted output $\mathrm{r}^{(2)}$ (dashed-dotted, black), for $\Theta_{\mathrm{mis}} = 9$ and $\Theta_{\mathrm{mis}} = 20$, respectively.

function of the dimensionless product $\Theta_{\text{mis}} = \beta_3 \Delta\omega \delta\omega^2 L$ (representing the average value of Eqs. (5.13) and (5.14)), for desired down-conversion [see Fig. 5.1(c)]. The pump powers (which is CW and balanced, $P_{\text{p}} = P_{\text{q}}$) are in all cases chosen such that a CE of unity is obtained without the inclusion of the undesired Bragg-scattering modes, $\text{r}^{(n)}$ [i.e. $2\gamma P_{\text{p}} L = \pi/2$ as seen from Eq. (5.6)]. For values $\Theta_{\text{mis}} > 50$, the attainable CE is near unity as undesired Bragg scattering processes are strongly suppressed by the large wavenumber mismatches given in Eqs. (5.13) and (5.14). However, for small values of the dimensionless product, the CE is limited to far below unity as a result of significant coupling to undesired signal modes. Furthermore, the CE-curve features small, and decaying, oscillations that arise due to the dynamical interaction between the multiple signal modes, as shown in Figs. 5.3(b) and (c).

As a consequence of the quadratic dependence of Θ_{mis} on $\delta\omega$, small frequency shifts are particularly difficult to achieve in a unidirectional fashion. As an example, for a 100-m long optical fiber with a third-order-dispersion coefficient of $\beta_3 = 1$ ps^3/km, a frequency shift of $\delta\omega = 2$ THz with the pumps placed $\Delta\omega = 20$ THz from the signals, yields $\Theta_{\text{mis}} = 8$. That is, according to Fig. 5.3, the frequency conversion process is far from unidirectional. This bidirectionality is an even larger hurdle in integrated waveguides, for which the length is limited to the order of centimeters, something which has been observed by multiple research groups in recent years [125, 126, 127]. This could potentially be overcome by a large pump-signal detuning $\Delta\omega$, which, on the other hand, is not always allowed due to the phase-matching requirement [110]. Fortunately, it was recently demonstrated that the bidirectionality might be alleviated by utilizing birefringence [133], and in the following we improve upon this concept.

5.4 Cross-polarized configuration

5.4.1 Phase-matching and bandwidth

To address the problems encountered with the standard configuration, we now consider an alternative setup where the two pumps are polarized on orthogonal axes of a birefringent nonlinear waveguide. The nonlinear waveguide is assumed to consist of a material for which the third-order susceptibility tensor takes the form $\chi^{(3)}_{ijkl} = a\delta_{ijkl} + b(\delta_{ij}\delta_{kl} + \delta_{ik}\delta_{jl} + \delta_{il}\delta_{jk})$ [134], where the indices i, j, k, l refer to the polarization state of an electric field and δ is the Kroenecker delta function. This form of the third-order susceptibility tensor encapsulates the properties of, for example, a silica fiber or a silicon waveguide, and entails that the converted output signal is polarized orthogonally to the input signal, as shown in Fig. 5.4(a).

We consider the case where the involved fields are placed far from the waveguide ZDF, resulting in a non-zero group-velocity dispersion β_2, which may be either negative or positive. In favor of a simple treatment, the group-velocity dispersion is

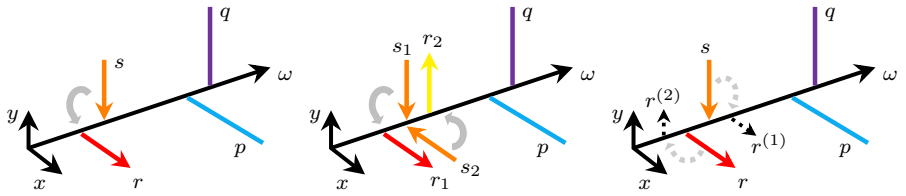

Figure 5.4: (a) In cross-polarized BS the converted output signal is orthogonal in polarization to the input signal. (b) The direction of conversion can be controlled by setting the polarization of the input signal. (c) Undesired BS processes are suppressed by waveguide birefringence, making the cross-polarized configuration unidirectional.

assumed to dominate over higher-order dispersion terms, and is assumed identical for the principle axes of the birefringent waveguide. Expanding the wavenumber around the average frequency $\omega_{\mathrm{av}} = (\omega_{\mathrm{s}} + \omega_{\mathrm{p}})/2$, the wavenumbers for the two principle axes are given as

$$\beta_{\pm}(\omega) = \beta_{0\pm} + \beta_{1\pm}\omega + \frac{\beta_2}{2}\omega^2 + \mathcal{O}(\omega^3), \tag{5.15}$$

where ω is relative to ω_{av}, and $\pm$ indicates the two principle axes of the waveguide. By an index '+' we shall without loss of generality refer to the slow axis, for which we take $\Delta\beta_1 \equiv \beta_{1+} - \beta_{1-} > 0$. If we now let pump p be polarized on the slow axis (and, consequently, let pump q be polarized on the fast axis), and the input signal s be polarized along the fast axis, the wavenumber mismatch for the process $(\omega_{\mathrm{s}} + \omega_{\mathrm{p}} \to \omega_{\mathrm{r}} + \omega_{\mathrm{q}})$ can be calculated as (using that $\delta\omega = \omega_{\mathrm{s}} - \omega_{\mathrm{r}} = \omega_{\mathrm{q}} - \omega_{\mathrm{p}}$ and $\omega_{\mathrm{s}} = -\omega_{\mathrm{p}}$)

$$\begin{aligned}
\Delta\beta &= \beta_-(\omega_{\mathrm{s}}) - \beta_+(\omega_{\mathrm{s}} - \delta\omega) + \beta_+(\omega_{\mathrm{p}}) - \beta_-(\omega_{\mathrm{q}}) \\
&= \beta_{1-}\omega_{\mathrm{s}} + \frac{\beta_2}{2}\omega_{\mathrm{s}}^2 - \beta_{1+}(\omega_{\mathrm{s}} - \delta\omega) - \frac{\beta_2}{2}(\omega_{\mathrm{s}} - \delta\omega)^2 \\
&\qquad + \beta_{1+}\omega_{\mathrm{p}} + \frac{\beta_2}{2}\omega_{\mathrm{p}}^2 - \beta_{1-}(\omega_{\mathrm{p}} + \delta\omega) - \frac{\beta_2}{2}(\omega_{\mathrm{p}} + \delta\omega)^2 \\
&= -\beta_2\delta\omega^2 - (2\omega_{\mathrm{p}}\beta_2 - \Delta\beta_1)\,\delta\omega + 2\omega_{\mathrm{p}}\Delta\beta_1.
\end{aligned} \tag{5.16}$$

Equation (5.16) is a second-order polynomial in the frequency shift $\delta\omega$, and can be shown to have the factorization

$$\Delta\beta = (\delta\omega + 2\omega_{\mathrm{p}})\left(\delta\omega - \frac{\Delta\beta_1}{\beta_2}\right). \tag{5.17}$$

The first root $\delta\omega = -2\omega_{\mathrm{p}}$ represents the trivial degenerate case where $\omega_{\mathrm{p}} = \omega_{\mathrm{r}}$ and $\omega_{\mathrm{q}} = \omega_{\mathrm{s}}$, and hence does not represent a case of energy transfer. On the other hand, the second root entails that the cross-polarized BS process is wavenumber matched, i.e. $\Delta\beta = 0$, whenever $\delta\omega = \omega_{\mathrm{q}} - \omega_{\mathrm{p}} = \Delta\beta_1/\beta_2$. Notably, the process occurs, exactly as does vector-modulation instability in birefringent waveguides,

for both normal ($\beta_2 > 0$) and anomalous ($\beta_2 < 0$) dispersion [75, 76]. By our convention, placing pumps p and q on the slow- and fast axes, respectively, in order to achieve phase matching one must choose $\omega_q > \omega_p$ for normal dispersion, and $\omega_q < \omega_p$ in the case of anomalous dispersion.

Remarkably, in complete contrast to the standard configuration, which allows perfect phase matching only for one specific signal frequency, the cross-polarized process appears to be wavenumber matched *independently* of the signal frequency, as long as the frequency separation between the pumps is to equal $\Delta\beta_1/\beta_2$. Note, that this is only exact here as we have neglected higher-order and polarization-mode dispersion effects. Moreover, the direction of the frequency shift is determined by the polarization of the input signal as sketched in Fig. 5.4(b). More specifically, if we let the input signal be polarized along the fast axis, we find $\omega_r = \omega_s - \Delta\beta_1/\beta_2$ resulting in a down-shift (an up-shift) for normal (anomalous) dispersion, while if the input signal is polarized along the slow axis, we obtain $\omega_r = \omega_s + \Delta\beta_1/\beta_2$ giving rise to an up-shift (a down-shift) for normal (anomalous) dispersion.

The phase-matching condition of the cross-polarized BS process leads to pairwise group-velocity matching of the pumps (p to q), and the signals (s to r), as can be seen by insertion of the shift $\delta\omega = \Delta\beta_1/\beta_2$ into

$$\beta_{\pm}^{(1)}(\omega) = \beta_{1\pm} + \beta_2\omega + \mathcal{O}(\omega^2). \tag{5.18}$$

This observation has an important implication, which we consider in the following section, and moreover provides a convenient way of visualizing the wavenumber-matching criterion for the cross-polarized BS process, see Fig. 5.5.

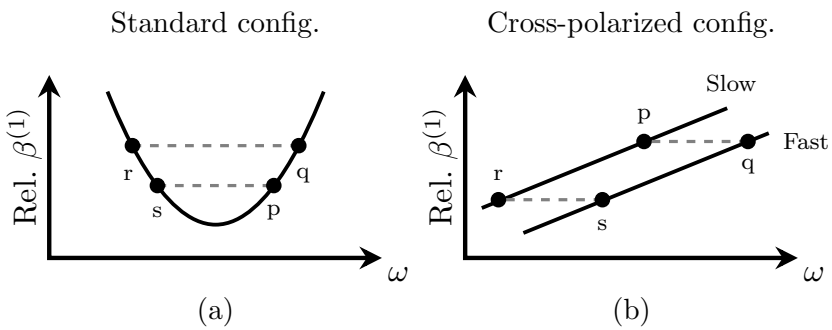

Figure 5.5: Phase-matching visualization using the relative inverse group velocity $\beta^{(1)}(\omega)$ for (a) the standard BS configuration and (b) the cross-polarized configuration.

5.4.2 Unidirectionality

As for the standard configuration, we now consider the effect of spurious BS. The wavenumber mismatch of this process [s to $r^{(1)}$ in Fig. 5.4(c)], can be found to

$$\Delta\beta_{\mathrm{spur}} = 2\Delta\beta_0 - \Delta\beta_1 \left(\Delta\omega + 2\delta\omega\right), \tag{5.19}$$

with $\Delta\beta_0 \equiv \beta_{0+} - \beta_{0-}$. Thus, to suppress the spurious BS, we require

$$\left| 4\pi \frac{L}{L_{\mathrm{B}}} - \Delta\beta_1 \left(\Delta\omega + 2\delta\omega\right) L \right| \gg 1, \tag{5.20}$$

where we have introduced the mode beat length of the birefringent waveguide, $L_{\mathrm{B}} = 2\pi/\Delta\beta_0$. Similarly, the suppression of the secondary BS process [r to $r^{(2)}$ in Fig. 5.4(c)], requires

$$\left| 4\pi \frac{L}{L_{\mathrm{B}}} - \Delta\beta_1 \left(\Delta\omega - 2\delta\omega\right) L \right| \gg 1, \tag{5.21}$$

differing from Eq. (5.20) only by the sign in front of the frequency shift $\delta\omega$. Noteworthy, in the cross-polarized configuration, the wavenumber mismatches of the undesired BS process contain one term inversely proportional to the beat length L_{B}, and another term proportional to the difference in inverse group velocity, $\Delta\beta_1$. For standard birefringent fibers with beat lengths on the order of 1–10 mm [135], the first term is typically orders of magnitudes larger than the second term for which $\Delta\beta_1 \approx 1$ ps/m (and $\Delta\omega \approx 5$–20 THz) [76, 129]. This is also the case in integrated birefringent waveguides, where the beat length can readily be made smaller than hundreds of microns at optical wavelengths [136, 137]. Hence, by employing a waveguide which is a few orders of magnitudes longer than its polarization-mode beat length, we may ensure that the undesired BS processes remain negligible.

5.5 Shape-preserving frequency conversion

The use of pulsed, rather than CW, pumps, entails the need for far smaller average pump-power levels. However, this also significantly complicates the spatial-temporal dynamics, and requires careful synchronization of the interacting fields. Moreover, the use of pulsed pumps typically prevents optimal signal CE for more than a single (or few) temporal shape(s), and results in a significantly altered temporal shape of the converted signal [81, 138]. In the following, we show that the cross-polarized BS configuration, introduced in Sec. 5.4, allows preservation of the signal temporal shape and, moreover, enables shape-independent frequency conversion.

5.5.1 Pump dynamics

Let us start by considering the pump dynamics. In our configuration, phase matching dictates co-propagating pumps ($\beta_{1\mathrm{p}} = \beta_{1\mathrm{q}} = \bar{\beta}$) and co-propagating signals ($\beta_{1\mathrm{s}} = \beta_{1\mathrm{r}}$). The undepleted coupled pump equations take the form

$$\left(\partial_z + \bar{\beta}\partial_t\right) A_{\mathrm{p}} = i\gamma \left(|A_{\mathrm{p}}|^2 + \frac{2}{3}|A_{\mathrm{q}}|^2 \right) A_{\mathrm{p}}, \tag{5.22}$$

$$\left(\partial_z + \bar{\beta}\partial_t\right) A_{\mathrm{q}} = i\gamma \left(|A_{\mathrm{q}}|^2 + \frac{2}{3}|A_{\mathrm{p}}|^2 \right) A_{\mathrm{q}}, \tag{5.23}$$

in which the amplitudes $A_{\mathrm{p,q}}$ are slowly varying envelopes in units of $\mathrm{W}^{1/2}$, and are assumed unaffected by intra-pulse dispersion. In Eqs. (5.22) and (5.23), the terms describing cross-phase modulation contain factors of 2/3, representing the case of orthogonally polarized fields in an isotropic material such as fused silica. This factor may be different if one considers the BS process using higher-order spatial modes [74, 129], or in a material with an anisotropic Kerr nonlinearity such as crystalline silicon [89]. We stress, however, that what follows does not depend on the value of this prefactor.

Optimal conversion in the third-order Kerr nonlinearity occurs when the two pump pulses are temporally matched, and we therefore consider the case where the initial pump pulses obey $A_{p_0}(0,t) = A_{q_0}(0,t)$. With this initial condition, the pump powers are balanced, which optimizes the nonlinear interaction per total amount of pump power, and the solution to the pump evolution becomes

$$A_p(z,t) = A_{p_0}(t - \bar{\beta}z) \exp\left(\frac{5i\gamma}{3} |A_{p_0}(t - \bar{\beta}z)|^2 z \right), \tag{5.24}$$

with $A_q(z,t) = A_p(z,t)$. The exponential in Eq. (5.24) accounts for both self- and cross-phase modulation, which contribute in the same manner as the pump pulses are group-velocity matched.

5.5.2 Signal dynamics

Consider now the Heisenberg-picture coupled-mode equations for the signal-mode operators. In the signal reference frame, so that now $\bar{\beta} = \beta_{1\mathrm{p}} - \beta_{1\mathrm{s}}$, we have

$$\partial_z \begin{bmatrix} a_{\mathrm{s}}(z,t) \\ a_{\mathrm{r}}(z,t) \end{bmatrix} = \mathbf{M}(z,t) \begin{bmatrix} a_{\mathrm{s}}(z,t) \\ a_{\mathrm{r}}(z,t) \end{bmatrix}, \tag{5.25}$$

where the system matrix $\mathbf{M}$ is given by

$$\mathbf{M}(z,t) = i\gamma \begin{bmatrix} 2|A_{\mathrm{q}}(z,t)|^2 + \frac{2}{3}|A_{\mathrm{p}}(z,t)|^2 & \frac{2}{3}A_{\mathrm{p}}^*(z,t)A_{\mathrm{q}}(z,t) \\ \frac{2}{3}A_{\mathrm{p}}(z,t)A_{\mathrm{q}}^*(z,t) & 2|A_{\mathrm{p}}(z,t)|^2 + \frac{2}{3}|A_{\mathrm{q}}(z,t)|^2 \end{bmatrix}, \tag{5.26}$$

where we have chosen s (r) to be co-polarized with q (p). In our case, we may define $A(z,t) \equiv A_p(z,t) = A_{\mathrm{q}}(z,t)$, recasting $\mathbf{M}$ into the simple form

$$\mathbf{M}(z,t) = \frac{2i\gamma}{3}\begin{bmatrix}4 & 1\\ 1 & 4\end{bmatrix}|A(z,t)|^2, \tag{5.27}$$

in which the matrix part is no longer spatially dependent. As a result, $\mathbf{M}$ commutes with itself at different spatial positions, i.e. $[\mathbf{M}(z',t),\mathbf{M}(z'',t)] = 0$, and therefore, Eq. (5.25) is solved by [139]

$$\begin{bmatrix}a_{\mathrm{s}}(z,t)\\ a_{\mathrm{r}}(z,t)\end{bmatrix} = \begin{bmatrix}G_{\mathrm{ss}}(z,z_0,t) & G_{\mathrm{sr}}(z,z_0,t)\\ G_{\mathrm{rs}}(z,z_0,t) & G_{\mathrm{rr}}(z,z_0,t)\end{bmatrix}\begin{bmatrix}a_{\mathrm{s}}(z_0,t)\\ a_{\mathrm{r}}(z_0,t)\end{bmatrix} = \mathbf{G}(z,z_0,t)\begin{bmatrix}a_{\mathrm{s}}(z_0,t)\\ a_{\mathrm{r}}(z_0,t)\end{bmatrix}, \tag{5.28}$$

where the 2×2 matrix transfer function is of the form $\mathbf{G}(z,z_0,t) = \exp\left[\int_{z_0}^{z}\mathrm{d}z'\mathbf{M}(z',t)\right]$. This further allows us to directly write down the solution as

$$\mathbf{G}(L,0,t) = \exp\left[4i\xi(t)\right]\times\begin{bmatrix}\cos\left[\xi(t)\right] & i\sin\left[\xi(t)\right]\\ i\sin\left[\xi(t)\right] & \cos\left[\xi(t)\right]\end{bmatrix}, \tag{5.29}$$

where we have defined the effective interaction strength

$$\xi(t) = \frac{2\gamma}{3}\int_{z_0=0}^{z=L}\mathrm{d}z'|A_0(t-\bar{\beta}z')|^2. \tag{5.30}$$

The exponential in Eq. (5.29) encompasses the combined effects of cross-phase modulation from the two pump pulses, whereas the matrix describes the time-dependent beam-splitter-like transformation, which is typical for nonlinear frequency-conversion processes [140]. As is apparent from Eq. (5.30), the CE efficiency of a time slice t_k depends on the interaction strength experienced by that time slice according to $\sin^2[\xi(t_k)]$. Therefore, in general, the converted signal is a distorted version of the input signal. However, if the input signal experiences a complete temporal collision with the pumps (a complete walk-off), then the CE is time-independent (CW-like), and the signal shape is preserved. Remarkably, this shape-preserving property, which is unique to our configuration, holds for both arbitrary input signal- and pump shapes.

5.5.3 Examples with Gaussian pumps

We now consider a few examples, and, for simplicity, consider Gaussian-shaped input pump pulses of the form

$$A_0(t) = \left(\frac{\bar{E}}{\pi^{1/2}\tau}\right)^{1/2}\exp\left[-(t+t_0)^2/(2\tau^2)\right], \tag{5.31}$$

where $\bar{E}$ is the pulse energy and τ is the pulse duration (related to the root-mean square width T_{RMS} according to $\tau = \sqrt{2}T_{\mathrm{RMS}}$). The parameter t_0 determines the initial pulse center in our reference frame, and henceforth $t_0 = \bar{\beta}L/2$ is used to

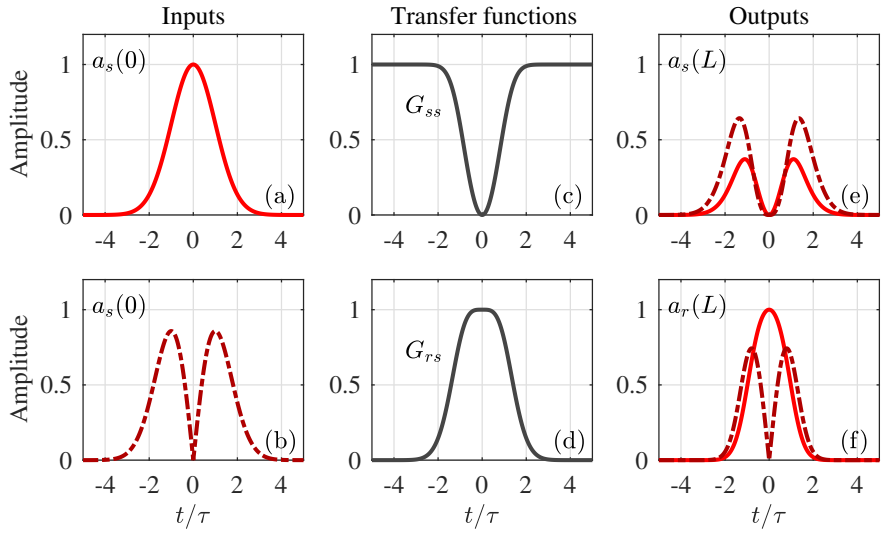

Figure 5.6: (a) Gaussian- and (b) first-order Hermite-Gaussian signal s inputs, which multiplied by (c) the self-transfer function G_{ss} and (d) the cross-transfer function G_{rs}, yields, (e) the remaining signal s outputs, and (f) the converted signal r outputs, respectively. The walk-off parameter, $\zeta = 2$, does not enable a full collision between the pumps and the signal resulting in temporally localized conversion.

ensure that the pump pulses are centered on $t = 0$ after a propagation distance of $z = L/2$. With the pulse shape in Eq. (5.31), one can readily show that Eq. (5.30) takes the explicit form

$$\xi(t) = \frac{\gamma \bar{E}}{3\bar{\beta}} \left[\mathrm{erf}\left(\frac{t}{\tau} + \frac{\zeta}{2}\right) - \mathrm{erf}\left(\frac{t}{\tau} - \frac{\zeta}{2}\right) \right], \tag{5.32}$$

where erf is the error function, and we have defined the dimensionless walk-off parameter $\zeta = \bar{\beta} L/\tau$, which quantifies the degree of walk-off between the pumps and a time slice of the signal. Notably, if a time slice t_k experiences a full collision with the pumps, then $\xi(t_k) = 2\gamma\bar{E}/(3\bar{\beta})$, and the CE (of this time slice) is then only dependent on the interaction strength $\gamma\bar{E}/\bar{\beta}$, which is a product of the nonlinearity γ, the pump peak power $\bar{E}/\tau$, and the walk-through distance $\tau/\bar{\beta}$.

Figure 5.6 illustrates the conversion dynamics in the case of $\zeta = 2$ for two different signal input pulse shapes: (a) a Gaussian input, and (b) a first-order Hermite-Gaussian input. The interaction strength is chosen such that the center of the signal, i.e. $t = 0$, is fully converted as illustrated with the transfer functions in Figs. 5.6(c) and (d). However, a value of $\zeta = 2$ only allows for a moderate degree of walk-off, resulting in a temporally localized conversion as shown in Figs. 5.6(e) and (f) for the remaining s-output and converted r-output, respectively. Notably, as the Hermite-Gaussian input signal contains only a small part of its energy around the pulse center, the total CE is only 53% compared to 85% for the Gaussian

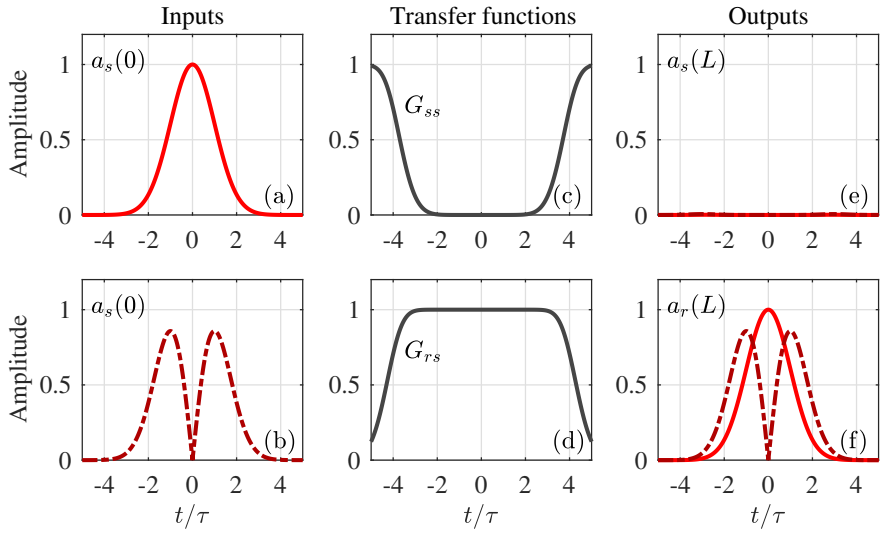

Figure 5.7: (a) Gaussian- and (b) first-order Hermite-Gaussian signal s inputs, which multiplied by (c) the self-transfer function G_{ss} and (d) the cross-transfer function G_{rs}, yields, (e) the remaining signal s outputs, and (f) the converted signal r outputs, respectively. The walk-off parameter, $\zeta = 8$, in this case enables a full collision between the pumps and the signal, resulting in shape-preserving conversion of both considered input signals.

input signal. Moreover, the converted signal is temporally narrower than the input signal, but is spectrally broadened due to the chirp received as a result of cross-phase modulation from the pumps.

The case of $\zeta = 8$ is shown in Fig. 5.7, using the same input signal pulses as in Fig. 5.6. Now the walk-off allows a full pump-signal collision, giving rise to transfer functions that are approximately constant within the signal duration, as seen in Figs. 5.7(c) and (d). This results in CEs of practically unity for both the Gaussian and the first-order Hermite Gaussian input signals, demonstrating that the configuration enables conversion of arbitrary temporal shapes with high efficiency. Moreover, irrespective of the signal input shape, this temporal shape is preserved in the frequency conversion process, as seen from Fig. 5.7(f).

Finally, it is highly instructive to make a comparison between the proposed pulsed scheme and the corresponding CW pumped configuration. In the CW pumped regime, the CE is simply determined by the product $\gamma P_{\mathrm{cw}} L$. On the other hand, when employing pulsed pumps, the conversion process typically becomes complicated, resulting in the CE being strongly dependent on the exact temporal shape, and timing, of the input signal. However, in this configuration, when the pumps are allowed to completely 'scan' through the signal, which somewhat alleviates the synchronization requirements between the pumps and the signal, the CE [see Eqs. (5.29) and (5.32)] becomes time-independent. Thus, one can

think of this configuration as being quasi CW-like, with a conversion efficiency being determined solely by the interaction strength $\gamma\bar{E}/\bar{\beta}$. Hence, in comparison to the CW case, the power-length product $P_{\mathrm{cw}}L$ is replaced by $\bar{E}/\bar{\beta}$. Thereby, to maintain a given CE moving from the CW regime to the pulsed regime, the peak power should merely satisfy $P_{\mathrm{peak}} = \bar{E}/(\pi^{1/2}\tau) = P_{\mathrm{cw}}\bar{\beta}L/(\pi^{1/2}\tau) \approx 5P_{\mathrm{cw}}$, where we have used that $\zeta \approx 8$ for a full collision with comparable signal and pump durations (see Fig. 5.7).

5.6 Discussion and Summary

In recent years, there have been proposals for using BS to perform all-optical switching and logic operations [121, 122]. The cross-polarized configuration adds an extra degree of freedom: polarization, and allows parallel operation of both polarization modes, which in the process are converted in opposite directions. Moreover, this scheme bears potential for enabling very large signal-conversion bandwidths as described in Sec. 5.4, where we assumed a simple waveguide-dispersion profile with polarization-independent group-velocity dispersion. Although this can be the design target, in practice, the waveguide dispersion is only approximately described by Eq. (5.15), and one may need to include a polarization-dependent group-velocity dispersion ($\beta_{2\pm}$). A more detailed treatment, which includes this effect, results in the frequency shift being given by $\delta\omega = \Delta\beta_1/\beta_{2,av}$, with $\beta_{2,av} = (\beta_{2+} + \beta_{2-})/2$. Moreover, this gives a signal bandwidth that scales as $[(\Delta\omega/2 + \delta\omega)\,\Delta\beta_2 L]^{-1}$, where, as previously, $\Delta\omega = |(\omega_p + \omega_q)/2 - (\omega_s + \omega_r)/2|$, and $\Delta\beta_2 = \beta_{2+} - \beta_{2-}$. Notably, the signal bandwidth scales inversely with $\Delta\beta_2$, which underpins the possibility for attaining ultra-high conversion bandwidth by careful dispersion tailoring. One also finds, that the inclusion of a polarization-dependent group-velocity dispersion opens the possibility for fine-tuning the frequency shift $\delta\omega$ simply by tuning the pump frequencies. Such tunability was not predicted by the simpler model neglecting polarization-dependent dispersion.

Finally, it is worth noticing that the cross-polarized BS process is designed to occur when the fields are placed far away from a waveguide ZDF. For this reason, the considered process is, in comparison to the standard BS configuration, to a lesser degree accompanied by other parasitic nonlinear processes such as parametric amplification. This is especially the case if the process is operated in the normal dispersion regime, for which scalar modulation instability is strongly suppressed. Moreover, spontaneous Raman scattering can, to a large extent, be avoided by cooling the nonlinear fiber and by placing the pumps on the low-frequency side of the signals [132], or by using a crystalline material such as silicon.

In conclusion, we have in this chapter investigated the properties of a four-wave mixing Bragg-scattering configuration, which employs cross polarized pumps in a birefringent nonlinear waveguide. Phase matching of this process, which can be achieved in both the anomalous or the normal dispersion regimes, occurs when the two pumps are placed in frequency such that they are group-velocity matched. The cross-polarized configuration has four distinct advantages compared to the

standard co-polarized Bragg-scattering configuration: (i) It allows a large signal bandwidth, which is not limited by the size of the frequency shift, (ii) the direction of conversion (up or down) is controlled by the polarization of the input signal, (iii) conversion is entirely unidirectional as undesired Bragg-scattering processes are suppressed by waveguide birefringence, and (iv) the pairwise group-velocity matching (pump-to-pump and signal-to-signal) enables shape-preserving frequency conversion of an arbitrary signal input temporal waveform.

Part IV

Amorphous silicon waveguides: Experimental work

CHAPTER 6

Design and characterization: Amorphous silicon waveguides

In this final part, we provide initial experimental results and thoughts towards realizing type-II cross-polarized four-wave mixing in an integrated setting.

6.1 Introduction and motivation

Integrated waveguides provide the capability of nonlinear signal processing in extremely small footprints. The large refractive-index difference between core and cladding material ($\Delta n > 1$) allows for ultra-tight light confinement on areas of $\sim (\lambda/n)^2$. This in turn enables low-radii waveguide bends ($R \sim 10$ μm) resulting in a large density of functionalities on a single photonic chip. Moreover, the high refractive index of integrated waveguides correlates with a large nonlinear Kerr index (n_2), which in co-operation with effective waveguide-mode areas that are an order of magnitude smaller than that obtainable with optical fibers, permits nonlinear functionalities such as FWM and supercontinuum generation to be realized on a length scale of sub-centimeters.

Crystalline silicon has often been the material of choice due to a mature fabrication processes, its high refractive index in the telecommunication window (3.48), and an impressive nonlinear coefficient n_2, which is approximately a factor of 100 larger than that found in glass-based optical fibers [141]. The silicon nonlinear platform has been a forerunner for integrated nonlinear photonics enabling demonstrations of e.g. stimulated Raman amplification [142], FWM-induced broadband amplification [77], and optical wavelength conversion [143]. On the other hand, the silicon platform is not without its limitations. Silicon suffers from nonlinear

absorption when the incident optical power reaches the level required for nonlinear optics functionalities. In particular, two-photon absorption (TPA), which mathematically stems from the imaginary part of the third-order susceptibility $\chi^{(3)}$, is the nonlinear-absorption process where two photons are simultaneously absorbed to raise a valence electron to the conduction band. Subsequently, the resulting carriers can, before relaxation, undergo a secondary process called free-carrier absorption (FCA), where the electron (hole) moves to a higher-energy conduction-band (valence-band) state by absorbing incoming light. As silicon has an electronic bandgap of ~ 1.1 eV avoiding the nonlinear TPA effect requires operation with $\lambda > 2$ μm well above the telecommunications window. This ultimately limits the use of crystalline silicon for nonlinear signal processing, which has stimulated the search for other nonlinear integrated platforms.

Inspired from the photovoltaic industry, one of these alternative platforms is *amorphous* silicon, a-Si. Unlike crystalline silicon which has a very well-defined structure with each Si-atom being tetrahedrally bonded, the atoms in a-Si are arranged with no particular long-range repeated structure. This lack of periodic structure entails that a fraction of the silicon atoms are left with dangling bonds, which from an optical point-of-view form undesired defect states. The dangling bonds may be passivated by hydrogen atoms by including H_2 in the plasma-enhanced chemical-vapor deposition (PECVD) process used to create thin films of hydrogenated amorphous silicon (a-Si:H). Even through the passivation process, however, a-Si:H suffers from metastable changes in the bonding structure when illuminated by intense light. This observation, first made by Staebler and Wronsk [144], and since referred to as the Staebler-Wronski effect, is to this day not fully understood [145]. Despite of this, a-Si:H possesses many of the same desired features as crystalline silicon for nonlinear photonics. This includes a cheap and CMOS-compatible fabrication procedure, and a remarkable linear refractive index ($n > 3.5$ at telecommunications wavelengths). Notably, tuning the PECVD process, used in the growth process of the a-Si:H thin film, enables tailoring of the energy band structure so that the TPA edge approaches or even enters the L- or C-bands [146]. As a result, a-Si:H waveguides can reach nonlinear figure of merits[1], which is significantly larger than for crystalline silicon [147, 148]. Moreover, with the PECVD process used to grow the initial a-Si:H layer, the a-Si platform permits the waveguide height to be a tunable parameter that can be used for dispersion tailoring. This is in contrast to production lines of crystalline silicon waveguides, which are wafer based and therefore have a predetermined height, typically around 220 nm. As we shall see in Sec. 6.2, this freedom turns out to be rather essential, and was in fact the 'deal-maker' in favor of the a-Si:H platform for attempting to realize the cross-polarized FWM processes on chip (see Chapters 3 and 5).

In this chapter, we provide design considerations, and preliminary experimental characterization, of waveguides tailored to realize the cross-polarized FWM schemes proposed in Chapter 3 and Chapter 5. We first provide detailed simulations of waveguide modes and their dispersion in Sec. 6.2, while we, in Sec. 6.3,

[1]The nonlinear figure of merit is defined as the ratio between the Kerr coefficient γ and the TPA coefficient, β_{T}.

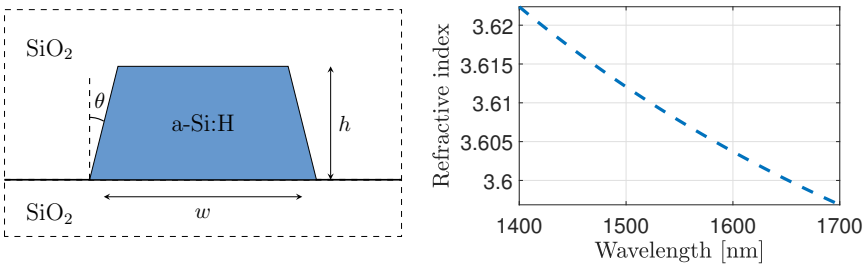

(a) (b)

Figure 6.1: (a) Sketch of a-Si:H waveguide buried in glass, and (b) material refractive-index profile of the a-Si:H measured through ellipsometry, courtesy of Lars. H. Frandsen.

shortly summarize the used fabrication method and consider the inter-connection challenge between optical fibers and the a-Si:H on-chip waveguides. In Sec. 6.4 we, shortly, present polarization-dependent loss measurements, which exhibit puzzling spectral features that we discuss. Lastly, in Sec. 6.5 we review a recently suggested means for measuring waveguide dispersion of test devices with a low net dispersion, and apply it to provide an estimate of the relative mode group index of some of our waveguides.

6.2 Waveguide design: Dispersion

To come up with a design for demonstrating the cross-polarized FWM process in an integrated a-Si photonic waveguide, a couple of design requirements had to be taken into account. First, the cross-polarized FWM processes of interest requires operation at wavelengths that are far separated from any ZDF of the two participating waveguide modes: the quasi-transverse electric (TE) mode and the quasi-transverse magnetic (TM) mode. These two modes should moreover experience the same sign of dispersion, i.e. normal or anomalous dispersion. This is a necessity in order to form the phase-matching parallelogram discussed in Chapter 3. To obtain this, we consider square-like waveguides where the cross-sectional dimensions, the height, h, and the width, w, are similar. In a compromise between tightly confining the fundamental modes in the core region while simultaneously limiting higher-order-mode content, we decided to go for waveguides with heights of $h \sim 400$ nm.

Figure 6.1(a) shows a sketch of the simulated waveguide cross section, indicating the height, h, the width, w, and the sidewall inclination angle θ. The buffer layer and the top-cladding layer consist of silica with a refractive index of 1.444 at $\lambda = 1550$ nm, while the core region consists of a-Si:H having the refractive-index profile shown in Fig. 6.1, which is a fit of experimental data obtained by

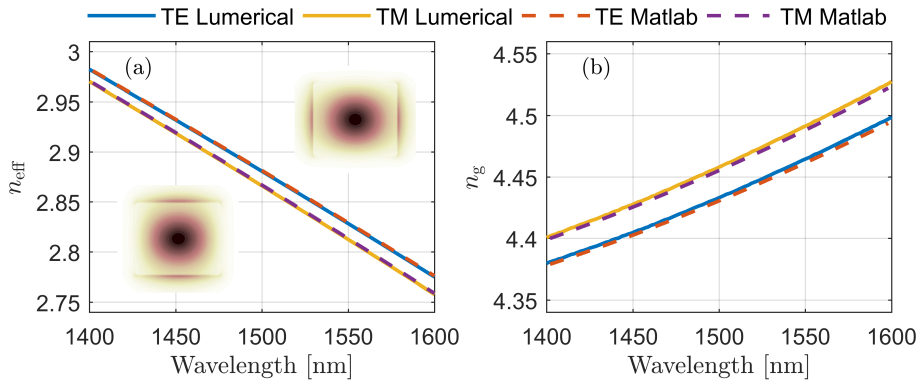

Figure 6.2: (a) Simulated effective refractive index of an a-Si:H rectangular waveguide that is 404 nm tall and 416 nm wide. Insets show the corresponding TE- and TM modes at 1550 nm. (b) Derived group refractive index of the guided TE- and TM mode, respectively.

ellipsometry. Note the large refractive index value of $n \approx 3.6$. The eigenmode problem of determining the waveguide modes and their propagation constants was solved independently with two different mode solvers to assure validity; one non-commercial mode solver in Matlab [149], and one commercial Lumerical mode solver. Using both solvers, Fig. 6.2 shows the obtained effective mode indices, $n_{\mathrm{eff}}(\lambda)$ along with the TE- (top right) and the TM mode (bottom left) field intensities, and the derived group indices, $n_{\mathrm{g}}(\lambda) = c/v_{\mathrm{g}}(\lambda)$ for a waveguide dimension of $h = 404$ nm, $w = 416$ nm, and $\theta = 0$. The two mode solvers agree well, with the small deviation expected to stem from minor discretization issues for the Matlab solver [plots here are obtained with a discretization area of (4×4) nm^2].

The waveguide simulated in Fig. 6.2 has a width that is slightly larger than the height, and this results in a mode birefringence of $\Delta n_{\mathrm{eff}} = n_{\mathrm{eff}}^{(\mathrm{TE})} - n_{\mathrm{eff}}^{(\mathrm{TM})} \approx 0.015$. However, as discussed back in Sec. 3.2 it is the inverse group velocity, $\beta^{(1)}$, and hence the group index n_{g}, which determines the phase-matching property of the type-II FWM processes. The group-index profiles are seen to increase as a function of wavelength revealing that the dispersion of both modes is anomalous. Moreover, the two group-index curves are characterized by very similar group-index slopes and feature GVD values of $\beta_2 \approx -1$ ps^2/m. As discussed in Sec. 3.2, such close-to-parallel curves is exactly what facilitates phase-matching of the type-II FWM process. In particular, based on Eq. (3.5), the phase matched signal- and idler wavelengths are determined as

$$\lambda_{\mathrm{i,s}} = \frac{2\pi c}{\omega_{\mathrm{p}} \pm \frac{\Delta n_{\mathrm{g}}}{c\beta_{2,\mathrm{av}}}} = \frac{\lambda_{\mathrm{p}}}{1 \pm \frac{\Delta n_{\mathrm{g}} \lambda_{\mathrm{p}}}{2\pi c^2 \beta_{2,\mathrm{av}}}}, \tag{6.1}$$

where λ_{p} is the (degenerate) pump frequency, $\Delta n_{\mathrm{g}} = n_{\mathrm{g}}^{(\mathrm{TE})} - n_{\mathrm{g}}^{(\mathrm{TM})}$, and $\beta_{2,\mathrm{av}}$ is the

mode-averaged GVD parameter at the pump wavelength. Moreover, as $n_{\mathrm{g}}^{(\mathrm{TM})} > n_{\mathrm{g}}^{(\mathrm{TE})}$, the red-shifted sideband emerges in the TE mode while the blue-shifted sideband is TM polarized, see Fig. 3.1(b). Based on Eq. (6.1), one can obtain phase-matching contours as a function of the pump wavelength. These contours are shown in Fig. 6.3 demonstrating the extreme tunability of the process over more than 200 nm with an almost constant signal-pump detuning of $\sim 40\ \mathrm{nm} \pm 3\ \mathrm{nm}$.

The degree of waveguide birefringence may be controlled by altering the dimensions of the waveguide cross section. For example, by slightly changing the

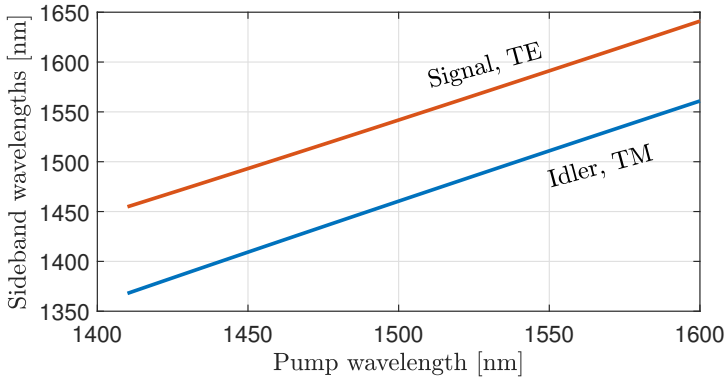

Figure 6.3: Calculated phase-matching contours of the type-II FWM process as a function of the degenerate pump wavelength for the waveguide considered in Fig. 6.2. The process is predicted to be tunable over more than 200 nm with respect to the pump wavelength.

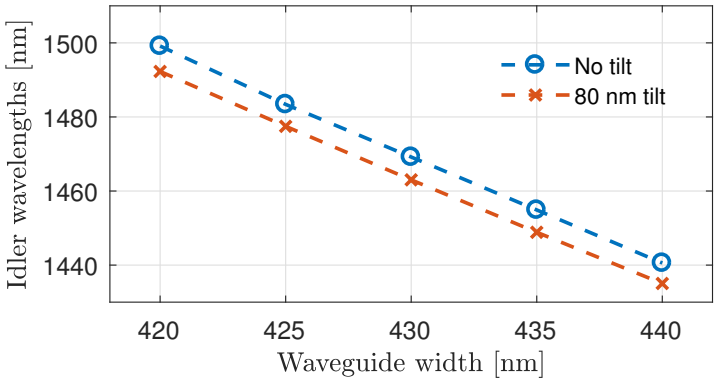

Figure 6.4: Simulated phase-matched idler frequency versus waveguide width for a pump wavelength of 1550 nm and a waveguide height of 404 nm. Simulations were performed both for a waveguide without tilt and a waveguide with a tilt corresponding to relative base difference of 80 nm. The results indicate that the tilted waveguides in general exhibit a slightly larger differential group index, Δn_{g}.

waveguide width, w, one may move the two curves in Fig. 6.2(b) either closer to each other (by decreasing w) or further away from each other (by increasing w). From the phase-matching condition expressed by Eq. (6.1), changing Δn_g directly translates into new phase-matched wavelengths. To demonstrate this, Fig. 6.4 shows the phase-matched idler frequencies for a waveguide height of 404 nm, and a fixed pump wavelength of 1550 nm, as the waveguide width w is varied from 420 nm to 440 nm. Evidently, the phase-matched frequencies depend strongly on the waveguide dimension, and from Fig. 6.4 one can read off a differential wavelength shift of $\delta\lambda/\delta w \approx 3$ nm/nm. With this kind of sensitivity, the type-II FWM process could potentially be used to assess the cross-section uniformity of integrated waveguides as the phase-matching bandwidth is smeared out. On the other hand, such a strong dependence on the waveguide dimension will, in the presence of longitudinal dispersion fluctuations, also result in a weaker effective nonlinear interaction. This could, if the dispersion fluctuations are too large, compromise an experimental demonstration of the type-II FWM process.

We further considered the effect of the waveguide having a non-zero tilt with a relative base difference of 80 nm ($\theta \approx 5.5$ deg.). The corresponding phase-matched idler frequencies are included in Fig. 6.4, in which case the waveguide width is given as the average base width of $w = w_{bot}/2 + w_{top}/2$. A small deviation from the results without waveguide tilts is observed, and the sign of the deviation indicates that the relative group-birefringence is increased by the introduced tilt. This effect is attributed to the TE mode (mainly) being perturbed by the slanted sidewalls.

6.3 Fabrication and optical interconnection

Our a-Si:H waveguide samples were fabricated based on a 404-nm thick a-Si:H film deposited on a 3-μm SiO_2 wafer using the PECVD technique at a temperature of 300 °C. Strip waveguides of widths from 376 nm to 444 nm, and three lengths of 7.7 mm, 11.7 mm, and 23.7 mm, were defined by electron beam lithography, and realized by etching the surrounding structure. Finally, a layer of 2 μm SiO_2 was deposited on top to form the upper cladding of the waveguides.

To optically interconnect the on-chip waveguides with off-chip optical fibers, each waveguide begins and ends in a 100-μm long inverse taper with a tip width designed to be 100 nm wide [150, 151]. This facilitates improved optical mode- and impedance matching to butt-coupled lensed optical fibers which are used to couple both in and out of the device. It is noted that this procedure is expected to result in a relatively better coupling performance for the fundamental TE mode compared to the TM mode as the latter is, due to our somewhat unconventional waveguide height of around 400 nm, still relatively confined at the taper tip.

6.4 Loss characterization

To measure the insertion loss of the waveguide samples, we used an experimental setup sketched in Fig. 6.5. A CW (Ando AQ4321) laser with a tuning range from 1520 nm to 1620 nm was used as light source. A 3-dB fiber-based coupler was used to split the light into two different paths each containing a polarization controller (PC). The two paths (hereinafter referred to as path 1 and path 2) were directed into a 2-by-1 optical switch whose output was connected to a lensed optical fiber (OZ Optics, spot size of 2.5 μm) used to couple light into the a-Si:H waveguides. The polarization controller of path 1 (path 2) was calibrated to TE polarized (TM polarized) light at the waveguide input using a separate waveguide sample with known polarization properties. Finally, the light coupled out of the waveguides, by a second lensed fiber, was directed to an optical spectrum analyser (OSA) which measured the output power level. By comparison with a reference measurement performed through by-passing the coupling stages and the a-Si:H waveguides, the waveguide polarization-dependent insertion loss was obtained.

The tested waveguides were to be 404 nm tall, but their designs varied in terms of waveguide width and length. In particular, the chip contained waveguides of six different designed widths, i.e. 376 nm, 390 nm, 404 nm, 416 nm, 430 nm, and 444 nm, all of which were fabricated in three different lengths of 7.7 mm, 11.7 mm, and 23.7 mm. Using an input power of ~ -4 dBm, the obtained polarization-dependent insertion-loss measurements are provided in Fig. 6.6. A seen tendency is that the insertion loss is generally lower for the TE mode than for the TM mode. This observation agrees well with the expectation that the inverse-taper coupling design should perform better for the TE polarization. Moreover, by relating the insertion losses for different waveguide length through a linear least-squares fit, one can estimate, respectively, the waveguide coupling loss and the propagation loss. Such linear fits are also included in Fig. 6.6, giving estimates of a per-fact coupling loss of 3.7 dB (5.5 dB) and a propagation loss of 4.4 dB/cm (3.5 dB/cm) for the TE mode (TM mode). Thus, while TM-polarized light experiences larger coupling-related losses, the propagation losses appear to be lower for the TM mode. Again, this is unsurprising given that the TE mode is more prone to scattering resulting from sidewall roughness.

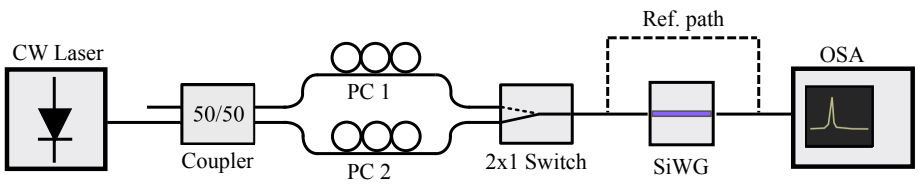

Figure 6.5: Sketch of the measurement setup used for measuring polarization-dependent waveguide loss. PC: Polarization controller, SiWG: Silicon waveguide, and OSA: Optical spectrum analyser.

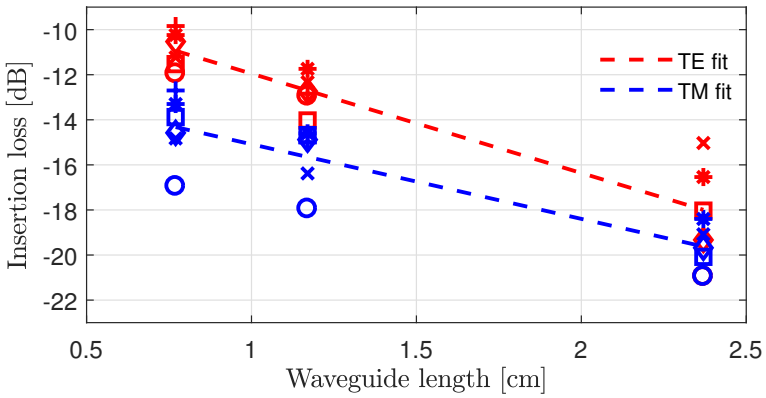

Figure 6.6: Measured polarization-dependent insertion loss of waveguides as a function of waveguide length. Tendency lines (first-order fit to averaged data) are included to guide the eye. Different types of markers correspond to different waveguide widths: 376 nm ('$*$'), 390 nm ('$+$'), 404 nm ('$\square$'), 416 nm ('x'), 430 nm ('$\diamond$'), and 444 nm ('$\circ$').

We further measured the wavelength-dependent insertion loss of the waveguides by synchronously sweeping the laser and the OSA from 1520 nm to 1620 nm. The results for the 7-mm long waveguides are shown in Fig. 6.7 for (a) launched TE polarization, and (b) launched TM polarization. Especially the plots representing the insertion loss of the TE mode is seen to feature surprising and distinct spectral "dips" which, in themselves, contain quick (sub-nanometer) oscillations and are approximately 5-10 nm wide. The spectral position of these dips are seen to be strongly waveguide dependent, appearing at a shorter wavelength as the waveguide width, and hence the effective-refractive index of the TE mode, decreases. Similar, albeit less pronounced, behavior is observed for TM-launched light in the broader waveguide samples (w = 404 nm, 416 nm, and 430 nm). However, in this case, the quick oscillations have been replaced by slow ($\sim$ 1 nm) oscillations, and the dips, moreover, occur at new wavelengths compared to the TE-polarized case. Besides the distinct spectral dips, the 404-nm wide waveguide sample indicates possible polarization-mode coupling through the $\sim$ 5 nm oscillation in the (orange) spectrum. This coupling is thought to be a result of six 50-nm radii half-circle bends included in the design of all waveguides, and was mainly observed for the 404-nm wide waveguides, likely explained by the remaining waveguides exhibiting a stronger degree of birefringence.

The origin of the spectral dips observed in Fig. 6.7 are still unexplained. As the waveguide is weakly supporting two higher-order quasi-modes (with effective indices of approximately 1.7 and 1.9), a "logical" interpretation might be to attribute the dips to higher-order-mode coupling. This coupling could occur in the inverse tapers [152], in the waveguide bends [153], or throughout the waveguide due to the horizontal asymmetry induced by the tilted ($\theta \approx 5.5°$) sidewalls [154]. Moreover, such coupling could potentially explain the large extinction ratio of

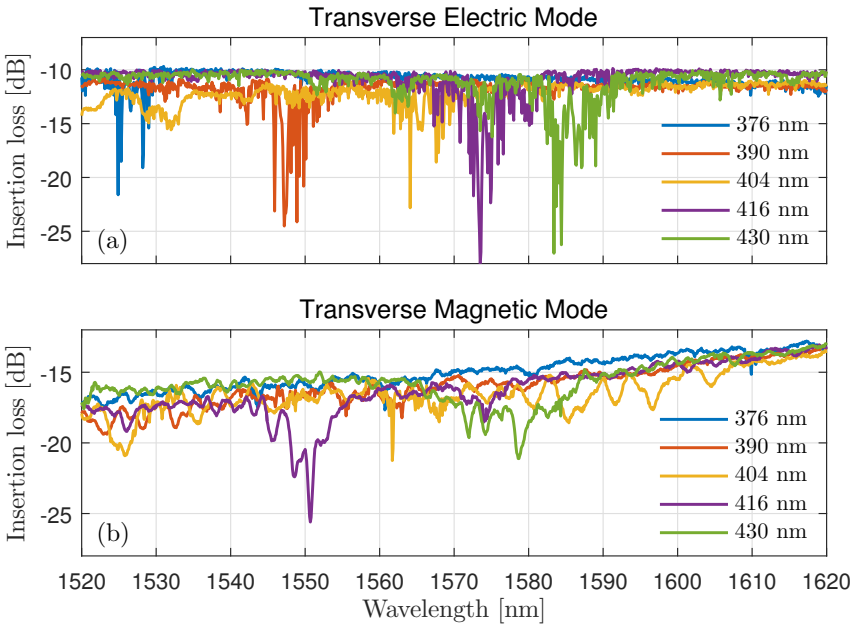

Figure 6.7: Measured wavelength-dependent insertion loss of 7.7-mm long waveguides for (a) TE-polarized light, and (b) TM-polarized light. Especially the TE mode is seen to exhibit very distinct spectral features in the form of 5-10 nm bands with high insertion loss.

the dips as the higher-order modes would be stripped off by the output coupling mechanism. However, it is not immediately obvious why such higher-order-mode coupling would be so relatively narrowband, i.e. 5 nm – 10 nm. A hint towards the origin of the dips is given in the next section where we analyse the dispersion through a stimulated FWM experiment.

6.4.1 The spectral dips: four-wave mixing analysis

We performed a FWM experiment in which a TE-polarized pump at 1530 nm was coupled into the 7.7-mm long and 416-nm wide a-Si:H waveguide along with a, likewise, TE-polarized signal. While keeping the wavelength of the pump fixed, the signal wavelength was tuned from 1531 nm to 1611 nm and the output spectra, along with the generated idlers, were measured by an OSA. The pre-chip pump and signal power levels were ~ 15 dBm and ~ 5 dBm, respectively.

The idler output power versus (idler and signal) wavelength is shown in Fig. 6.8. While the behavior for small signal-pump detunings (1530 nm $< \lambda_s <$ 1570 nm) looks much like expected with a slowly decreasing CE as the phase-mismatch increases, we observe a peculiar peak in the idler CE at around $\lambda_i = 1490$ nm

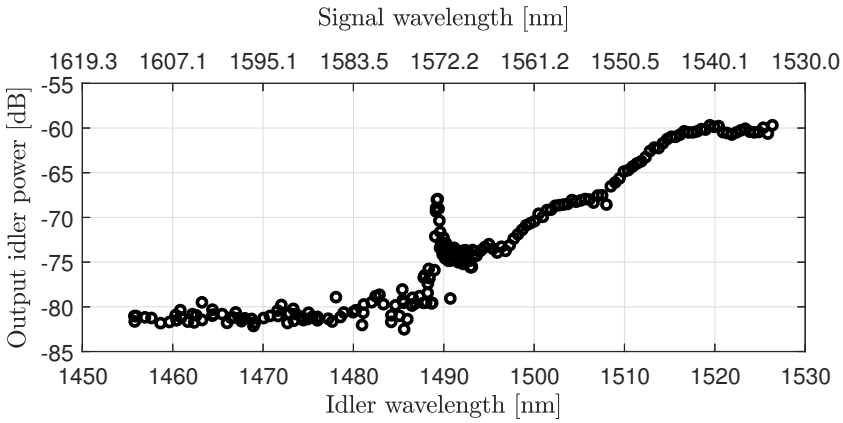

Figure 6.8: Signal-seeded FWM spectrum for the 416-nm wide 7.7-long waveguide pumped at a wavelength of $\lambda_p = 1530$ nm. For a specific signal-pump detuning, corresponding to an idler wavelength of $\lambda_i \approx 1490$ nm, the generated idler power suddenly grows by ~ 6 dB.

($\lambda_s = 1572$ nm). Here, the CE suddenly increases (by approximately 6 dB) in a narrow bandwidth of approximately 1 nm. This feature seems to be connected to the spectral dip observed in the transmission spectrum for the TE mode in Fig. 6.7(b), which for the 416-nm wide waveguide occurs at around $\lambda \approx 1575$ nm. We expect that the spectrally localized loss, due to the Kramers-Kronig relations, gives rise to a dispersive phase. This phase contribution then partly cancels out the, otherwise, large FWM phase mismatch, and thereby increases the idler CE in a narrow bandwidth. This, however, strongly suggests that the spectral dips observed in Fig. 6.7 are due to a distributed loss- or scattering phenomena. Moreover, in this experiment we had configured the input- and output such that the 50-nm radii waveguide bends (which were placed near one edge of the chip), were near the output-coupling side. Thus, we do not expect the bends to have played a significant role in the FWM experiment.

6.5 Dispersion characterization

Due to the presence of the nonlinear-loss mechanisms TPA and FCA, it is not realistic to observe the type-II FWM interaction simply by using a pulsed laser to spontaneously amplify vacuum fluctuations at the phase-matched signal- and idler wavelengths. Instead, one must resort to seeding the process by an input signal, which then poses the additional questions: at what wavelength, and in which polarization, should the seed be? To answer these questions, detailed knowledge of the waveguide dispersion is necessary. In this section we investigate a recently proposed method for measuring the dispersion of integrated waveguides [155], and

we furthermore use it to estimate the inter-modal group dispersion of the two fundamental polarization modes of our waveguides.

6.5.1 Concept and experimental setup

The concept of the adopted measurement technique is described in detail in [155, 156], but is revisited here for completeness. Consider two mutually coherent optical tones separated in frequency by a spacing of $2\Delta f$ where Δf is some radio frequency (RF). The total CW electric field is given as the superposition

$$E(t) = E_1(t) + E_2(t) = \left(\tilde{E}_1 \mathrm{e}^{i(\phi_1+\varphi)-i(\omega_0-\Delta\omega)t} + \tilde{E}_2 \mathrm{e}^{i\phi_2-i(\omega_0+\Delta\omega)t}\right) + c.c., \quad (6.2)$$

where ϕ_1 and ϕ_2 are two phases whose difference $\Delta\phi = \phi_2 - \phi_1$, we wish to determine, and φ is a controllable phase imparted on the first tone. The two field components may be partly superimposed by sending them through a Mach-Zehnder modulator (MZM) driven at an RF of Δf. This results in the generation of two optical combs (one from each tone), which interfere with one another. The optical power at the center angular frequency ω_0 is now given by

$$P_\varphi = K\left|\eta_1 \tilde{E}_1 \mathrm{e}^{i(\phi_1+\varphi)-i\omega_0 t} + \eta_2 \tilde{E}_2 \mathrm{e}^{i\phi_2 - i\omega_0 t}\right|^2, \quad (6.3)$$

where K is an unimportant conversion constant, and η_1 and η_2 are the fractions of the original two field components that are converted to the comb line at ω_0. Consider now the power for the particular values $\varphi = \{0, \pi/2, \pi, 3\pi/2\}$ [156]

$$P_{\varphi=0} = K^2\left(|\eta_1\tilde{E}_1|^2 + |\eta_2\tilde{E}_2|^2 + 2\eta_1\eta_2\tilde{E}_1\tilde{E}_2\cos\left[\phi_2-\phi_1\right]\right), \quad (6.4a)$$

$$P_{\varphi=\pi/2} = K^2\left(|\eta_1\tilde{E}_1|^2 + |\eta_2\tilde{E}_2|^2 + 2\eta_1\eta_2\tilde{E}_1\tilde{E}_2\sin\left[\phi_2-\phi_1\right]\right), \quad (6.4b)$$

$$P_{\varphi=\pi} = K^2\left(|\eta_1\tilde{E}_1|^2 + |\eta_2\tilde{E}_2|^2 - 2\eta_1\eta_2\tilde{E}_1\tilde{E}_2\cos\left[\phi_2-\phi_1\right]\right), \quad (6.4c)$$

$$P_{\varphi=3\pi/2} = K^2\left(|\eta_1\tilde{E}_1|^2 + |\eta_2\tilde{E}_2|^2 - 2\eta_1\eta_2\tilde{E}_1\tilde{E}_2\sin\left[\phi_2-\phi_1\right]\right), \quad (6.4d)$$

which can be seen only to deviate through the interference term involving the phase difference $\phi_2 - \phi_1$. By combining Eqs. (6.4d) one finds

$$\Delta\phi = \phi_2 - \phi_1 = \arctan\left(\frac{P_{\varphi=\pi/2} - P_{\varphi=3\pi/2}}{P_{\varphi=0} - P_{\varphi=\pi}}\right). \quad (6.5)$$

This result suggests, that using a time-sequential measurement in which four distinct phases are applied to one of the tones, it is possible to reconstruct the phase difference between the two tones (up to an integer m of 2π).

Assume now that two tones have propagated through dispersive media or waveguides, and have thereby accumulated the phase difference

$$\Delta\Phi = \left[\tilde{\beta}(\omega_2) - \tilde{\beta}(\omega_1)\right] l, \quad (6.6)$$

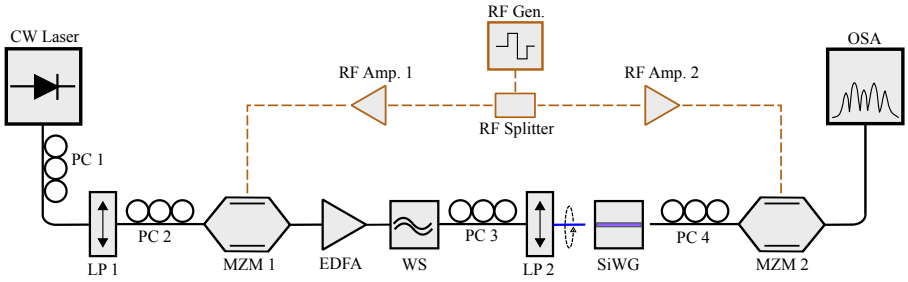

Figure 6.9: Dispersion measurement setup. PC: Polarization controller; LP: Linear polarizer, MZM: Mach-Zehnder modulator; EDFA: Erbium-doped fiber amplifier; WS: Waveshaper; SiWG: Silicon waveguide; OSA: Optical spectrum analyser; RF: Radio frequency. A PM fiber and a PM lensed fiber (blue) is used for coupling light into the waveguide in a known calibrated polarization. The in-coupling stage employs a rotatable fiber mount for the PM lensed fiber facilitating easy alteration between TE-polarized and TM-polarized input.

where l is the propagation length, and we have defined effective (average) wavenumbers $\tilde{\beta}$, which encompass the effect of a potential z-dependence through different optical waveguides and components. By combining Eqs. (6.5) and (6.6), one finds that the measured phase difference $\Delta\phi = \Delta\Phi - 2m\pi$. From this, a first-order approximation of the inverse group velocity can be deduced:

$$\frac{\Delta\phi}{(\omega_2-\omega_1)l} = \frac{\tilde{\beta}(\omega_2)-\tilde{\beta}(\omega_1)}{\omega_2-\omega_1} - \frac{2m\pi}{(\omega_2-\omega_1)l} \approx \frac{\mathrm{d}\tilde{\beta}}{\mathrm{d}\omega}\Big|_{\omega=\omega_0} - \frac{2m\pi}{\Delta\omega l}. \tag{6.7}$$

It follows, that by measuring $\Delta\phi$ for the TE- and TM-polarization modes, one may estimate the relative inverse group velocity $\Delta\beta_1(\omega_0)$, and furthermore, by extending the measurement to a range of center wavelengths, one may even extract the GVD parameter $\beta_2(\omega)$ or the dispersion parameter D.

The measurement setup is sketched in Fig. 6.9. A tunable CW laser (either Tunics Plus or IDPhotonics CoBrite) provides the optical signal, which is directed into the first MZM (MZM 1). The MZM is driven at an RF of $f_{\mathrm{MZM}} = 25$ GHz, generating an optical comb structure with this frequency spacing. By controlling the bias of the MZM, the original laser line is suppressed with respect to the two first-order modulation peaks at $f_0 - f_{\mathrm{MZM}}$ and $f_0 + f_{\mathrm{MZM}}$, which form the two optical tones discussed above. A low-threshold, low-gain erbium-doped fiber amplifier (EDFA) amplifies the two tones to an output power of 10 dBm. A programmable optical filter (Finisar, Waveshaper 4000s) imparts the controlled phase φ on the low-frequency tone (or the high-frequency tone), while at the same time further attenuating the center peak (> 40 dB). The two tones now co-propagate through an additional PC and into a LP setting a polarization reference. A PM fiber leads to the in-coupling stage, which consists of a rotatable fiber holder (with angle meter) facilitating easy alteration between TE- and TM input. The TE-input angle is calibrated using a crystalline silicon photonic crystal waveguide

featuring a TE-bandgap above 1568 nm, while the TM mode is launched by a rotation of 90° with respect to the TE angle. Finally, the output-coupled light is sent to a second MZM operated by an RF signal that originates from the same RF signal generation as that driving the first MZM. The 25-GHz modulation causes the two tones to interfere and the power of the center tone (original laser frequency) is measured by an OSA for the four different values of φ.

Our setup has an optical measurement bandwidth set by the EDFA of 1530 nm - 1565 nm, although this could potentially be extended by substitution with a C+L-band amplifier. Within this wavelength range, data acquisition is fully automated.

6.5.2 Optical fiber: known test device

The implemented setup is first tested for a 250-m long highly-nonlinear fiber (HNLF) optical fiber (OFS, HNLF Spline), which has a reference dispersion profile provided by the manufacturer. The used measurement setup was similar to that sketched in Fig. 6.9 but with the HNLF substituted for the coupling stages and the silicon chip. Figure 6.10 shows $\Delta\Phi(\lambda)$ for (a) the background measurement performed by bypassing the HNLF, and (b) the measurements including the HNLF. The effective differential phase accumulated in the HNLF is given by the difference $\Delta\Phi_{\text{Fiber}} = \Delta\Phi_{\text{Tot}} - \Delta\Phi_{\text{Ref}}$ and is shown in Fig. 6.10(c). Finally, the resulting dispersion parameter, $D(\lambda) = \frac{d}{d\lambda}(\frac{d\beta}{d\omega})$ is shown in Fig. 6.10(d) alongside the dispersion parameter provided by the fiber manufacturer (red line). Fine agreement is observed between the two measurement techniques within the tuning range allowed by our setup, justifying that we proceed with the integrated waveguides.

6.5.3 Waveguide measurements

Finally, the measurement setup in Fig. 6.9 was used to analyse some of our a-Si:H waveguide samples. An important parameter for these square-like waveguides is their relative group index $\Delta n_{\text{g}} = c\Delta\beta_1$. Figure 6.11 shows the experimentally obtained relative values of the TE- and TM group indices for six different waveguides. The top, middle, and bottom row represent the 390-nm wide, 404-nm wide, and 416-nm wide, waveguides respectively, while the left- and right column represent waveguide lengths of 7.7 mm and 11.7 mm, respectively. First, consider the waveguides of width $w \approx 390$ nm in (a) and (b). The measured group index for the TM mode can be observed to be slightly larger ($\Delta n_{\text{g}} \approx 0.05$) than that measured for the TE mode, but the data for both modes is rather noisy. This 'noise', however, was reproducible, and is therefore likely caused by some unwanted effect such as mode coupling. A particularly big fluctuation is seen for the TE mode at $\lambda = (1545 - 1550)$ nm, which coincides with the spectral dip for the 390-nm wide waveguide, see Fig. 6.7. These noisy features rendered it impossible to estimate the waveguide dispersion for the two polarization modes. Moreover, proceeding to the waveguides of width $w \approx 404$ nm in (c) and (d), this effect only worsened. By

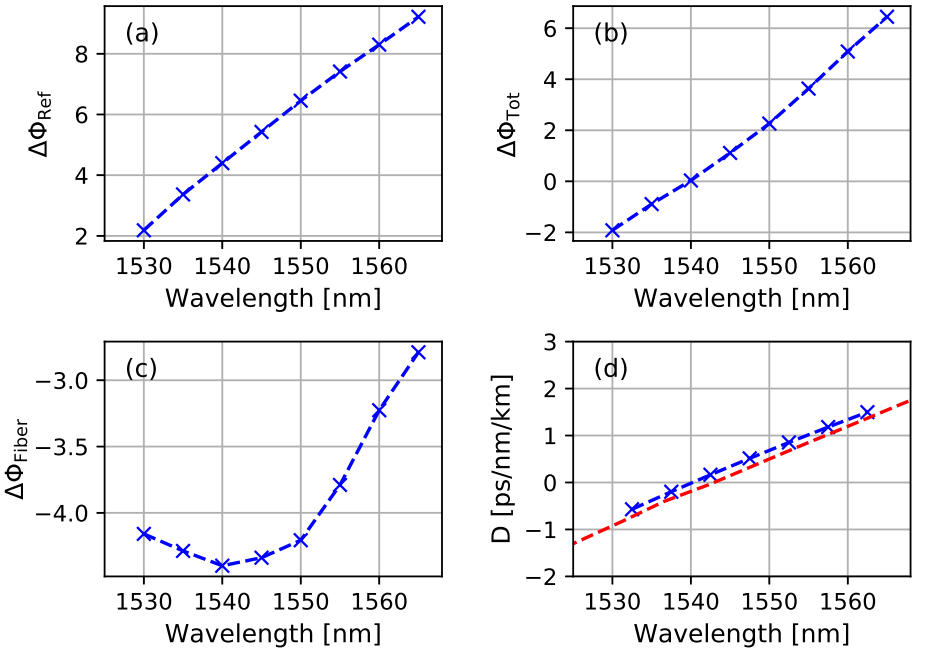

Figure 6.10: (a) Reference, (b) total, and (c) resulting differential phase for a 250-m long HNLF fiber. (d) A fit of the dispersion parameter D shown along with data provided by manufacturer OFS. Our measurement reproduces the ZDW provided by the manufacturer to within 2 nm.

design, the 404-nm wide waveguides exhibit the smallest degree of birefringence, which rendered them more susceptible to polarization-mode coupling. Finally, consider the waveguides of width $w \approx 390$ nm in (e) and (f), which exhibit a group birefringence of $\Delta n_g \approx 0.1$ with $n_g^{(TM)} > n_g^{(TE)}$. In comparison with the narrower 390-nm wide waveguides, we observe that the differential group index $\Delta n_g = n_g^{(TM)} - n_g^{(TE)}$ increases as we move to a broader waveguide. This tendency is in agreement with expectations. On the other hand, we did not anticipate for the 390-nm wide waveguides that $n_g^{(TM)} > n_g^{(TE)}$ as experimentally observed.

Note that Fig. 6.11 shows the results for the TE mode and the TM mode relative to each other on a common y-axis. Doing so relies on the assumption that the same value of the integer m in Eq. (6.7) applies to the measurement of the two polarization modes. Indeed this assumption seems realistic in our case as a an additional factor of 2π would result in a group index change, see Eq. (6.7), of $c/(\Delta f l) \approx 0.8$ for the short 7.7 mm waveguide. As we expect the two waveguide polarization modes to behave very similarly, such a large polarization-mode group-index difference seems very unlikely. Note that this approach of "stitching" the results for the two polarization modes to enable a comparison of their relative group indices would not be viable for longer waveguides.

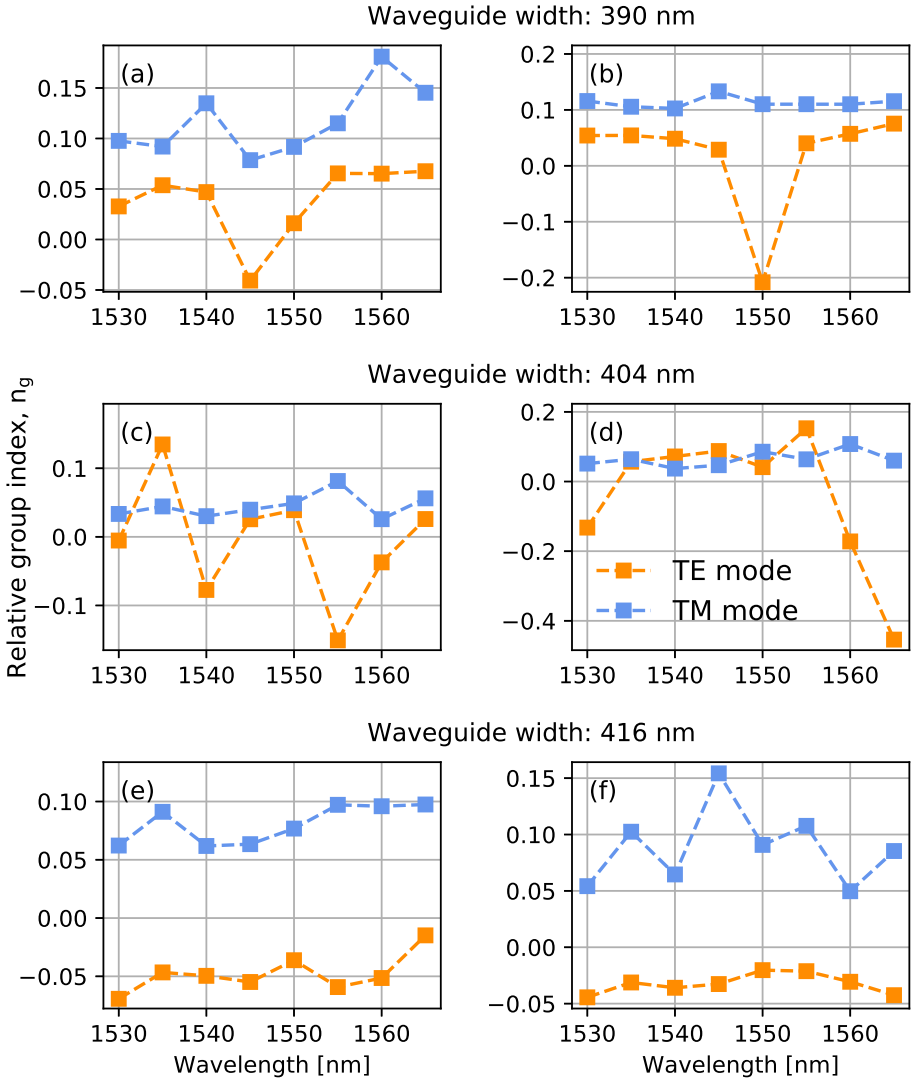

Figure 6.11: Relative group indices n_g measured for both the TE- (orange) and the TM (blue) polarization modes, for the (a), (c), and (e) 7.7-mm long waveguides, and (b), (d), and (f) 11.7 mm waveguides.

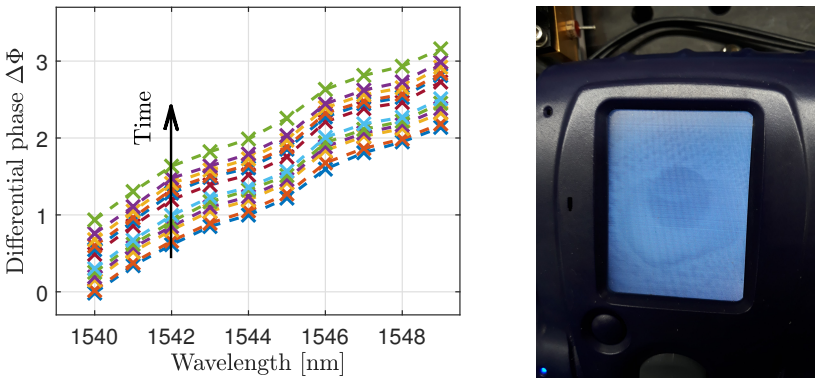

(a) (b)

Figure 6.12: (a) 12 datasets illustrating how the differential-phase measurements drift in time over the course of a morning (∼4 hours). (b) Illustration of water condensation on a fiber facet, courtesy of P. D. Girouard.

6.5.4 Discussion of error sources

Further characterization of our waveguide samples was unfortunately hindered due to time restrictions on availability of certain pieces of equipment. Therefore it was not possible to run the measurements with a finer wavelength resolution, nor was it possible to repeat the experiments multiple times for gathering statistics. This said, it was clear from working with the setup that various sources of errors were playing a non trivial role.

Firstly, we observed a drift in the recorded phase over time, see Fig. 6.12(a). While the cause of this drift is not completely pinned down, it is expected to be a result of water molecules condensing (and evaporating) inside the fiber connectors as seen in Fig. 6.12(b). The setup was located in a transparent laboratory, which permitted solar radiation to influence the temperature and humidity of the local environment. The effect of this was only worsened by the fact that the experiment was carried out during peak Summer time. The systematic error was accompanied by small random fluctuations estimated to $(0.01 - 0.04)$ rad depending on the time of day. We likewise expect a significant portion of these fluctuations to result from the water condensation. This is supported by the observation that the fluctuations largely disappeared, temporarily, after cleaning all fiber facets and connectors.

The measurements in Fig. 6.11 were performed during evening- and early-night hours, at which point the measurement setup demonstrated a much larger degree of stability than during day hours. However, despite of this, it would have been more optimal to perform the experiment in a temperature- and humidity controlled basement laboratory.

6.6 Discussion and Summary

We have designed and characterized hydrogenated amorphous silicon waveguides of an unconventional square-like geometries of $h \times w \approx 400 \times (400 \pm \delta)$ nm^2. In such waveguides, the fundamental TE- and TM modes are characterized by similar propagation constants and dispersion properties, but the elongation of the waveguide cross section introduces a birefringence in a similar manner to an elliptical-core optical fiber.

The purpose of the designed waveguides, was to realize, for the first time on an integrated platform, the type-II cross-polarized FWM interaction. Unfortunately, and this was not due to lack of searching for it, no such demonstration was realized. This can likely be attributed to a mix of the three following issues: (i) Our waveguide samples were prone to mode coupling, which was evident from relative noisy transmission measurements. Such coupling could strongly influence the phase-matching condition of the type-II FWM process. (ii) The considered nonlinear process is narrowband (although it can be tailored to be broadband [157]), which makes it difficult to localize. For example, the 7.7 mm waveguide is estimated to have a 3-dB bandwidth of 2 nm. However, the amorphous waveguide inevitably features long-range core-size fluctuations on the order of $\sim$ 2-3 nm, which will result in a broadened bandwidth but a decreased peak efficiency. This final point could be crucially important as the desired process already features a $\sim$ 10 dB conversion penalty with respect to the co-polarized FWM process. (iii) A clear degradation of the hydrogenated amorphous silicon (at least 6 dB of insertion loss) was observed in the course of a few hours when the material was pumped with a CW input power of $\sim$ 14 dBm. This degradation strongly worked against us, given that we had to sweep the signal-pump detuning to attempt to localize the interaction. Each sweep (of 50 nm) took approximately an hour, during which the tested waveguide had already undergone significant degradation. The degradation can, in a future trial, be avoided by using another platform such as silicon nitride or by altering the passivation process of the dangling bonds so to use deuterium rather than hydrogen [158]. This could simultaneously diminish the effect of nonlinear absorption [158].

We further characterized the hydrogenated amorphous silicon samples through (linear) loss measurements. As expected, the employed interconnection mechanism using inverted waveguide tapers, resulted in a generally lower insertion loss for TE-polarized light. On the other hand, the "cut-back" analysis indicated that the TM mode experienced a slightly lower propagation loss, likely attributed to the TE mode being more affected by scattering induced by sidewall roughness. By furthermore investigating the wavelength-dependent loss we observed a surprising feature: each waveguide exhibited a transmission dip in a spectral region of $\sim$ 5 nm, the position of which seemed to depend on both the waveguide width and the polarization mode. The origin of this peculiar "chip-n-dip"-effect is an ongoing investigation.

Finally, some of the waveguide samples were characterized by a setup build for dispersion measurements. However, presumably due to various coupling mechanisms, which rendered the results "noisy", it was not realistic to extract the dispersion parameters for the fundamental polarization modes. Instead, we used the measurement setup to estimate the relative group index of the two polarization modes.

Part V

Final remarks

CHAPTER 7

Conclusion

In this thesis we have, mainly on a theoretical level, considered and tailored four-wave-mixing processes for applications within quantum information science.

7.1 Tailored photon-pair generation

First, we proposed two very different schemes for the generation of spectral-temporal uncorrelated photon pairs through spontaneous four-wave mixing:

The first proposal, in Chapter 3, relied on an interaction between two orthogonally polarized pulsed pumps in a birefringent waveguide. The modal birefringence enabled a relative walk-off between the two pulses, which gave rise to a gradually varying nonlinear interaction strength. The generated signal and idler photons emerge in orthogonal polarizations, and were found to be temporal copies of the two pump pulses. Thus, temporal shaping of the two photons could be realized merely by controlling the temporal pulse forms of the interacting pumps. Further, our developed time-domain approach in the Heisenberg picture allowed assessment of the influence of nonlinear phase modulation on the photon-pair quantum state. It was here found that, even for high generation rates, the proposed configuration was extremely robust against the otherwise deleterious effect of nonlinear phase modulation.

Proposal number two, outlined in Chapter 4, considered spontaneous four-wave mixing inside a resonator structure. The resonator enhances the optical density of states at certain (resonator) wavelengths, which facilitates efficient photon-pair generation at particular well-defined frequency modes. We demonstrated, that by carefully tailoring the pulse used to pump a standard microring resonator, we

could entirely eliminate spectral correlation between generated signal- and idler photons. We showed that the optimal pump-pulse spectrum for achieving this, was well approximated by a dual-pulse spectrum in which the two pulse components were π out of phase and properly separated in time.

7.2 Shape-preserving Bragg scattering

Next, we considered four-wave mixing Bragg scattering driven by two orthogonally polarized pumps in a birefringent waveguide. It was shown that this version of Bragg scattering, due to its underlying phase-matching mechanism, allowed for entirely uni-directional frequency conversion as undesired Bragg scattering processes were suppressed by the waveguide birefringence. Further, we found that the process featured a large conversion bandwidth, which, contrary for the standard co-linear Bragg scattering process, was not limited by the size of the frequency translation. Finally, it was demonstrated that the considered process preserved the temporal shape of the signal upon frequency conversion, an important and desirable feature in optical (quantum) communication systems.

7.3 Experimental efforts with amorphous silicon

All of the three theoretical proposals are envisioned to be implementable on a nonlinear photonic chip. In the final part of the thesis, in Chapter 6, we took the first steps towards demonstrating the two proposals based on birefringent waveguides from Chapters 3 and 5. We simulated and designed a range of hydrogenated amorphous silicon-on-insulator waveguides of varying waveguide widths, which were fabricated in-house using electron-beam lithography. Upon fabrication, we characterized the waveguide samples in terms of their polarization-dependent optical loss and relative modal group indices. The transmission spectra illuminated a surprising issue with the waveguide samples: each waveguide featured a significant spectral dip, likely due to resonant mode coupling. This effect, however, altered the dispersive property of the waveguides, which, alongside the light-induced material degradation, significantly complicated our search for the cross-polarized four-wave mixing interaction. More work is therefore necessary in order to demonstrate the desired interaction in an on-chip integrated waveguide, and to understand exactly what effect caused the peculiar spectral features.

7.4 Outlook and future work

On-chip integrated sources of pure-state single photons constitute a key ingredient for the development and up-scaling of quantum photonics technologies. In this thesis, we suggested two different heralded schemes for realizing such sources, and

a rather obvious future goal is to pursue experimental demonstrations of these two schemes in an integrated scenario.

An experimental demonstration of the microring-resonator scheme presented in Chapter 4 seems like the least complicated of the two. In this case, the microring resonator sources already exist (a silicon microring resonator with a quality factor of 40,000 is a realistic candidate), and they must "simply" be pumped by a reshaped pump pulse created e.g. using a waveshaper. A more ambitious approach would be to attempt to reshape the pump pulse on the photonic chip using integrated thermally controlled Mach-Zehnder interferometers. This, naturally, requires detailed design considerations, and likely mitigation of photons generated prior to the microring.

With respect to the configuration based on a birefringent waveguide described in Chapter 3 (and also the Bragg scattering configuration in Chapter 5), there are still open questions. For example, is silicon the natural platform for the scheme? It would be attractive to look towards other material platforms than silicon. In particular, lower index materials such as silicon (rich) nitride or hydex would potentially enable the desired birefringence but without the presence of higher-order guided modes. This possibility is interesting also since it would ease the challenge of simultaneously coupling light on and off chip in both polarization modes simultaneously. Yet, silicon is still attractive as it provides an ultra high nonlinearity, thereby limiting power requirements. Alternatively, a proof-of-concept experiment could be performed in a polarization maintaining optical fiber, although Raman scattering, in this case, would be a significant source of noise photons.

From a theoretical perspective, there also remains a lot of work to be done. The microring resonators are an attractive option for pair generation, and their dynamics are rich, making them interesting to study. More detailed theoretical work is necessary to come up with more optimal designs and coupling schemes such as in [107, 108]. Besides, it would be interesting to investigate the performance of a hybridization between our dual-pulse proposal and the multi-point coupling schemes [107].

With respect to the schemes based on a birefringent waveguide, there are also theoretical work yet to be performed. In particular, the interplay between dispersive and nonlinear phase-modulation effects has to investigated. This could be done on the basis of a split-step Fourier method for the biphoton amplitude, which we have recently developed [159].

Part VI

Appendices

APPENDIX A

The joint amplitude in time and frequency

The biphoton wavefunction is commonly expressed as

$$|\Psi_{\mathrm{II}}\rangle = \iint \mathrm{d}\omega_{\mathrm{i}}\mathrm{d}\omega_{\mathrm{s}}\mathcal{A}(\omega_{\mathrm{i}},\omega_{\mathrm{s}})\hat{a}_{\mathrm{i}}^{\dagger}(\omega_{\mathrm{i}})\hat{a}_{\mathrm{s}}^{\dagger}(\omega_{\mathrm{s}})\,|0_{\mathrm{i}},0_{\mathrm{s}}\rangle\,, \tag{A.1}$$

where $\hat{a}_{\mathrm{i}}^{\dagger}(\omega_{\mathrm{i}})$ and $\hat{a}_{\mathrm{s}}^{\dagger}(\omega_{\mathrm{s}})$ generates a signal- and idler photon at frequencies ω_{i} and ω_{s}, respectively, and $|0_{\mathrm{i}},0_{\mathrm{s}}\rangle$ is the two-mode vacuum state. Moreover, $\mathcal{A}(\omega_{\mathrm{i}},\omega_{\mathrm{s}})$ is the joint spectral amplitude containing the spectral characteristics of the photon pair. Introducing the Fourier relationship,

$$\hat{a}_j(\omega) = (2\pi)^{-1/2}\int \mathrm{d}t\ \hat{a}_j(t)\mathrm{e}^{-i\omega t}, \tag{A.2}$$

where $\hat{a}_j^{\dagger}(t)$ generates a photon in mode j at time t, we may reformulate Eq. (A.1):

$$\begin{aligned}
|\Psi_{\mathrm{II}}\rangle &= (2\pi)^{-1}\iint \mathrm{d}\omega_{\mathrm{i}}\mathrm{d}\omega_{\mathrm{s}}\mathcal{A}(\omega_{\mathrm{i}},\omega_{\mathrm{s}})\iint \mathrm{d}t_{\mathrm{i}}\mathrm{d}t_{\mathrm{s}}\hat{a}_i^{\dagger}(t_{\mathrm{i}})\hat{a}_s^{\dagger}(t_{\mathrm{s}})\mathrm{e}^{i(\omega_{\mathrm{i}}t_{\mathrm{i}}+\omega_{\mathrm{s}}t_{\mathrm{s}})}\,|0_{\mathrm{i}},0_{\mathrm{s}}\rangle \\
&= \iint \mathrm{d}t_{\mathrm{i}}\mathrm{d}t_{\mathrm{s}}\,(2\pi)^{-1}\iint \mathrm{d}\omega_{\mathrm{i}}\mathrm{d}\omega_{\mathrm{s}}\mathcal{A}(\omega_{\mathrm{i}},\omega_{\mathrm{s}})\mathrm{e}^{i(\omega_{\mathrm{i}}t_{\mathrm{i}}+\omega_{\mathrm{s}}t_{\mathrm{s}})}\hat{a}_i^{\dagger}(t_{\mathrm{i}})\hat{a}_s^{\dagger}(t_{\mathrm{s}})\,|0_{\mathrm{i}},0_{\mathrm{s}}\rangle \\
&= \iint \mathrm{d}t_{\mathrm{i}}\mathrm{d}t_{\mathrm{s}}\mathcal{A}(t_{\mathrm{i}},t_{\mathrm{s}})\hat{a}_i^{\dagger}(t_{\mathrm{i}})\hat{a}_s^{\dagger}(t_{\mathrm{s}})\,|0_{\mathrm{i}},0_{\mathrm{s}}\rangle\,,
\end{aligned} \tag{A.3}$$

where we have identified the JTA, $\mathcal{A}(t_{\mathrm{i}},t_{\mathrm{s}})$, which has a 2-D Fourier relation with the JSA according to:

$$\mathcal{A}(t_{\mathrm{i}},t_{\mathrm{s}}) = (2\pi)^{-1}\iint \mathrm{d}\omega_{\mathrm{i}}\mathrm{d}\omega_{\mathrm{s}}\mathcal{A}(\omega_{\mathrm{i}},\omega_{\mathrm{s}})\mathrm{e}^{i(\omega_{\mathrm{i}}t_{\mathrm{i}}+\omega_{\mathrm{s}}t_{\mathrm{s}})}. \tag{A.4}$$

APPENDIX B

Hong-Ou-Mandel interference of spectrally mixed photons

We here provide the derivation[1] of Eq. (2.46) which describes the quantum-interference coincidence probability on a 50-50 BS for an input given as two photons described by arbitrary density operators. To this end, consider a photon in input mode 1, described by the density operator $\hat{\rho}_1$, and a photon in input mode 2, described by the density operator $\hat{\rho}_2$. The density operator describing the composite system is then $\hat{\rho}^{\text{in}} = \hat{\rho}_1 \otimes \hat{\rho}_2$, or explicitly

$$\hat{\rho}^{\text{in}} = \sum_{k_1} \lambda_{k_1}^2 \hat{A}_{1,k_1}^\dagger \left|0\right\rangle \left\langle 0\right| \hat{A}_{1,k_1} \otimes \sum_{k_2} \mu_{k_2}^2 \hat{B}_{2,k_2}^\dagger \left|0\right\rangle \left\langle 0\right| \hat{B}_{2,k_2}, \tag{B.1}$$

where $\hat{A}_{1,k}^\dagger = \int \mathrm{d}\omega\ \psi_{a,k}(\omega)\hat{a}_1^\dagger(\omega)$ and $\hat{B}_{2,k}^\dagger = \int \mathrm{d}\omega\ \psi_{b,k}(\omega)\hat{a}_2^\dagger(\omega)$ are broadband mode operators as defined in Eq. (2.37). We assume that the BS is non-dispersive, so that the broadband mode operators are transformed in the same way as the discrete mode operators in Eq. (2.42). Hence, after the BS, the density operator describing the two photons is given as

$$\begin{aligned}\hat{\rho}^{\text{out}} = \frac{1}{4} \sum_{k_1} \lambda_{k_1}^2 \left(\hat{A}_{1,k_1}^\dagger + i\hat{A}_{2,k_1}^\dagger\right) \left|0\right\rangle \left\langle 0\right| \left(\hat{A}_{1,k_1} - i\hat{A}_{2,k_1}\right) \\ \otimes \sum_{k_2} \mu_{k_2}^2 \left(\hat{B}_{2,k_2}^\dagger + i\hat{B}_{1,k_2}^\dagger\right) \left|0\right\rangle \left\langle 0\right| \left(\hat{B}_{2,k_2} - i\hat{B}_{1,k_2}\right),\end{aligned} \tag{B.2}$$

[1] This derivation was done in collaboration with Prof. C. McKinstrie, and later refined based on work in [46]

or in the shorter form [46]

$$\hat{\rho}^{\text{out}} = \sum_{k_1,k_2} \lambda_{k_1}^2 \mu_{k_2}^2 \left|\psi_{k_1,k_2}^{\text{out}}\right\rangle \left\langle\psi_{k_1,k_2}^{\text{out}}\right|, \tag{B.3}$$

where

$$\left|\psi_{k_1,k_2}^{\text{out}}\right\rangle = \frac{1}{2}\left(\hat{A}_{1,k_1}^\dagger + i\hat{A}_{2,k_1}^\dagger\right)\left(\hat{B}_{2,k_2}^\dagger + i\hat{B}_{1,k_2}^\dagger\right). \tag{B.4}$$

To calculate the probability of getting a coincidence detection, P_{12}, we need the projection operators, $\hat{P}_1$ and $\hat{P}_2$: [160]

$$\begin{aligned}
\hat{P}_j &= \int \mathrm{d}\omega\ \hat{a}_j^\dagger(\omega)\left|0\right\rangle\left\langle 0\right|\hat{a}_j(\omega) \\
&= \int \mathrm{d}\omega\ \hat{a}_j^\dagger(\omega)\left|0\right\rangle \int \mathrm{d}\omega' \delta(\omega-\omega')\left\langle 0\right|\hat{a}_j(\omega') \\
&= \int \mathrm{d}\omega\ \hat{a}_j^\dagger(\omega)\left|0\right\rangle \int \mathrm{d}\omega' \sum_k \psi_{a,k}(\omega)\psi_{a,k}^*(\omega')\left\langle 0\right|\hat{a}_j(\omega') \\
&= \sum_k \int \mathrm{d}\omega\ \psi_{a,k}(\omega)\hat{a}_j^\dagger(\omega)\left|0\right\rangle \int \mathrm{d}\omega'\left\langle 0\right|\psi_{a,k}^*(\omega')\hat{a}_j(\omega') \\
&= \sum_k \hat{A}_{j,k}^\dagger\left|0\right\rangle\left\langle 0\right|\hat{A}_{j,k} = \sum_k \hat{B}_{j,k}^\dagger\left|0\right\rangle\left\langle 0\right|\hat{B}_{j,k},
\end{aligned} \tag{B.5}$$

where we have first inserted unity, and then used the completeness relation, in order to express the projection operators in the basis of broadband mode operators. The probability P_{12} is given as the trace

$$P_{12} = \mathrm{Tr}\left[\rho^{\text{out}}\hat{P}_1\hat{P}_2\right] = \sum_{k_1,k_2} \lambda_{k_1}^2\mu_{k_2}^2 \left\langle\psi_{k_1,k_2}^{\text{out}}\right|\hat{P}_1\hat{P}_2\left|\psi_{k_1,k_2}^{\text{out}}\right\rangle \tag{B.6}$$

In inserting into Eq. (B.6), terms involving either zero or two photons in either path drop out, leaving us with:

$$P_{12} = \frac{1}{4}\sum_{k_1,k_2} \lambda_{k_1}^2\mu_{k_2}^2 \left\langle 0,0\right|\left(\hat{A}_{1,k_1}\hat{B}_{2,k_2} - \hat{A}_{2,k_1}\hat{B}_{1,k_2}\right)\hat{P}_1\hat{P}_2\left(\hat{A}_{1,k_1}^\dagger\hat{B}_{2,k_2}^\dagger - \hat{A}_{2,k_1}^\dagger\hat{B}_{1,k_2}^\dagger\right)\left|0,0\right\rangle, \tag{B.7}$$

Calculating first the non-interfering terms, noting that for a normalized input $\sum_k \lambda_k^2 = \sum_k \mu_k^2 = 1$, we find

$$\begin{aligned}
P_{12} = \frac{1}{2} - \frac{1}{4}\sum_{k_1,k_2} \lambda_{k_1}^2\mu_{k_2}^2 \Big[&\left\langle 0,0\right|\hat{A}_{1,k_1}\hat{B}_{2,k_2}\hat{P}_1\hat{P}_2\hat{A}_{2,k_1}^\dagger\hat{B}_{1,k_2}^\dagger\left|0,0\right\rangle \\
&+ \left\langle 0,0\right|\hat{A}_{2,k_1}\hat{B}_{1,k_2}\hat{P}_1\hat{P}_2\hat{A}_{1,k_1}^\dagger\hat{B}_{2,k_2}^\dagger\left|0,0\right\rangle\Big],
\end{aligned} \tag{B.8}$$

By now returning to continuous mode operators, we find the final expression

$$P_{12} = \frac{1}{2} - \frac{1}{4} \sum_{k_1,k_2} \lambda_{k_1}^2 \mu_{k_2}^2 \int \mathrm{d}\omega_1 \psi_{a,k_1}^*(\omega_1) \psi_{b,k_2}(\omega_1) \int \mathrm{d}\omega_2 \psi_{b,k_2}^*(\omega_2) \psi_{a,k_1}(\omega_2), \tag{B.9}$$

which is identical to Eq. (2.46).

APPENDIX C

Photon generation in the Heisenberg picture

In Eq. (2.28) of the main text we, for simplicity, neglected a time-ordering operator, which in a rigorous treatment must be included as the Hamiltonian in Eq. (2.27) in general does not commute with itself at different points in time. The more general unitary operator thus takes the form

$$\hat{U} = \mathcal{T} \exp\left[-\frac{i}{\hbar}\int_{t_1}^{t_2} \hat{H}_{\text{eff}}(t)\right], \tag{C.1}$$

where $\mathcal{T}$ is the time-ordering operator [40, 39], which significantly complicates the evolution and only allows for analytical solutions in exceptional cases [86]. Instead, in order to solve the problem of state-evolution, one must often resort to various approximations such as the Dyson series [36, 38] or the Magnus expansion [39]. However, even with the time-ordering operator included, the bilinearity of the Hamiltonian entails that the evolution has a very specific structure. Specifically, in the Heisenberg picture of motion, the general solution takes the form of a linear Bogoliubov transformation:

$$\hat{b}_{\text{i}}(\omega) = \int \mathrm{d}\omega' \left[G_{\text{ii}}(\omega,\omega')\hat{a}_{\text{i}}(\omega') + G_{\text{is}}(\omega,\omega')\hat{a}_{\text{s}}^{\dagger}(\omega')\right], \tag{C.2}$$

$$\hat{b}_{\text{s}}(\omega) = \int \mathrm{d}\omega' \left[G_{\text{ss}}(\omega,\omega')\hat{a}_{\text{s}}(\omega') + G_{\text{si}}(\omega,\omega')\hat{a}_{\text{i}}^{\dagger}(\omega')\right], \tag{C.3}$$

in which G_{jk} are transfer function, which, as a set, form a unitary transformation, and $\hat{a}_j$ and $\hat{b}_j$ are input and output operators, respectively. We note that similar relations exist in the time domain, as used explicitly in Chapter 3.

As the input operators $\hat{a}_j$, the output operators must obey the usual Bosonic commutator relations:

$$\left[\hat{b}_j(\omega), \hat{b}_k(\omega')\right] = 0, \qquad \left[\hat{b}_j(\omega), \hat{b}_k^\dagger(\omega')\right] = \delta_{jk}\delta(\omega - \omega'). \tag{C.4}$$

These commutators result in constraints on the transfer functions in Eq. (C.2) and Eq. (C.3), such as

$$\left[\hat{b}_\mathrm{i}(\omega_\mathrm{i}), \hat{b}_\mathrm{i}^\dagger(\omega_\mathrm{i}')\right] = \int \mathrm{d}\omega \left[G_\mathrm{ii}(\omega_\mathrm{i}, \omega) G_\mathrm{ii}^*(\omega_\mathrm{i}', \omega) - G_\mathrm{is}(\omega_\mathrm{i}, \omega) G_\mathrm{is}^*(\omega_\mathrm{i}', \omega)\right] = \delta(\omega_\mathrm{i} - \omega_\mathrm{i}'), \tag{C.5}$$

$$\left[\hat{b}_\mathrm{s}(\omega_\mathrm{s}), \hat{b}_\mathrm{s}^\dagger(\omega_\mathrm{s}')\right] = \int \mathrm{d}\omega \left[G_\mathrm{ss}(\omega_\mathrm{s}, \omega) G_\mathrm{ss}^*(\omega_\mathrm{s}', \omega) - G_\mathrm{si}(\omega_\mathrm{s}, \omega) G_\mathrm{si}^*(\omega_\mathrm{s}', \omega)\right] = \delta(\omega_\mathrm{s} - \omega_\mathrm{s}'), \tag{C.6}$$

and

$$\left[\hat{b}_\mathrm{i}(\omega_\mathrm{i}), \hat{b}_\mathrm{s}(\omega_\mathrm{s})\right] = \int \mathrm{d}\omega \left[G_\mathrm{ii}(\omega_\mathrm{i}, \omega) G_\mathrm{si}(\omega_\mathrm{s}, \omega) - G_\mathrm{is}(\omega_\mathrm{i}, \omega) G_\mathrm{ss}(\omega_\mathrm{s}, \omega)\right] = 0. \tag{C.7}$$

Similar to the forward transformations in Eqs. (C.2) and Eq. (C.3), we have the backward transformations

$$\hat{a}_\mathrm{i}(\omega') = \int \mathrm{d}\omega \left[H_\mathrm{ii}(\omega', \omega)\hat{b}_\mathrm{i}(\omega) + H_\mathrm{is}(\omega', \omega)\hat{b}_\mathrm{s}^\dagger(\omega)\right], \tag{C.8}$$

$$\hat{a}_\mathrm{s}(\omega') = \int \mathrm{d}\omega \left[H_\mathrm{ss}(\omega', \omega)\hat{b}_\mathrm{s}(\omega) + H_\mathrm{si}(\omega', \omega)\hat{b}_\mathrm{i}^\dagger(\omega)\right]. \tag{C.9}$$

The backward transformation transfer functions H_{jk} are related to the forward transformation transfer functions G_{jk}, a relation which is used in Appendix D. To find this relation, we combine Eqs. (C.2), (C.3), (C.8), and (C.9), to achieve

$$\begin{aligned}
\hat{b}_\mathrm{i}(\omega) &= \int \mathrm{d}\omega' \left[G_\mathrm{ii}(\omega, \omega')\hat{a}_\mathrm{i}(\omega') + G_\mathrm{is}(\omega, \omega')\hat{a}_\mathrm{s}^\dagger(\omega')\right] \\
&= \int \mathrm{d}\omega' \left\{ G_\mathrm{ii}(\omega, \omega') \int \mathrm{d}\omega'' \left[H_\mathrm{ii}(\omega', \omega'')\hat{b}_\mathrm{i}(\omega'') + H_\mathrm{is}(\omega', \omega'')\hat{b}_\mathrm{s}^\dagger(\omega'')\right] \right. \\
&\qquad \left. + G_\mathrm{is}(\omega, \omega') \int \mathrm{d}\omega'' \left[H_\mathrm{ss}^*(\omega', \omega'')\hat{b}_\mathrm{s}^\dagger(\omega'') + H_\mathrm{si}^*(\omega', \omega'')\hat{b}_\mathrm{i}(\omega'')\right] \right\}
\end{aligned} \tag{C.10}$$

and

$$\begin{aligned}
\hat{b}_\mathrm{s}(\omega) &= \int \mathrm{d}\omega' \left[G_\mathrm{ss}(\omega, \omega')\hat{a}_\mathrm{s}(\omega') + G_\mathrm{si}(\omega, \omega')\hat{a}_\mathrm{i}^\dagger(\omega')\right] \\
&= \int \mathrm{d}\omega' \left\{ G_\mathrm{ss}(\omega, \omega') \int \mathrm{d}\omega'' \left[H_\mathrm{ss}(\omega', \omega'')\hat{b}_\mathrm{s}(\omega'') + H_\mathrm{si}(\omega', \omega'')\hat{b}_\mathrm{i}^\dagger(\omega'')\right] \right. \\
&\qquad \left. + G_\mathrm{si}(\omega, \omega') \int \mathrm{d}\omega'' \left[H_\mathrm{ii}^*(\omega', \omega'')\hat{b}_\mathrm{i}^\dagger(\omega'') + H_\mathrm{is}^*(\omega', \omega'')\hat{b}_\mathrm{s}(\omega'')\right] \right\}
\end{aligned} \tag{C.11}$$

From this we find the four relations

$$\int \mathrm{d}\omega' \left[G_{\mathrm{ii}}(\omega,\omega')H_{\mathrm{ii}}(\omega',\omega'') + G_{\mathrm{is}}(\omega,\omega')H^*_{\mathrm{si}}(\omega'\omega'')\right] = \delta(\omega-\omega''), \tag{C.12}$$

$$\int \mathrm{d}\omega' \left[G_{\mathrm{ii}}(\omega,\omega')H_{\mathrm{is}}(\omega',\omega'') + G_{\mathrm{is}}(\omega,\omega')H^*_{\mathrm{ss}}(\omega'\omega'')\right] = 0, \tag{C.13}$$

$$\int \mathrm{d}\omega' \left[G_{\mathrm{ss}}(\omega,\omega')H_{\mathrm{ss}}(\omega',\omega'') + G_{\mathrm{si}}(\omega,\omega')H^*_{\mathrm{is}}(\omega'\omega'')\right] = \delta(\omega-\omega''), \tag{C.14}$$

$$\int \mathrm{d}\omega' \left[G_{\mathrm{ss}}(\omega,\omega')H_{\mathrm{si}}(\omega',\omega'') + G_{\mathrm{si}}(\omega,\omega')H^*_{\mathrm{ii}}(\omega'\omega'')\right] = 0, \tag{C.15}$$

which constrain the backward transfer functions to the forward ones. In comparison with the constraints in Eqs. (C.5), (C.6), and (C.7), we find that

$$\begin{bmatrix} H_{\mathrm{ii}}(\omega,\omega') & H_{\mathrm{is}}(\omega,\omega') \\ H_{\mathrm{si}}(\omega,\omega') & H_{\mathrm{ss}}(\omega,\omega') \end{bmatrix} = \begin{bmatrix} G^*_{\mathrm{ii}}(\omega',\omega) & -G_{\mathrm{si}}(\omega',\omega) \\ -G_{\mathrm{is}}(\omega',\omega) & G^*_{\mathrm{ss}}(\omega',\omega) \end{bmatrix}. \tag{C.16}$$

APPENDIX D

Unifying the Schrödinger- and Heisenberg pictures in the perturbative regime

Based on work in [49], we here demonstrate a relationship between the Heisenberg-picture Green functions G_{jk} and the Scrödinger-picture biphoton joint amplitude $\mathcal{A}$. While our derivation takes place in the time domain, an equivalent derivation can be performed in the frequency domain.

Consider an input state consisting of the two-mode vacuum state $|\Psi(z=0)\rangle = |0,0\rangle$, such that operation on the input state with either the signal- or the idler annihilation operator, yields

$$\hat{a}_{\mathrm{i}}(t')\,|0,0\rangle = \hat{a}_{\mathrm{s}}(t')\,|0,0\rangle = 0. \tag{D.1}$$

By insertion of the backward transformation kernels derived in Appendix C, one finds (for $\hat{a}_{\mathrm{i}}$)

$$\int \mathrm{d}t \left[G^{*}_{\mathrm{ii}}(t,t')\hat{b}_{\mathrm{i}}(t) - G_{\mathrm{si}}(t,t')\hat{b}^{\dagger}_{\mathrm{s}}(t)\right]|\Psi(0)\rangle = 0, \tag{D.2}$$

which involves the input state vector and the evolved signal- and idler operators, and is hence clearly written in the Heisenberg picture. We may, however, convert it to the Scrödinger picture by introducing the unitary operator $\hat{U}_l$ that evolves the state vector: $\hat{U}_l\,|\Psi(0)\rangle = |\Psi(l)\rangle$ and converts between input- and output operators according to $\hat{a}_j = \hat{U}_l \hat{b}_j \hat{U}_l^{\dagger}$. Thus, operating on Eq. (D.2) with $\hat{U}_l$ from the left, results in

$$\begin{aligned}\hat{U}_l \int \mathrm{d}t \left[G^{*}_{\mathrm{ii}}(t,t')\hat{b}_{\mathrm{i}}(t) - G_{\mathrm{si}}(t,t')\hat{b}^{\dagger}_{\mathrm{s}}(t)\right]|\Psi(0)\rangle \\ = \int \mathrm{d}t \left[G^{*}_{\mathrm{ii}}(t,t')\hat{a}_{\mathrm{i}}(t) - G_{\mathrm{si}}(t,t')\hat{a}^{\dagger}_{\mathrm{s}}(t)\right]|\Psi(l)\rangle = 0,\end{aligned} \tag{D.3}$$

in which we, to reach the second line, inserted the identity operator written as $\mathcal{I} = \hat{U}_l^\dagger \hat{U}_l$ before the state vector. Equation (D.3) contains the input mode operators and the evolved state vector, and is thus clearly written in the Scrödinger picture, despite the fact that it also contains the Heisenberg-picture transfer functions.

As in Eq. (2.32), the key to proceeding from Eq. (D.3) is to assume a perturbative expansion of the state vector according to

$$|\Psi(l)\rangle \approx |\Psi_0\rangle + \epsilon\,|\Psi_1\rangle\,, \tag{D.4}$$

where ϵ is a small perturbation parameter. Similarly, we consider the cross-transfer function G_{si}, which is related to the weak nonlinear interaction as a first-order perturbative term, i. e. $G_{\mathrm{si}} \to \epsilon G_{\mathrm{si}}$. Applying this perturbative framework to Eq. (D.3), we obtain the two equations to zeroth- and first order in ϵ, respectively:

$$\int \mathrm{d}t\; G_{\mathrm{ii}}^*(t,t')\hat{a}_{\mathrm{i}}(t)\,|\Psi_0\rangle = 0, \qquad [\epsilon^0], \tag{D.5}$$

$$\int \mathrm{d}t\; G_{\mathrm{ii}}^*(t,t')\hat{a}_{\mathrm{i}}(t)\,|\Psi_1\rangle = \int \mathrm{d}t\; G_{\mathrm{si}}(t,t')\hat{a}_{\mathrm{s}}^\dagger(t)\,|\Psi_0\rangle\,, \qquad [\epsilon^1]. \tag{D.6}$$

Whereas the zeroth-order equation is simply solved by the two-mode vacuum state (the input state), i.e. $|\Psi_0\rangle = |0,0\rangle$, finding the first-order perturbation $|\Psi_1\rangle$, which solves Eq. (D.6) is a little more involved. To achieve this, we need the constraint (3.15) on the form

$$\int \mathrm{d}t'\; G_{\mathrm{ii}}(t,t')G_{\mathrm{ii}}^*(t'',t') \approx \delta(t-t''), \tag{D.7}$$

where the approximation is correct to order ϵ^2. By now multiplying Eq. (D.6) from the left by $G_{\mathrm{ii}}(t'',t')\hat{a}_{\mathrm{i}}^\dagger(t'')$, and integrate with respect to both t' and t'', we obtain:

$$\begin{aligned}\iiint \mathrm{d}t''\mathrm{d}t'\mathrm{d}t\; G_{\mathrm{ii}}(t'',t')G_{\mathrm{ii}}^*(t,t')\hat{a}_{\mathrm{i}}^\dagger(t'')\hat{a}_{\mathrm{i}}(t)\,|\Psi_1\rangle \\ = \iiint \mathrm{d}t''\mathrm{d}t'\mathrm{d}t\; G_{\mathrm{ii}}(t'',t')G_{\mathrm{si}}(t,t')\hat{a}_{\mathrm{i}}^\dagger(t'')\hat{a}_{\mathrm{s}}^\dagger(t)\,|\Psi_0\rangle\,.\end{aligned} \tag{D.8}$$

By now invoking the expression in Eq. (D.7), the left-hand side of Eq. (D.8) simplifies significantly, leaving us with

$$\int \mathrm{d}t\; \hat{n}_{\mathrm{i}}(t)\,|\Psi_1\rangle = \iiint \mathrm{d}t''\mathrm{d}t'\mathrm{d}t\; G_{\mathrm{ii}}(t'',t')G_{\mathrm{si}}(t,t')\hat{a}_{\mathrm{i}}^\dagger(t'')\hat{a}_{\mathrm{s}}^\dagger(t)\,|\Psi_0\rangle\,, \tag{D.9}$$

where $\hat{n}_{\mathrm{i}}(t) = \hat{a}_{\mathrm{i}}^\dagger(t)\hat{a}_{\mathrm{i}}(t)$. Noting that the operator $\int \mathrm{d}t\hat{n}_{\mathrm{i}}(t)$ counts the number of idler photons, while the right-hand side is proportional to $\hat{a}_{\mathrm{i}}^\dagger(t)$, it is tempting to guess that $|\Psi_1\rangle$ itself equals the right-hand side. By inserting this, one finds that

$$|\Psi_1\rangle = \iiint \mathrm{d}t''\mathrm{d}t'\mathrm{d}t\; G_{\mathrm{ii}}(t'',t')G_{\mathrm{si}}(t,t')\hat{a}_{\mathrm{i}}^\dagger(t'')\hat{a}_{\mathrm{s}}^\dagger(t)\,|0,0\rangle\,, \tag{D.10}$$

indeed solves Eq. (D.9). Not surprisingly, $|\Psi_1\rangle$ exactly constitutes the biphoton state vector described in detail in Sec. 2.3, and thus in comparing Eq. (D.10) with Eq. (2.34), we find that the JTA is related to the transfer functions according to

$$\mathcal{A}(t_\mathrm{i}, t_\mathrm{s}) = \int \mathrm{d}t \; G_\mathrm{ii}(t_\mathrm{i}, t) G_\mathrm{si}(t_\mathrm{s}, t), \tag{D.11}$$

or, using the constraint in Eq. (3.16), equivalently

$$\mathcal{A}(t_\mathrm{i}, t_\mathrm{s}) = \int \mathrm{d}t \; G_\mathrm{ss}(t_\mathrm{s}, t) G_\mathrm{is}(t_\mathrm{i}, t). \tag{D.12}$$

In conclusion, we have identified a relationship between the Heisenberg-picture transfer (Green) functions used in Chapter 3 and the more commonly used Scrödinger-picture joint amplitude. The relationship is derived in the perturbative regime, and therefore only applies for low-generation rates.

APPENDIX E

Coupled-mode equations with undesired Bragg scattering

Based on work in [112], this appendix reports on how we numerical study the inclusion of multiple signal BS modes.

To model the standard co-polarized BS process including multiple BS signal modes we introduce multiple additional converted signal frequencies according to $\omega_{\mathrm{r}^{(n)}} = \omega_{\mathrm{s}} + \delta\omega(n+1)/2$ for n odd (up-converted fields), and $\omega_{\mathrm{r}^{(n)}} = \omega_{\mathrm{s}} - \delta\omega(n/2+1)$ for n even (down-converted fields), where $\delta\omega = \omega_{\mathrm{q}} - \omega_{\mathrm{p}} > 0$, [see also inset of Fig. 5.3(a)]. For each of these frequencies, the corresponding wavenumber is obtained from Eq. (5.8), resulting in the wavenumber mismatches

$$\Delta\beta_{j\to k} = \beta(\omega_j) - \beta(\omega_k) \pm (\beta(\omega_{\mathrm{p}}) - \beta(\omega_{\mathrm{q}}))\,, \tag{E.1}$$

where $+$ is chosen for $\omega_j > \omega_k$ and $-$ is chosen for $\omega_j < \omega_k$. Note, that this construction entails $\Delta\beta_{j\to k} = -\Delta\beta_{k\to j}$, as required. With the input fields placed such that $\omega_{\mathrm{s}} = -\omega_{\mathrm{p}}$, with frequencies measured relative to the waveguide ZDF, we have, for example, $\Delta\beta_{\mathrm{s}\to\mathrm{r}} = 0$, but $\Delta\beta_{\mathrm{s}\to\mathrm{r}^{(1)}} \neq 0$. The BS process only allows coupling between signal fields separated by $\delta\omega$, and thus the set of first-order

coupled ordinary differential equations takes the form

$$\partial_z A_{\mathrm{s}} = 2i\gamma \left(|A_{\mathrm{p}}|^2 + |A_{\mathrm{q}}|^2\right) A_{\mathrm{s}} + 2i\gamma \left(A_{\mathrm{p}}^* A_{\mathrm{q}} A_{\mathrm{r}} + A_{\mathrm{p}} A_{\mathrm{q}}^* A_{\mathrm{r}^{(1)}} \mathrm{e}^{i\Delta\beta_{\mathrm{r}^{(1)}\to\mathrm{s}}}\right), \tag{E.2}$$

$$\partial_z A_{\mathrm{r}} = 2i\gamma \left(|A_{\mathrm{p}}|^2 + |A_{\mathrm{q}}|^2\right) A_{\mathrm{r}} + 2i\gamma \left(A_{\mathrm{p}}^* A_{\mathrm{q}} A_{\mathrm{r}^{(2)}} \mathrm{e}^{i\Delta\beta_{\mathrm{r}^{(2)}\to\mathrm{r}}} + A_{\mathrm{p}} A_{\mathrm{q}}^* A_{\mathrm{s}}\right), \tag{E.3}$$

$$\partial_z A_{\mathrm{r}^{(1)}} = 2i\gamma \left(|A_p|^2 + |A_{\mathrm{q}}|^2\right) A_{\mathrm{r}^{(1)}} + 2i\gamma \left(A_{\mathrm{p}}^* A_{\mathrm{q}} A_{\mathrm{s}} \mathrm{e}^{i\Delta\beta_{\mathrm{s}\to\mathrm{r}^{(1)}}} + A_{\mathrm{p}} A_{\mathrm{q}}^* A_{\mathrm{r}^{(3)}} \mathrm{e}^{i\Delta\beta_{\mathrm{r}^{(3)}\to\mathrm{r}^{(1)}}}\right), \tag{E.4}$$

$$\partial_z A_{\mathrm{r}^{(2)}} = 2i\gamma \left(|A_{\mathrm{p}}|^2 + |A_{\mathrm{q}}|^2\right) A_{\mathrm{r}^{(2)}} + 2i\gamma \left(A_{\mathrm{p}}^* A_{\mathrm{q}} A_{\mathrm{r}^{(4)}} \mathrm{e}^{i\Delta\beta_{\mathrm{r}^{(4)}\to\mathrm{r}^{(2)}}} + A_{\mathrm{p}} A_{\mathrm{q}}^* A_{\mathrm{r}} \mathrm{e}^{i\Delta\beta_{\mathrm{r}\to\mathrm{r}^{(2)}}}\right), \tag{E.5}$$

$$\vdots$$

where the vertical dots present the equations for $a_{r^{(n>2)}}$. In the numerical simulations used to create Fig. 5.3, we included, for each value of Θ_{mis}, N additional fields so that negligible power transfer was observed to the most detuned fields, i.e. $n = N - 1$ and $n = N$.

Bibliography

[1] T. H. Maiman. Stimulated optical radiation in ruby. *Nature*, **187**:493–494, 1960.

[2] G. P. Agrawal. *Nonlinear fiber optics*. Elsevier, 5th edition, 2013.

[3] R. W. Boyd. *Nonlinear optics*. Elsevier, 2nd edition, 2003.

[4] K. Rottwitt and P. Tidemand-Lichtenberg. *Nonlinear optics: principles and applications*, volume **3**. CRC Press, 2014.

[5] P. A. Franken, A. E. Hill, C. W. Peters, and G. Weinreich. Generation of optical harmonics. *Phys. Rev. Lett.*, **7**(4):118, 1961.

[6] H. Kidorf, K. Rottwitt, M. Nissov, M. Ma, and E. Rabarijaona. Pump interactions in a 100-nm bandwidth Raman amplifier. *IEEE Photonics Technol. Lett.*, **11**(5):530–532, 1999.

[7] J. Hansryd, P. A. Andrekson, M. Westlund, J. Li, and P.-O. Hedekvist. Fiber-based optical parametric amplifiers and their applications. *IEEE J. Sel. Top. Quantum Electron.*, **8**(3):506–520, 2002.

[8] J. M. Dudley, G. Genty, and S. Coen. Supercontinuum generation in photonic crystal fiber. *Rev. Mod. Phys.*, **78**(4):1135, 2006.

[9] C. C. Gerry and P. L. Knight. *Introductory quantum optics*. Cambridge University Press, 3rd edition, 2008.

[10] Mark Hillery. Quantum cryptography with squeezed states. *Phys. Rev. A*, **61**(2):022309, 2000.

[11] L. A. Lugiato, A. Gatti, and E. Brambilla. Quantum imaging. *J. Opt. B: Quantum Semiclass. Opt.*, **4**(3):S176, 2002.

[12] V. Giovannetti, S. Lloyd, and L. Maccone. Quantum-enhanced measurements: beating the standard quantum limit. *Science*, **306**(5700):1330–1336, 2004.

[13] M. Giustina, M. A. M. Versteegh, S. Wengerowsky, J. Handsteiner, A. Hochrainer, K. Phelan, F. Steinlechner, J. Kofler, J.-Å. Larsson, C. Abellán, et al. Significant-loophole-free test of Bell's theorem with entangled photons. *Phys. Rev. Lett.*, **115**(25):250401, 2015.

[14] J. Yin, Y. Cao, Y.-H. Li, S.-K. Liao, L. Zhang, J.-G. Ren, W.-Q. Cai, W.-Y. Liu, B. Li, H. Dai, et al. Satellite-based entanglement distribution over 1200 kilometers. *Science*, **356**(6343):1140–1144, 2017.

[15] A. K Ekert, J. G. Rarity, P. R. Tapster, and G. M. Palma. Practical quantum cryptography based on two-photon interferometry. *Phys. Rev. Lett.*, **69**(9):1293, 1992.

[16] T. Jennewein, C. Simon, G. Weihs, H. Weinfurter, and A. Zeilinger. Quantum cryptography with entangled photons. *Phys. Rev. Lett.*, **84**(20):4729, 2000.

[17] S. Aaronson and A. Arkhipov. The computational complexity of linear optics. In *Proceedings of the forty-third annual ACM symposium on Theory of computing*, pages 333–342. ACM, 2011.

[18] A. Crespi, R. Osellame, R. Ramponi, D. J. Brod, E. F. Galvao, N. Spagnolo, C. Vitelli, E. Maiorino, P. Mataloni, and F. Sciarrino. Integrated multimode interferometers with arbitrary designs for photonic boson sampling. *Nat. Photonics*, **7**(7):545, 2013.

[19] E. Knill, R. Laflamme, and G. J. Milburn. A scheme for efficient quantum computation with linear optics. *Nature*, **409**(6816):46–52, 2001.

[20] P. Kok, W. J. Munro, K. Nemoto, T. C. Ralph, J. P. Dowling, and G. J. Milburn. Linear optical quantum computing with photonic qubits. *Rev. Mod. Phys.*, **79**(1):135, 2007.

[21] M. Gimeno-Segovia, P. Shadbolt, D. E. Browne, and T. Rudolph. From three-photon Greenberger-Horne-Zeilinger states to ballistic universal quantum computation. *Phys. Rev. Lett.*, **115**(2):020502, 2015.

[22] M. D. Eisaman, J. Fan, A. Migdall, and S. V. Polyakov. Invited review article: Single-photon sources and detectors. *Rev. Sci. Instrum.*, **82**(7):071101, 2011.

[23] C. Sun, M. T Wade, Y. Lee, J. S. Orcutt, L. Alloatti, M. S. Georgas, A. S. Waterman, J. M. Shainline, R. R. Avizienis, S. Lin, et al. Single-chip microprocessor that communicates directly using light. *Nature*, **528**(7583):534, 2015.

[24] J. Wang, S. Paesani, Y. Ding, R. Santagati, P. Skrzypczyk, A. Salavrakos, J. Tura, R. Augusiak, L. Mančinska, D. Bacco, et al. Multidimensional quantum entanglement with large-scale integrated optics. *Science*, page eaar7053, 2018.

[25] X.-C. Yao, T.-X. Wang, P. Xu, H. Lu, G.-S. Pan, X.-H. Bao, C.-Z. Peng, C.-Y. Lu, Y.-A. Chen, and J.-W. Pan. Observation of eight-photon entanglement. *Nat. Photonics*, **6**(4):225–228, 2012.

[26] X.-L. Wang, L.-K. Chen, W. Li, H.-L. Huang, C. Liu, C. Chen, Y.-H. Luo, Z.-E. Su, D. Wu, Z.-D. Li, H. Lu, Y. Hu, X. Jiang, C.-Z. Peng, L. Li, N.-L. Liu, Y.-A. Chen, C.-Y. Lu, and J.-W. Pan. Experimental ten-photon entanglement. *Phys. Rev. Lett.*, **117**:210502, Nov 2016.

[27] D. J. Griffiths. *Introduction to electrodynamics*. Pearson Education, Inc., 3rd edition, 2008.

[28] O. Reshef, E. Giese, M. Z. Alam, I. D. Leon, J. Upham, and R. W. Boyd. Beyond the perturbative description of the nonlinear optical response of low-index materials. *Opt. Lett.*, **42**(16):3225–3228, Aug 2017.

[29] J. Hansryd and P. A. Andrekson. Broad-band continuous-wave-pumped fiber optical parametric amplifier with 49-dB gain and wavelength-conversion efficiency. *IEEE Photonics Technol. Lett.*, **13**(3):194–196, 2001.

[30] S. Radic, C. J. McKinstrie, A. R. Chraplyvy, G. Raybon, J. C. Centanni, C. G. Jorgensen, K. Brar, and C. Headley. Continuous-wave parametric gain synthesis using nondegenerate pump four-wave mixing. *IEEE Photonics Technol. Lett.*, **14**(10):1406–1408, 2002.

[31] C. J. McKinstrie, J. D. Harvey, S. Radic, and M. G. Raymer. Translation of quantum states by four-wave mixing in fibers. *Opt. Express*, **13**(22):9131–9142, Oct 2005.

[32] A. Eckstein, A. Christ, P. J. Mosley, and C. Silberhorn. Highly efficient single-pass source of pulsed single-mode twin beams of light. *Phys. Rev. Lett.*, **106**(1):013603, 2011.

[33] J. E. Sharping, M. Fiorentino, and P. Kumar. Observation of twin-beam-type quantum correlation in optical fiber. *Opt. Lett.*, **26**(6):367–369, 2001.

[34] S. J. Carter, P. D. Drummond, M. D. Reid, and R. M. Shelby. Squeezing of quantum solitons. *Phys. Rev. Lett.*, **58**:1841–1844, May 1987.

[35] K. J. Blow, R. Loudon, S. J. D. Phoenix, and T. J. Shepherd. Continuum fields in quantum optics. *Phys. Rev. A*, **42**:4102–4114, Oct 1990.

[36] A. Christ, B. Brecht, W. Mauerer, and C. Silberhorn. Theory of quantum frequency conversion and type-II parametric down-conversion in the high-gain regime. *New J. Phys.*, **15**(5):053038, 2013.

[37] J. G. Koefoed, J. B. Christensen, and K. Rottwitt. Effects of noninstantaneous nonlinear processes on photon-pair generation by spontaneous four-wave mixing. *Phys. Rev. A*, **95**(4):043842, 2017.

[38] A. M. Brańczyk, T. M. Stace, and T. C. Ralph. Time ordering in spontaneous parametric down-conversion. In *AIP Conference Proceedings*, volume **1363**, pages 335–338. AIP, 2011.

[39] N. Quesada and J. E. Sipe. Effects of time ordering in quantum nonlinear optics. *Phys. Rev. A*, **90**:063840, Dec 2014.

[40] N. Quesada and J. E. Sipe. Time-ordering effects in the generation of entangled photons using nonlinear optical processes. *Phys. Rev. Lett.*, **114**:093903, Mar 2015.

[41] W. P. Grice and I. A. Walmsley. Spectral information and distinguishability in type-II down-conversion with a broadband pump. *Phys. Rev. A*, **56**(2):1627, 1997.

[42] W. P. Grice, A. B. U'Ren, and I. A. Walmsley. Eliminating frequency and space-time correlations in multiphoton states. *Phys. Rev. A*, **64**(6):063815, 2001.

[43] C. K. Law, I. A. Walmsley, and J. H. Eberly. Continuous frequency entanglement: effective finite Hilbert space and entropy control. *Phys. Rev. Lett.*, **84**(23):5304, 2000.

[44] B. J. Smith and M. G. Raymer. Photon wave functions, wave-packet quantization of light, and coherence theory. *New J. Phys.*, **9**(11):414, 2007.

[45] C.-K. Hong, Z.-Y. Ou, and L. Mandel. Measurement of subpicosecond time intervals between two photons by interference. *Phys. Rev. Lett.*, **59**(18):2044, 1987.

[46] A. M. Brańczyk. Hong-Ou-Mandel Interference. *ArXiv e-prints*, October 2017.

[47] K. Garay-Palmett, H. J. McGuinness, O. Cohen, J. S. Lundeen, R. Rangel-Rojo, A. B. U'Ren, M. G. Raymer, C. J. McKinstrie, S. Radic, and I. A. Walmsley. Photon pair-state preparation with tailored spectral properties by spontaneous four-wave mixing in photonic-crystal fiber. *Opt. Express*, **15**(22):14870–14886, Oct 2007.

[48] A. B. U'Ren, C. Silberhorn, R. Erdmann, K. Banaszek, W. P. Grice, I. A. Walmsley, and M. G. Raymer. Generation of pure-state single-photon wavepackets by conditional preparation based on spontaneous parametric downconversion. *Laser Phys.*, **15**:146–161, 2005.

[49] J. B. Christensen, C. J. McKinstrie, and K. Rottwitt. Temporally uncorrelated photon-pair generation by dual-pump four-wave mixing. *Phys. Rev. A*, **94**(1):013819, 2016.

[50] J. B. Christensen, C. J. McKinstrie, and K. Rottwitt. Generation of pure heralded single-photon states by cross-polarized spontaneous four-wave mixing. In *Conference on Lasers and Electro-Optics*, page FTu4C.8. Optical Society of America, 2016.

[51] B. J. Smith, P. Mahou, O. Cohen, J. S. Lundeen, and I. A. Walmsley. Photon pair generation in birefringent optical fibers. *Opt. Express*, **17**(26):23589–23602, 2009.

[52] B. Fang, O. Cohen, M. Liscidini, J. E. Sipe, and V. O. Lorenz. Fast and highly resolved capture of the joint spectral density of photon pairs. *Optica*, **1**(5):281–284, 2014.

[53] J. B. Spring, P. S. Salter, B. J. Metcalf, P. C. Humphreys, M. Moore, N. Thomas-Peter, M. Barbieri, X. Jin, N. K. Langford, W. S. Kolthammer, M. J. Booth, and I. A Walmsley. On-chip low loss heralded source of pure single photons. *Opt. Express*, **21**(11):13522–13532, 2013.

[54] J. B. Spring, P. L. Mennea, B. J. Metcalf, P. C. Humphreys, J. C. Gates, H. L. Rogers, C. Söller, B. J. Smith, W. S. Kolthammer, P. G. R. Smith, and I. A. Walmsley. Chip-based array of near-identical, pure, heralded single-photon sources. *Optica*, **4**(1):90–96, 2017.

[55] P. J. Mosley, J. S. Lundeen, B. J. Smith, P. Wasylczyk, A. B. U'Ren, C. Silberhorn, and I. A. Walmsley. Heralded generation of ultrafast single photons in pure quantum states. *Phys. Rev. Lett.*, **100**(13):133601, 2008.

[56] O. Cohen, J. S. Lundeen, B. J. Smith, G. Puentes, P. J. Mosley, and I. A. Walmsley. Tailored photon-pair generation in optical fibers. *Phys. Rev. Lett.*, **102**(12):123603, 2009.

[57] C. Söller, B. Brecht, P. J. Mosley, L. Y. Zang, A. Podlipensky, N. Y. Joly, P. St. J. Russell, and C. Silberhorn. Bridging visible and telecom wavelengths with a single-mode broadband photon pair source. *Phys. Rev. A*, **81**(3):031801, 2010.

[58] M. Halder, J. Fulconis, B. Cemlyn, A. Clark, C. Xiong, W. J. Wadsworth, and J. G. Rarity. Nonclassical 2-photon interference with separate intrinsically narrowband fibre sources. *Opt. Express*, **17**(6):4670–4676, 2009.

[59] R J.A. Francis-Jones, R. A. Hoggarth, and P. J. Mosley. All-fiber multiplexed source of high-purity single photons. *Optica*, **3**(11):1270–1273, 2016.

[60] E. Meyer-Scott, N. Montaut, J. Tiedau, L. Sansoni, H. Herrmann, T. J. Bartley, and C. Silberhorn. Limits on the heralding efficiencies and spectral purities of spectrally filtered single photons from photon-pair sources. *Phys. Rev. A*, **95**:061803, Jun 2017.

[61] D. R. Blay, M. J. Steel, and L. G. Helt. Effects of filtering on the purity of heralded single photons from parametric sources. *Phys. Rev. A*, **96**:053842, Nov 2017.

[62] M. J. Collins, C. Xiong, I. H. Rey, T. D. Vo, J. He, S. Shahnia, C. Reardon, T. F. Krauss, M. J. Steel, A. S. Clark, et al. Integrated spatial multiplexing of heralded single-photon sources. *Nat. Commun.*, **4**:2582, 2013.

[63] C. Xiong, X. Zhang, Z. Liu, M. J. Collins, A. Mahendra, L. G. Helt, M. J. Steel, D.-Y. Choi, C. J. Chae, P. H. W. Leong, et al. Active temporal multiplexing of indistinguishable heralded single photons. *Nat. Commun.*, **7**:10853, 2016.

[64] B. Bell, A. McMillan, W. McCutcheon, and J. Rarity. Effects of self- and cross-phase modulation on photon purity for four-wave-mixing photon pair sources. *Phys. Rev. A*, **92**:053849, Nov 2015.

[65] J. G. Koefoed, J. B. Christensen, C. J. McKinstrie, and K. Rottwitt. Effects of dispersion on spontaneous four-wave mixing in quantum applications. *submitted*.

[66] A. M. Brańczyk, A. Fedrizzi, T. M. Stace, T. C. Ralph, and A. G. White. Engineered optical nonlinearity for quantum light sources. *Opt. Express*, **19**(1):55–65, 2011.

[67] F. Graffitti, P. Barrow, M. Proietti, D. Kundys, and A. Fedrizzi. Independent high-purity photons created in domain-engineered crystals. *Optica*, **5**(5):514–517, 2018.

[68] B. Fang, O. Cohen, J. B. Moreno, and V. O. Lorenz. State engineering of photon pairs produced through dual-pump spontaneous four-wave mixing. *Opt. Express*, **21**(3):2707–2717, Feb 2013.

[69] J. G. Koefoed, S. M. M. Friis, J. B. Christensen, and K. Rottwitt. Spectrally pure heralded single photons by spontaneous four-wave mixing in a fiber: reducing impact of dispersion fluctuations. *Opt. Express*, **25**(17):20835–20849, Aug 2017.

[70] E. N. Christensen, S. M. M. Friis, J. G. Koefoed, M. A. Usuga Castaneda, and K. Rottwitt. Near-infrared photon-pair generation by intermodal four-wave mixing in a few-mode fiber. In *Frontiers in Optics 2017*, page JW4A.6. Optical Society of America, 2017.

[71] E. N. Christensen, J. B. Christensen, S. M. M. Friis, J. G. Koefoed, M. A. U. Castaneda, and K. Rottwitt. Heralded single-photon source based on intermodal four-wave mixing in a few-mode fiber. In *Conference on Lasers and Electro-Optics*, page FM3G.3. Optical Society of America, 2018.

[72] S. Signorini, M. Mancinelli, M. Borghi, M. Bernard, M. Ghulinyan, G. Pucker, and L. Pavesi. Intermodal four-wave mixing in silicon waveguides. *Photon. Res.*, **6**(8):805–814, Aug 2018.

[73] J. E. Rothenberg. Modulational instability for normal dispersion. *Phys. Rev, A*, **42**(1):682, 1990.

[74] S. M. M. Friis, I. Begleris, Y. Jung, K. Rottwitt, P. Petropoulos, D. J. Richardson, P. Horak, and F. Parmigiani. Inter-modal four-wave mixing study in a two-mode fiber. *Opt. Express*, **24**(26):30338–30349, 2016.

[75] P. D. Drummond, T. A. B. Kennedy, J. M. Dudley, R. Leonhardt, and J. D. Harvey. Cross-phase modulational instability in high-birefringence fibers. *Opt. Commun.*, **78**(2):137–142, 1990.

[76] D. Amans, E. Brainis, M. Haelterman, P. Emplit, and S. Massar. Vector modulation instability induced by vacuum fluctuations in highly birefringent fibers in the anomalous-dispersion regime. *Opt. Lett*, **30**(9):1051–1053, 2005.

[77] M. A. Foster, A. C. Turner, J. E. Sharping, B. S. Schmidt, M. Lipson, and A. L. Gaeta. Broad-band optical parametric gain on a silicon photonic chip. *Nature*, **441**(7096):960, 2006.

[78] K. Guo, L. Lin, J. B. Christensen, E. N. Christensen, X. Shi, Y. Ding, K. Rottwitt, and H. Ou. Broadband wavelength conversion in a silicon vertical-dual-slot waveguide. *Opt. Express*, **25**(26):32964–32971, Dec 2017.

[79] J. Chen, X. Li, and P. Kumar. Two-photon-state generation via four-wave mixing in optical fibers. *Phys. Rev. A*, **72**(3):033801, 2005.

[80] L. Mejling, D. S. Cargill, C. J. McKinstrie, K. Rottwitt, and R. O. Moore. Effects of nonlinear phase modulation on bragg scattering in the low-conversion regime. *Opt. Express*, **20**(24):27454–27475, Nov 2012.

[81] L. Mejling, C. J. McKinstrie, M. G. Raymer, and K. Rottwitt. Quantum frequency translation by four-wave mixing in a fiber: low-conversion regime. *Opt. Express*, **20**(8):8367–8396, 2012.

[82] S. L. Braunstein. Squeezing as an irreducible resource. *Phys. Rev. A*, **71**:055801, May 2005.

[83] C. J. McKinstrie and M. Karlsson. Schmidt decompositions of parametric processes i: Basic theory and simple examples. *Opt. Express*, **21**(2):1374–1394, Jan 2013.

[84] H. J. McGuinness, M. G. Raymer, and C. J. McKinstrie. Theory of quantum frequency translation of light in optical fiber: application to interference of two photons of different color. *Opt. Express*, **19**(19):17876–17907, 2011.

[85] D. V. Reddy, M. G. Raymer, C. J. McKinstrie, L. Mejling, and K. Rottwitt. Temporal mode selectivity by frequency conversion in second-order nonlinear optical waveguides. *Opt. Express*, **21**(11):13840–13863, Jun 2013.

[86] C. J. McKinstrie, J. B. Christensen, K. Rottwitt, and M. G. Raymer. Generation of two-temporal-mode photon states by vector four-wave mixing. *Op. Express*, **25**(17):20877–20893, 2017.

[87] V. Ansari, E. Roccia, M. Santandrea, M. Doostdar, C. Eigner, L. Padberg, I. Gianani, M. Sbroscia, J. M. Donohue, L. Mancino, M. Barbieri, and C. Silberhorn. Heralded generation of high-purity ultrashort single photons in programmable temporal shapes. *Opt. Express*, **26**(3):2764–2774, Feb 2018.

[88] V. Ansari, J. M. Donohue, B. Brecht, and C. Silberhorn. Tailoring nonlinear processes for quantum optics with pulsed temporal-mode encodings. *Optica*, **5**(5):534–550, May 2018.

[89] J. Zhang, Q. Lin, G. Piredda, R. W. Boyd, G. P. Agrawal, and PM Fauchet. Anisotropic nonlinear response of silicon in the near-infrared region. *Appl. Phys. Lett.*, **91**(7):071113, 2007.

[90] S. D. Dyer, M. J. Stevens, B. Baek, and S. W. Nam. High-efficiency, ultra low-noise all-fiber photon-pair source. *Opt. Express*, **16**(13):9966–9977, Jun 2008.

[91] J. B. Christensen, J. G. Koefoed, K. Rottwitt, and C. J. McKinstrie. Engineering spectrally unentangled photon pairs from nonlinear microring resonators by pump manipulation. *Opt. Lett.*, **43**(4):859–862, 2018.

[92] J. B. Christensen, J. G. Koefoed, C. J. McKinstrie, and K. Rottwitt. Spectrally unentangled photon pairs from microring resonators using pump-pulse tailoring. In *Conference on Lasers and Electro-Optics*, page FTh1G.1. Optical Society of America, 2018.

[93] A. Politi, J. C. F. Matthews, M. G. Thompson, and J. L. O'Brien. Integrated quantum photonics. *IEEE J. Sel. Top. Quantum Electron.*, **15**(6):1673–1684, Nov 2009.

[94] A. Dutt, K. Luke, S. Manipatruni, A. L. Gaeta, P. Nussenzveig, and M. Lipson. On-chip optical squeezing. *Phys. Rev. Applied*, **3**:044005, Apr 2015.

[95] J. W. Silverstone, D. Bonneau, J. L. O'Brien, and M. G. Thompson. Silicon quantum photonics. *IEEE J. Sel. Top. Quantum Electron.*, **22**(6):390–402, 2016.

[96] M. Heuck, Y. Ding, L. H. Frandsen, J. G. Koefoed, J. B. Christensen, and K. Rottwitt. Unidirectional frequency conversion in silicon-based double-ring microresonator. In *Conference on Lasers and Electro-Optics*, page JTh4C.4. Optical Society of America, 2018.

[97] C. Reimer, L. Caspani, M. Clerici, M. Ferrera, M. Kues, M. Peccianti, A. Pasquazi, L. Razzari, B. E. Little, S. T. Chu, D. J. Moss, and R. Morandotti. Integrated frequency comb source of heralded single photons. *Opt. Express*, **22**(6):6535–6546, Mar 2014.

[98] D. Grassani, A. Simbula, S. Pirotta, M. Galli, M. Menotti, N. C. Harris, T. Baehr-Jones, M. Hochberg, C. Galland, M. Liscidini, and D. Bajoni. Energy correlations of photon pairs generated by a silicon microring resonator probed by stimulated four wave mixing. *Sci. Rep.*, **6**:23564, 2016.

[99] Z. Vernon, M. Liscidini, and J. E. Sipe. No free lunch: the trade-off between heralding rate and efficiency in microresonator-based heralded single photon sources. *Opt. Lett.*, **41**(4):788–791, Feb 2016.

[100] M. Heuck, M. Pant, and D. R. Englund. Temporally and spectrally multiplexed single photon source using quantum feedback control for scalable photonic quantum technologies. *New J. Phys.*, **20**(6):063046, 2018.

[101] C. Reimer, M. Kues, P. Roztocki, B. Wetzel, F. Grazioso, B. E. Little, S. T. Chu, T. Johnston, Y. Bromberg, L. Caspani, D. J. Moss, and R. Morandotti. Generation of multiphoton entangled quantum states by means of integrated frequency combs. *Science*, **351**(6278):1176–1180, 2016.

[102] M. Kues, C. Reimer, P. Roztocki, L. R. Cortés, S. Sciara, B. Wetzel, Y. Zhang, A. Cino, S. T. Chu, B. E. Little, D. J. Moss, L. Caspani, J. Azaña, and R. Morandotti. On-chip generation of high-dimensional entangled quantum states and their coherent control. *Nature*, **546**(7660):622–626, 2017.

[103] P. Imany, J. A. Jaramillo-Villegas, O. D. Odele, K. Han, D. E. Leaird, J. M. Lukens, P. Lougovski, M. Qi, and A. M. Weiner. 50-GHz-spaced comb of high-dimensional frequency-bin entangled photons from an on-chip silicon nitride microresonator. *Opt. Express*, **26**(2):1825–1840, Jan 2018.

[104] L. G. Helt, Z. Yang, M. Liscidini, and J. E. Sipe. Spontaneous four-wave mixing in microring resonators. *Opt. Lett.*, **35**(18):3006–3008, Sep 2010.

[105] I. I. Faruque, G. F. Sinclair, D. Bonneau, J. G. Rarity, and M. G. Thompson. On-chip quantum interference with heralded photons from two independent micro-ring resonator sources in silicon photonics. *Opt. Express*, **26**(16):20379–20395, Aug 2018.

[106] A. Christ, K. Laiho, A. Eckstein, K. N. Cassemiro, and C. Silberhorn. Probing multimode squeezing with correlation functions. *New J. Phys.*, **13**(3):033027, 2011.

[107] Z. Vernon, M. Menotti, C. C. Tison, J. A. Steidle, M. L. Fanto, P. M. Thomas, S. F. Preble, A. M. Smith, P. M. Alsing, M. Liscidini, and J. E. Sipe. Truly unentangled photon pairs without spectral filtering. *Opt. Lett.*, **42**(18):3638–3641, Sep 2017.

[108] C. C. Tison, J. A. Steidle, M. L. Fanto, Z. Wang, N. A. Mogent, A. Rizzo, S. F. Preble, and P. M. Alsing. Path to increasing the coincidence efficiency of integrated resonant photon sources. *Opt. Express*, **25**(26):33088–33096, Dec 2017.

[109] L. Zhang, C. Bao, V. Singh, J. Mu, C. Yang, A. M. Agarwal, L. C. Kimerling, and J. Michel. Generation of two-cycle pulses and octave-spanning frequency combs in a dispersion-flattened micro-resonator. *Opt. Lett.*, **38**(23):5122–5125, 2013.

[110] C. Joshi, A. Farsi, S. Clemmen, S. Ramelow, and A. L. Gaeta. Frequency multiplexing for quasi-deterministic heralded single-photon sources. *Nat. Commun.*, **9**(1):847, 2018.

[111] M. Heuck, J. G. Koefoed, J. B. Christensen, Y. Ding, L. H. L. H. Frandsen, K. Rottwitt, and L. K. Oxenløwe. Unidirectional frequency conversion in microring resonators for on-chip frequency-multiplexed single-photon sources. *submitted*.

[112] J. B. Christensen, J. G. Koefoed, B. A. Bell, C. J. McKinstrie, and K. Rottwitt. Shape-preserving and unidirectional frequency conversion by four-wave mixing. *Opt. Express*, **26**(13):17145–17157, Jun 2018.

[113] H. J. McGuinness, M. G. Raymer, C. J. McKinstrie, and S. Radic. Quantum frequency translation of single-photon states in a photonic crystal fiber. *Phys. Rev. Lett.*, **105**(9):093604, 2010.

[114] A. S. Clark, S. Shahnia, M. J. Collins, C. Xiong, and B. J. Eggleton. High-efficiency frequency conversion in the single-photon regime. *Opt. Lett.*, **38**(6):947–949, Mar 2013.

[115] Q. Li, M. Davanço, and K. Srinivasan. Efficient and low-noise single-photon-level frequency conversion interfaces using silicon nanophotonics. *Nat. Photonics*, **10**(6):406, 2016.

[116] S. Tanzilli, W. Tittel, M. Halder, O. Alibart, P. Baldi, N. Gisin, and H. Zbinden. A photonic quantum information interface. *Nature*, **437**(7055):116–120, 2005.

[117] M. Allgaier, V. Ansari, L. Sansoni, C. Eigner, V. Quiring, R. Ricken, G. Harder, B. Brecht, and C. Silberhorn. Highly efficient frequency conversion with bandwidth compression of quantum light. *Nat. Commun.*, **8**:14288, 2017.

[118] B. Brecht, D. V. Reddy, C. Silberhorn, and M. G. Raymer. Photon temporal modes: a complete framework for quantum information science. *Phys. Rev. X*, **5**(4):041017, 2015.

[119] Y.-S. Ra, C. Jacquard, A. Dufour, C. Fabre, and N. Treps. Tomography of a mode-tunable coherent single-photon subtractor. *Phys. Rev. X*, **7**(3):031012, 2017.

[120] D. V. Reddy and M. G. Raymer. High-selectivity quantum pulse gating of photonic temporal modes using all-optical ramsey interferometry. *Optica*, **5**(4):423–428, Apr 2018.

[121] Y. Zhao, D. Lombardo, J. Mathews, and I. Agha. Low control-power wavelength conversion on a silicon chip. *Opt. Lett.*, **41**(15):3651–3654, Aug 2016.

[122] K. Li, H.-F. Ting, M. A. Foster, and A. C. Foster. High-speed all-optical nand/and logic gates using four-wave mixing Bragg scattering. *Opt. Lett.*, **41**(14):3320–3323, Jul 2016.

[123] Y. Zhao, D. Lombardo, J. Mathews, and I. Agha. All-optical switching via four-wave mixing Bragg scattering in a silicon platform. *APL Photonics*, **2**(2):026102, 2017.

[124] I. Agha, S. Ates, M. Davanço, and K. Srinivasan. A chip-scale, telecommunications-band frequency conversion interface for quantum emitters. *Opt. Express*, **21**(18):21628–21638, 2013.

[125] I. Agha, M. Davanço, B. Thurston, and K. Srinivasan. Low-noise chip-based frequency conversion by four-wave-mixing Bragg scattering in SiN_x waveguides. *Opt. Lett.*, **37**(14):2997–2999, 2012.

[126] B. A. Bell, J. He, C. Xiong, and B. J. Eggleton. Frequency conversion in silicon in the single photon regime. *Opt. Express*, **24**(5):5235–5242, 2016.

[127] K. Li, H. Sun, and A. C. Foster. Four-wave mixing Bragg scattering in hydrogenated amorphous silicon waveguides. *Opt. Lett.*, **42**(8):1488–1491, Apr 2017.

[128] C. J. McKinstrie, L. Mejling, M. G. Raymer, and K. Rottwitt. Quantum-state-preserving optical frequency conversion and pulse reshaping by four-wave mixing. *Phys. Rev. A*, **85**:053829, May 2012.

[129] F. Parmigiani, P. Horak, Y. Jung, L. Grüner-Nielsen, T. Geisler, P. Petropoulos, and D. J. Richardson. All-optical mode and wavelength converter based on parametric processes in a three-mode fiber. *Opt. Express*, **25**(26):33602–33609, 2017.

[130] E. Bahar, X. Ding, A. Dahan, H. Suchowski, and J. Moses. Adiabatic four-wave mixing frequency conversion. *Opt. Express*, **26**(20):25582–25601, Oct 2018.

[131] K. Inoue. Tunable and selective wavelength conversion using fiber four-wave mixing with two pump lights. *IEEE Photonics Technol. Lett.*, **6**(12):1451–1453, 1994.

[132] S. Clemmen, A. Farsi, S. Ramelow, and A. L. Gaeta. Ramsey interference with single photons. *Phys. Rev. Lett.*, **117**(22):223601, 2016.

[133] B. A. Bell, C. Xiong, D. Marpaung, C. J. McKinstrie, and B. J. Eggleton. Uni-directional wavelength conversion in silicon using four-wave mixing driven by cross-polarized pumps. *Opt. Lett.*, **42**(9):1668–1671, May 2017.

[134] Q. Lin, O. J. Painter, and G. P. Agrawal. Nonlinear optical phenomena in silicon waveguides: modeling and applications. *Opt. Express*, **15**(25):16604–16644, 2007.

[135] J. Noda, K. Okamoto, and Y. Sasaki. Polarization-maintaining fibers and their applications. *J. Light. Technol.*, **4**(8):1071–1089, 1986.

[136] I. Kiyat, A. Aydinli, and N. Dagli. A compact silicon-on-insulator polarization splitter. *IEEE Photonics Technol. Lett.*, **17**(1):100–102, 2005.

[137] F. Morichetti, A. Melloni, M. Martinelli, R. G. Heideman, A. Leinse, D. H. Geuzebroek, and A. Borreman. Box-shaped dielectric waveguides: A new concept in integrated optics? *J. Light. Technol.*, **25**(9):2579–2589, 2007.

[138] J. B. Christensen, D. V. Reddy, C. J. McKinstrie, K. Rottwitt, and M. G. Raymer. Temporal mode sorting using dual-stage quantum frequency conversion by asymmetric Bragg scattering. *Opt. Express*, **23**(18):23287–23301, 2015.

[139] S. Blanes, F. Casas, J. A. Oteo, and J. Ros. The Magnus expansion and some of its applications. *Phys. Rep.*, **470**(5-6):151–238, 2009.

[140] D. V. Reddy, M. G. Raymer, and C. J. McKinstrie. Efficient sorting of quantum-optical wave packets by temporal-mode interferometry. *Opt. Lett.*, **39**(10):2924–2927, May 2014.

[141] J. Leuthold, C. Koos, and W. Freude. Nonlinear silicon photonics. *Nat. Photonics*, **4**(8):535, 2010.

[142] R. Claps, D. Dimitropoulos, V. Raghunathan, Y. Han, and B. Jalali. Observation of stimulated Raman amplification in silicon waveguides. *Opt. Express*, **11**(15):1731–1739, Jul 2003.

[143] K. Yamada, H. Fukuda, T. Tsuchizawa, T. Watanabe, T. Shoji, and S. Itabashi. All-optical efficient wavelength conversion using silicon photonic wire waveguide. *IEEE Photon. Tech. Lett.*, **18**(9):1046–1048, 2006.

[144] D. L. Staebler and C. R. Wronski. Reversible conductivity changes in discharge-produced amorphous Si. *Appl. Phys. Lett.*, **31**(4):292–294, 1977.

[145] A. Kołodziej. Staebler-Wronski effect in amorphous silicon and its alloys. *Opto-electron. Rev.*, **12**(1):21–32, 2004.

[146] B. Kuyken, H. Ji, S. Clemmen, S. K. Selvaraja, H. Hu, M. Pu, M. Galili, P. Jeppesen, G. Morthier, S. Massar, L.K. Oxenløwe, G. Roelkens, and R. Baets. Nonlinear properties of and nonlinear processing in hydrogenated amorphous silicon waveguides. *Opt. Express*, **19**(26):146–153, Dec 2011.

[147] C. Grillet, L. Carletti, C. Monat, P. Grosse, B. B. Bakir, S. Menezo, J. M. Fedeli, and D. J. Moss. Amorphous silicon nanowires combining high nonlinearity, FOM and optical stability. *Opt. Express*, **20**(20):22609–22615, Sep 2012.

[148] J. Matres, G. C. Ballesteros, P. Gautier, J.-M. Fédéli, J. Martí, and C. J. Oton. High nonlinear figure-of-merit amorphous silicon waveguides. *Opt. Express*, **21**(4):3932–3940, Feb 2013.

[149] A. B. Fallahkhair, K. S. Li, and T. E. Murphy. Vector finite difference modesolver for anisotropic dielectric waveguides. *J. Lightwave Technol.*, **26**(11):1423–1431, Jun 2008.

[150] S. J. McNab, N. Moll, and Y. A. Vlasov. Ultra-low loss photonic integrated circuit with membrane-type photonic crystal waveguides. *Opt. Express*, **11**(22):2927–2939, Nov 2003.

[151] M. Pu, L. Liu, H. Ou, K. Yvind, and J. M. Hvam. Ultra-low-loss inverted taper coupler for silicon-on-insulator ridge waveguide. *Opt. Commun.*, **283**(19):3678–3682, 2010.

[152] D. Dai and J. E. Bowers. Novel concept for ultracompact polarization splitter-rotator based on silicon nanowires. *Opt. Express*, **19**(11):10940–10949, 2011.

[153] W. W. Lui and W.-P.Huang. Polarization rotation in semiconductor bending waveguides: A coupled-mode theory formulation. *J. Lightwave Technol.*, **16**(5):929, May 1998.

[154] N. Somasiri and B. M. Azizur Rahman. Polarization crosstalk in high index contrast planar silica waveguides with slanted sidewalls. *J. Lightwave Technol.*, **21**(1):54, Jan 2003.

[155] K. R. H. Bottrill, M. A. Ettabib, J. C. Gates, C. Lacava, F. Parmigiani, D. J. Richardson, and P. Petropoulos. Flexible scheme for measuring chromatic dispersion based on interference of frequency tones. In *Optical Fiber Communication Conference*, pages Th4H–5. Optical Society of America, 2017.

[156] K. R. H. Bottrill, G. D. Hesketh, F. Parmigiani, P. Horak, D. J. Richardson, and P. Petropoulos. Suppression of gain variation in a psa-based phase regenerator using an additional harmonic. *IEEE Photonics Technol. Lett.*, **26**(20):2074–2077, 2014.

[157] J. Demas, G. Prabhakar, T. He, and S. Ramachandran. Broadband and wideband parametric gain via intermodal four-wave mixing in optical fiber. In *CLEO: Science and Innovations*, page SM3M.1. Optical Society of America, 2017.

[158] P. Girouard, L. H. Frandsen, M. Galili, and L. K. Oxenløwe. A deuterium-passivated amorphous silicon platform for stable integrated nonlinear optics. In *Conference on Lasers and Electro-Optics*, page SW4I.2. Optical Society of America, 2018.

[159] J. G. Koefoed, J. B. Christensen, and K. Rottwitt. Split-step scheme for photon-pair generation through spontaneous four-wave mixing. In *2017 European Conference on Lasers and Electro-Optics and European Quantum Electronics Conference*, page EA.P.23. Optical Society of America, 2017.

[160] M. A. Nielsen and I. L Chuang. *Quantum computation and quantum information*. Cambridge university press, 2010.